

Transport and Optical Effects in
Self-Assembled Quantum Dot Devices

Adam Brown, MPhys.

Thesis submitted to the University of Nottingham
for the degree of Doctor of Philosophy

April 2009

Abstract

This thesis describes a theoretical and numerical study of quantum transport and optical effects through an array of self-assembled InAs quantum dots grown in the intrinsic region of a GaAs p-i-n junction. We present a numerical simulation of this system and compare the generated transport and electroluminescence results to recent experimental data. The simulation first calculates the quantum tunnelling, excitonic recombination, and relaxation rates within the dots, and then uses a stochastic model to simulate carriers entering and leaving the array. We highlight a number of features within the simulation, which shed light on similar features seen in experimental data. In particular, we demonstrate the importance of including the effects of the Coulomb interactions between the carriers, as this is shown to be necessary for the simulated and experimental results to match closely. We also investigate a model of Auger processes which is shown to produce up-conversion luminescence, and study the effect of varying the location of the array within the intrinsic region.

Additionally we present a master equation approach, which we use to describe a correlated tunnelling regime, in which the Coulomb interaction between an electron and a hole forces them to tunnel alternately onto a single dot before recombination. We produce current and photon noise predictions for both tunnelling and recombination limited regimes. We also investigate this phenomena for a pair of interacting dots, and find a number of two dot configurations which are able to produce current and electroluminescence. We present current and photo-current rate predictions for each case, and associated current and photon noise results.

Acknowledgments

The completion of this thesis could not have taken place without the assistance and support of several people.

Firstly I would like to thank my supervisor Keith Benedict, whose knowledgeable advice and support proved invaluable on many occasions. The experimental group, headed by Prof Laurence Eaves and Prof Amalia Patane, particularly Andreas and Ricky, for their enthusiastic collaboration. My office-mates, particularly Tom Harvey, who was always on hand with the answer to any question I could possibly think of. The Nottingham Thieves baseball team over the years for being a necessary and entertaining diversion from physics. My housemate Dave, and pseudo-housemate Tom for generously letting me win at darts on the many trips to the crown and the cricketers. Kate, of course, and my parents, for their eternal patience and immeasurable help and assistance. Finally, it only remains for me to thank the EPSRC for providing the funding for this project.

Contents

Contents	iii
List of Figures	vi
1 Introduction	1
1.1 Semiconductor p-i-n junctions	2
1.2 Quantum Dots	10
1.3 Experimental Information	14
1.4 Outline of Thesis	17
2 Mathematical Model	19
2.1 Quantum Dots	19
2.2 Quantum Tunnelling	24
2.3 Recombination Processes	32
2.4 Full Rate Equations	36
3 Implementation	44
3.1 Calculating The Energy Levels	44
3.2 Calculating the Rates	48
3.3 Calculating the Populations	54
4 Including the Coulomb interaction	61
4.1 Mathematical Model	61
4.2 Implementation and Results	67
5 Analysis of Simulation	74
5.1 Delayed Recombination Effects	74
5.2 Many Dot Interactions	81
5.3 Up Conversion Luminescence	85

6	Correlated Tunnelling Regime Analysis	93
6.1	Correlated Tunnelling Regime	93
6.2	CTR in a single quantum dot	96
6.3	CTR in two interacting quantum dots	105
7	Conclusions and Future Prospects	119
	Bibliography	122

Publications and Presentations

EP2DS-MSS 2007, Genoa, Italy. Poster presentation: “*Theoretical Studies of Electroluminescence in Self-Assembled InAs Quantum Dots*”

CMMP 2007, Leicester, UK. Poster Presentation: “*Simulation of Electroluminescence in self-assembled InAs quantum dots*”

CMMP 2006, Exeter, UK. Poster presentation: “*Simulation of Resonant tunnelling and Coulomb charging effects within self assembled InAs quantum dots in a GaAs quantum well*”

A. L. Brown, K. A. Benedict. “*Correlated Tunnelling Noise in Quantum Dot Systems*”, paper in preparation.

A. L. Brown, K. A. Benedict. “*Simulation of Coulomb Effects in self-assembled Quantum Dot Devices*”, paper in preparation.

List of Figures

1.1.1 Bandstructure formation in crystalline solids	3
1.1.2 Valence and conduction bands and bandgap	4
1.1.3 The conduction and valence bands for an insulator and a metal	5
1.1.4 Electrons and holes	6
1.1.5 The energy-wavevector relationship in GaAs.	7
1.1.6 p doped and n doped semiconductors	8
1.1.7 A p-i-n junction under zero volts.	9
1.2.1 A diagram of the energy levels of a quantum well	11
1.2.2 Tunnelling through a barrier into and out of a quantum well	12
1.2.3 A quantum well formed by surrounding a layer of InAs with GaAs.	13
1.2.4 The bottom 2 energy levels in a dot for each dimension	13
1.3.1 Stranski-Krastanov growth of InAs/GaAs quantum dots	15
1.3.2 InAs dots within a p-i-n junction	16
2.1.1 Quantum Harmonic Oscillator Model	21
2.1.2 The energy levels included in the simulation	22
2.2.1 p-i-n junction with a layer of dots embedded	24
2.2.2 Model of a triangular barrier	27
2.2.3 p-i-n junction at zero Volts	28
2.2.4 p-i-n junction at typical resonant bias voltage of 1.25 V	29
2.2.5 p-i-n junction at 1.52V (flat band conditions)	30
2.2.6 resonant tunnelling	31
2.3.1 Excitonic Recombination within a dot	33
2.3.2 Overlap integrals between energy levels	34
2.3.3 Phonon Assisted relaxation mechanism	35
2.4.1 Totality of Processes used in Model	37
2.4.2 Variation of level occupation probability with bias voltage	43
3.1.1 Distribution of electron dot energy levels generated	46
3.1.2 Distribution of hole dot energy levels generated	47
3.2.1 Background tunnelling rate $T_{in(p)}$	49
3.2.2 Resonance Function for a randomly chosen dot	51

3.2.3 total resonance for all 2500 dots	52
3.2.4 Comparison of rates of all major processes	53
3.3.1 Electrons and Holes occupying the dot array	55
3.3.2 Current vs voltage plot for transport through the dot array	56
3.3.3 The number of photons emitted per 1000 timesteps for each voltage	57
3.3.4 EL colour-scale plot of photon energy against bias voltage	58
3.3.5 Comparison of experimental and theoretical EL colour-scale plots	60
4.1.1 Average separation between two electrons in a QHO	63
4.1.2 Energy level shifting	64
4.1.3 Bandstructure distortion	65
4.1.4 Typical separation between neighbouring dots	66
4.1.5 “Fingers” extending from contacts towards dots	66
4.2.1 Resonance Function with Coulomb interaction included	67
4.2.2 Fluctuations in tunnelling distance	68
4.2.3 Fluctuations in the background tunnelling rate	69
4.2.4 IV plot with Coulomb Interaction	70
4.2.5 Photon Emission plot with Coulomb Interaction	71
4.2.6 EL colourscale plot with Coulomb Interaction	72
4.2.7 Experimental EL colourscale plot	73
5.1.1 Photons emitted via delayed recombination	75
5.1.2 EL plot with leakage current without Coulomb interactions	76
5.1.3 EL plot with leakage current with Coulomb interactions	76
5.1.4 Two different dot array locations within intrinsic region	78
5.1.5 Comparison of IV plots with no Coulomb interactions included	79
5.1.6 Comparison of IV plots with full Coulomb interactions included	80
5.1.7 Comparison of symmetric case	80
5.2.1 Neighbouring Dot Interactions	81
5.2.2 xy plot of the dot array	82
5.2.3 Variation of Coulomb field correlation length with bias voltage	84
5.3.1 Evidence of UCL in experimental plots	85
5.3.2 Proposed Mechanism of Auger Process	87
5.3.3 Simulated UCL colourscale plot and spectra	89
5.3.4 Simulated relationship of UCL emission with Magnetic Field	90
6.1.1 Correlated Tunnelling Regime Mechanism	94
6.1.2 Time Series showing electrons and holes tunnelling sequentially	96
6.2.1 Three Possible States of CTR system	98
6.2.2 Associations between bath and system processes	99
6.2.3 Simulated Noise Characteristics for different tunnelling rates	104

6.3.1	The four possible combinations of E_A and E_B in the dot offset . . .	105
6.3.2	The 10 possible combinations of 2 dots	106
6.3.3	9 Possible states of the system	107
6.3.4	trajectories of the system for the 10 different configurations	108
6.3.5	State Trajectories of FF system	109
6.3.6	State Trajectories of OF system.	110
6.3.7	State Trajectories of EH system	111
6.3.8	State occupation probabilities	115
6.3.9	Noise characteristics of the simulations	117

List of Frequently Used Symbols	
V	bias voltage
ψ	wavefunction
f	contact attempt frequency
s	distance between contact and dot
k	wavevector
T	background tunnelling rate
R	resonance function
α	tunnelling rate
β	relaxation rate
γ	recombination rate
o	dot level occupation
Subscripts	
c	contact (unspecified)
n	n-contact
p	p-contact
e	electron
h	hole
x	excited-state
g	ground-state

Chapter 1

Introduction

This thesis investigates computational and numerical approaches to modelling a system comprising of an array of quantum dots grown within the intrinsic region of a p-i-n junction. We study the effects of including various interactions in the model on the transport and electroluminescence (EL) characteristics of the system, and compare these to recent experimental results. We also present a theoretical investigation into a range of correlated tunnelling phenomena. This chapter introduces the important physics behind the basic system, and describes a sample of the recent experimental and theoretical work done in this field.

A semiconductor quantum dot is a nanostructure which confines the motion of a particle in all three spatial dimensions, effectively replicating the characteristics of an artificial atom. Quantum dots were first investigated over 20 years ago [1, 2], and the ability to modify their properties with relative ease has maintained their position at the forefront of condensed matter research ever since. [3]

1.1 Semiconductor p-i-n junctions

In an atom, when an electron feels a Coulomb force from a nucleus, the energy spectra of the electron has discrete energy levels. However, if the atoms are brought together to form a crystal, the electrons on each atom starts to feel the attractive force of the neighbouring nuclei. This leads the outer atomic energy levels to experience a broadening effect, until eventually we start to see the formation of continuous energy bands. [4]

The Schrodinger equation for electrons in the periodic potential of a semiconductor is:

$$\left[\frac{-\hbar^2}{2m} \nabla^2 + U(r) \right] \psi(\mathbf{r}) = E\psi(\mathbf{r}). \quad (1.1.1)$$

Whereas the tightly bound electrons in the inner core levels remain relatively unaffected, the electrons in the outer shell form a series of continuous bands. For Gallium Arsenide, this is occurs for the weakly bound electrons in the 4s and 4p shells. Each GaAs pair contributes 8 electrons into the newly formed energy band, which represents the solution of [1.1.1].

Figure 1.1.1 shows a schematic diagram showing the band structure forming around an array of individual atoms.

The allowed energy levels are not continuous as for the case of a free electron, but are split into regions of allowed bands separated by forbidden bandgaps. The two bands we are particularly interested in when studying semiconductor physics are the uppermost occupied or partly occupied band, known as the valence band, and the band immediately above it, known as the conduction band. The valence and conduction band are separated by a bandgap as shown in figure 1.1.2.

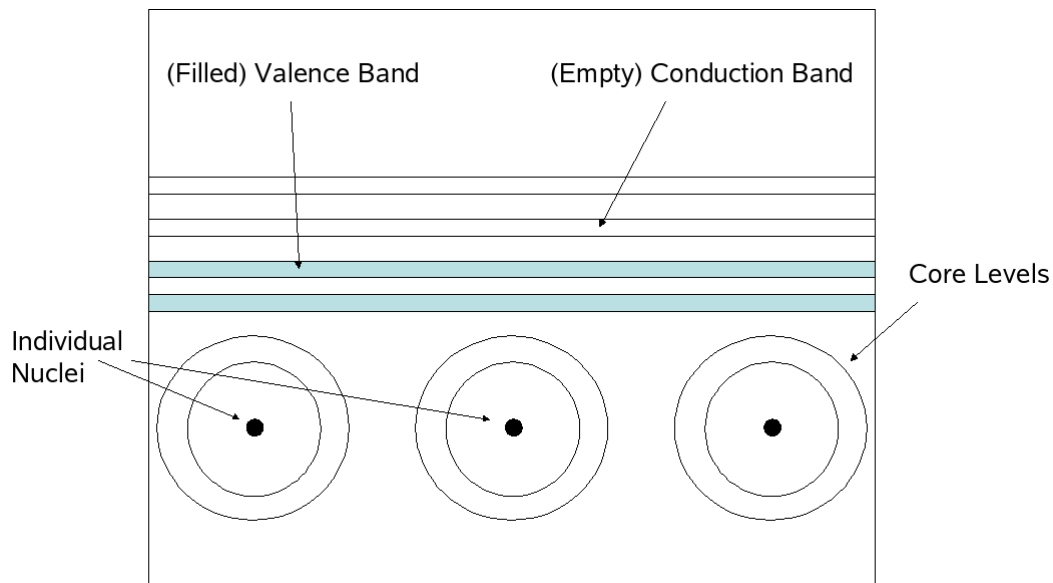


Figure 1.1.1: Bandstructure formation in crystalline solids

Depending on the exact nature of the material, how many electrons it donates to the bandstructure, and the exact solution of the Schrodinger equation, the valence band may be either entirely or partially filled with electrons. In order for the material to be able to conduct current, the electrons need available empty states into which they may move. A material with a completely full valence band will therefore have a far higher resistivity than a material with only a partially filled valence band, as there are no empty states to provide mobility. This is the key difference between an insulator and a metal, as shown in figure 1.1.3.

At non-zero temperature however, it is possible for the electrons of certain insulators to possess sufficient kinetic energy to be able to jump up into the empty conduction band, provided the band gap is small enough in comparison to the thermal energy ($E = k_B T$). Once in the conduction band, they are surrounded by empty states and are therefore able to move freely and thus conduct electricity. The electron also leaves behind a vacancy in the valence band, which will allow

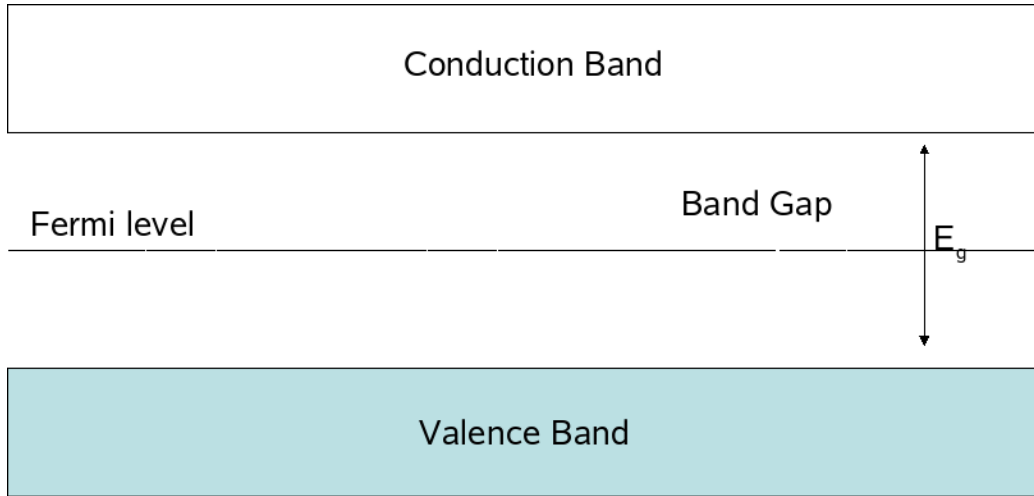


Figure 1.1.2: Valence and conduction bands and bandgap. The Fermi level can be seen mid-way between the 2 bands.

the remaining electrons to move more freely as a result, increasing the valence band conductivity in the process. This gap is called a hole, and can be understood as the equivalent of a positively charged particle moving in the opposite direction to the bulk motion of the electrons in the valence band. This system can be seen in figure 1.1.4.

The energy of carriers occupying the conduction and valence bands varies with the momentum of the carrier. In certain semiconductors, such as GaAs, the lowest energy point of the conduction band coincides with the point $k = 0$. Semiconductors with this property are known as direct semiconductors. The solution of the Schrodinger equation in such a semiconductor leads to the following relation between the energy and wavevector of the electron:

$$E(k) = E_c + \frac{\hbar^2 k^2}{2m^*}, \quad (1.1.2)$$

where m^* is the “effective” mass of the carrier. Near the band edges of the semi-

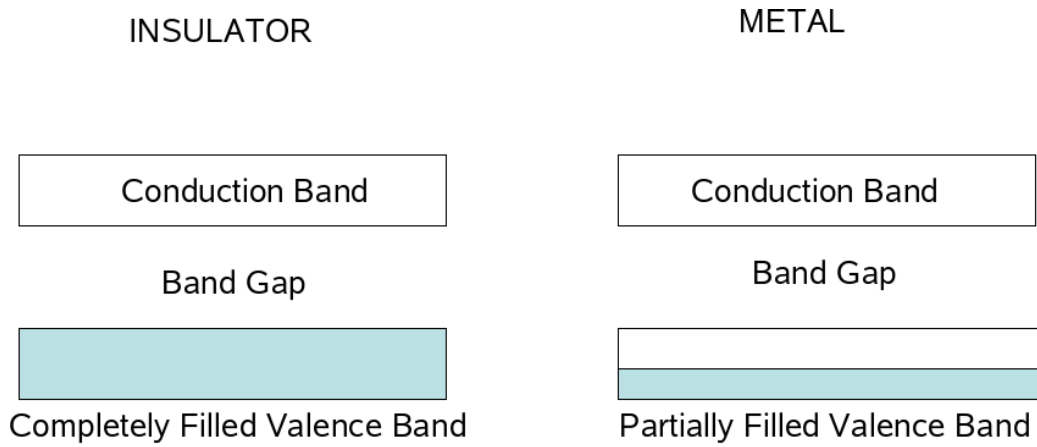


Figure 1.1.3: The conduction and valence bands for an insulator and a metal

conductor, the electrons and holes behave as if they have an effective mass, often significantly lower than the mass of an electron in free space [4].

The behaviour of the holes is slightly more complex than the behaviour of the electrons. We see three distinct $E(k)$ relationships within the valence band: known as the heavy hole band, the light hole band, and the split-off band. The effective mass of the holes is dependent upon which band they are occupying. Figure 1.1.5 shows the energy-wavevector relationship for GaAs. The energy gap (E_g) can be seen between the Γ valley in the conduction band and the heavy and light hole bands. In confined structures such as quantum dots, the heavy hole band and light hole band are split[5]. In the case of InAs, the heavy hole band ground state will shift enough to be disguised by overlapping in energy with the valence band. It is therefore the light hole band which we are particularly interested in.

The number of electrons in the conduction band, and the corresponding number of holes in the valence band, is dependant upon the temperature and the size of the bandgap of the semiconductor in question.

The intrinsic carrier concentration is given by [4]:

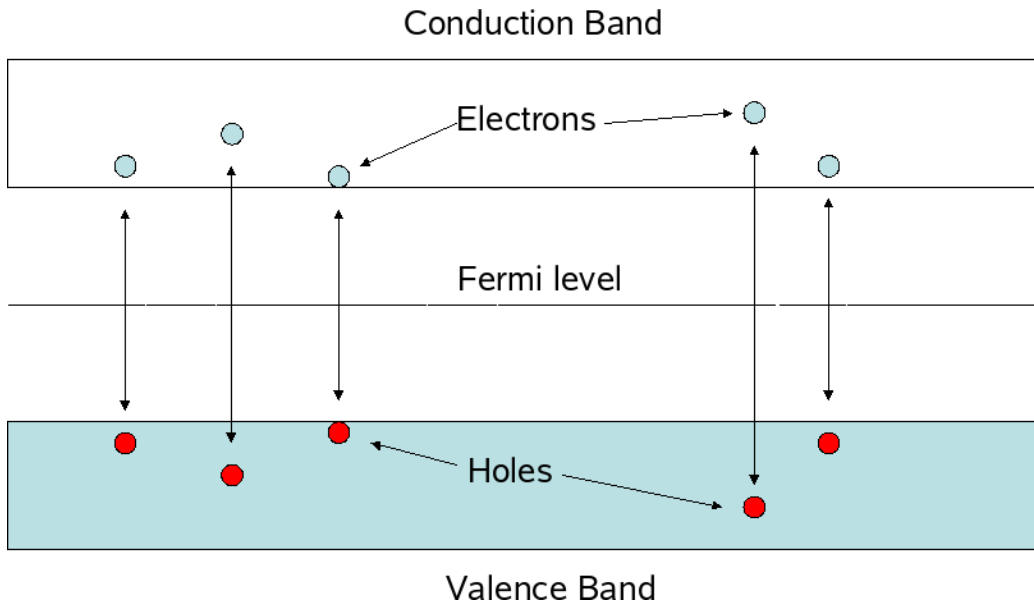


Figure 1.1.4: When an electron is excited into the conduction band, a hole is left behind in the valence band

$$n_i = N_c e^{(E_F - E_C)/k_B T}, \quad (1.1.3)$$

where the effective density of states is,

$$N_c = 2 \left[\frac{m^* k_B T}{2\pi \hbar^2} \right]^{3/2} \quad (1.1.4)$$

We can also calculate the Fermi energy of an intrinsic semiconductor as:

$$E_F = \frac{E_c + E_v}{2} + (3/4)k_B T \ln(m_h^*/m_e^*). \quad (1.1.5)$$

The Fermi energy of an intrinsic semiconductor therefore lies very close to the middle of the bandgap. This situation changes however, if we wish to change the distribution of electrons and holes within the material, creating an excess of

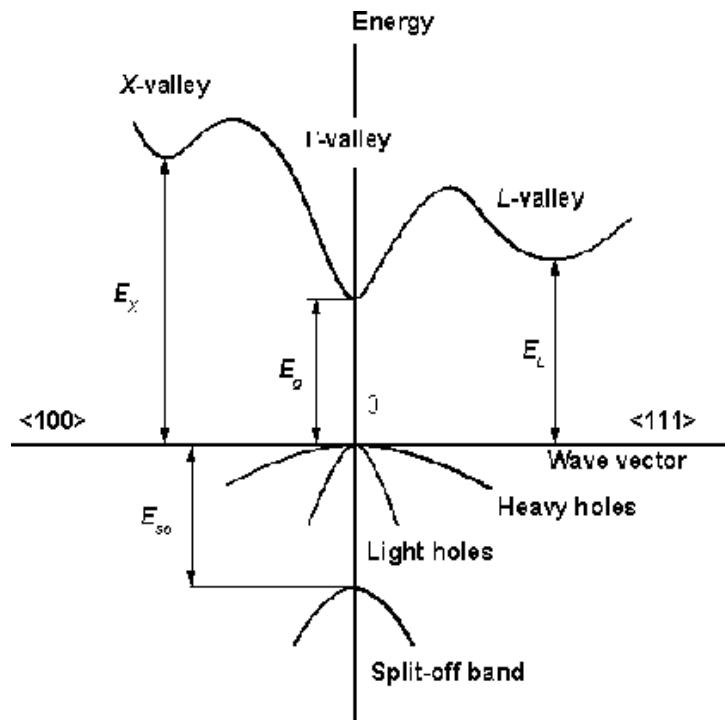


Figure 1.1.5: The energy-wavevector relationship in Gallium Arsenide. Figure taken from [6]

one species or the other. We do this using a process known as doping. Doping involves the addition of specific impurities to the semiconductor, which either donate electrons to the semiconductor leading to an electron excess, or accept electrons from it, leaving behind an excess of holes. This changes the carrier concentrations in the conduction and valence bands, and causes the Fermi level to shift to either just above the valence band (for acceptor ions) or just below the conduction band (for donor ions). We denote the two types of doping as positive (p) doping or negative (n) doping. A diagram of n-doped and p-doped semiconductors can be seen in figure 1.1.6.

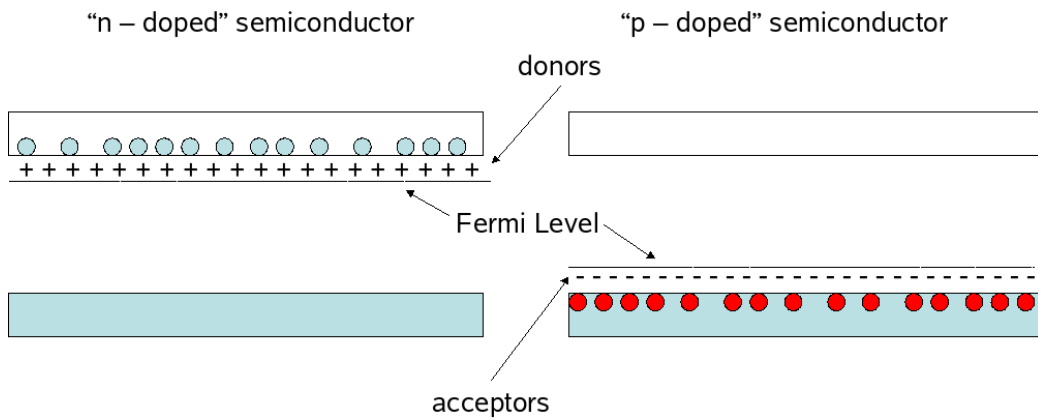


Figure 1.1.6: p doped and n doped semiconductors. The Fermi energy becomes pinned to the conduction and valence band by the presence of the acceptors and donors

The new Fermi level and carrier densities are related by:

$$n = n_i e^{(E_F - E_{F_i})/k_B T}. \quad (1.1.6)$$

If a p-doped semiconductor and an n-doped semiconductor are joined or grown in direct contact with each other, a number of things happen. The Fermi level, which is pinned to the conduction band edge in the n-doped region and the valence band edge in the p-doped region, will remain aligned, leading to a “bending” of the conduction band and valence band at the point where the two materials meet. This central region is known as the depletion region, and all the carriers present will be swept out by the built-in electric potential caused by the presence of the charged donors and acceptors on either side of the region. The slope of the potential can be modified by placing a layer of undoped (intrinsic) semiconductor between the two doped layers. This can be done to allow us to adjust the width of the effective depletion region, and reduce the severity of the slope in the band edges as necessary. This is now a p-i-n junction[4]. A diagram of a p-i-n junction

under zero bias is shown in figure 1.1.7.

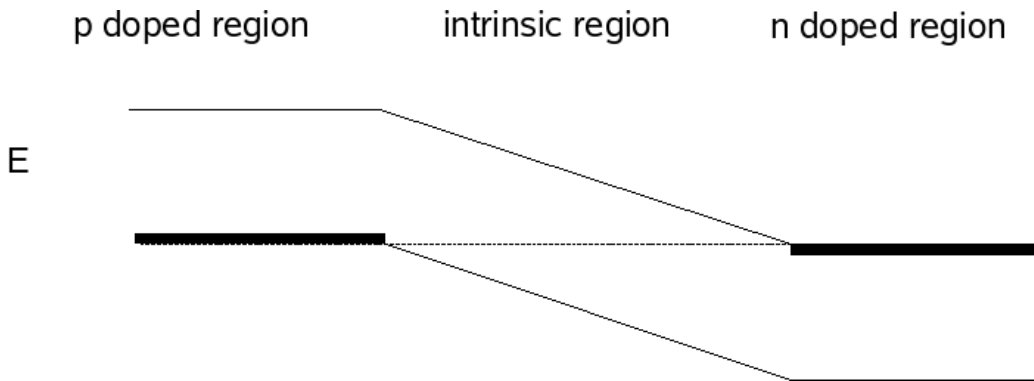


Figure 1.1.7: A p-i-n junction under zero volts. At 4.2 Kelvin, the Fermi level is pinned to the conduction and valence band edges, causing a slope in the band-structure in the intrinsic region.

As a positive or negative bias voltage is introduced across the junction, the pseudo-Fermi levels in the contacts are shifted relative to one another, leading to a change in the degree of the band bending. If a positive bias voltage is placed across the junction with a value equal to that of the energy gap (1.52eV in GaAs), then band bending will no longer occur. This is known as the flat band condition. Figure 1.1.8 shows the p-i-n junction under a positive bias of 1.52V.

1.2 Quantum Dots

Before we deal in detail with quantum dot devices, we must understand the underlying quantum mechanical theories. The two situations we are particularly interested in in this system involve two distinct cases: carriers that are spatially confined in all three directions in a zero-dimensional potential, and completely unconfined (free) carriers.

The solution of the Schrodinger equation for an unconfined electron, able to move in all three spatial dimensions, is given by:

$$\psi = e^{i(\mathbf{k}\cdot\mathbf{r}-\omega t)}, \quad (1.2.1)$$

with energy

$$E = \frac{\hbar^2(k_x^2 + k_y^2 + k_z^2)}{2m^*}. \quad (1.2.2)$$

In contrast to a free carrier, a carrier may be confined between two potential barriers, known as a quantum well. A quantum well is shown in figure 1.2.1. The electrons are confined to the three energy states within the well by the two barriers. The number of possible states within the well is dependent upon the width of the well and the height of the barriers.

We begin by imagining placing an electron in an infinite square well, confining it in all three dimensions. We find that the wavefunction will have the form[7]:

$$\psi = \sin\left(\frac{n_x\pi x}{L_x}\right)\sin\left(\frac{n_y\pi y}{L_y}\right)\sin\left(\frac{n_z\pi z}{L_z}\right), \quad (1.2.3)$$

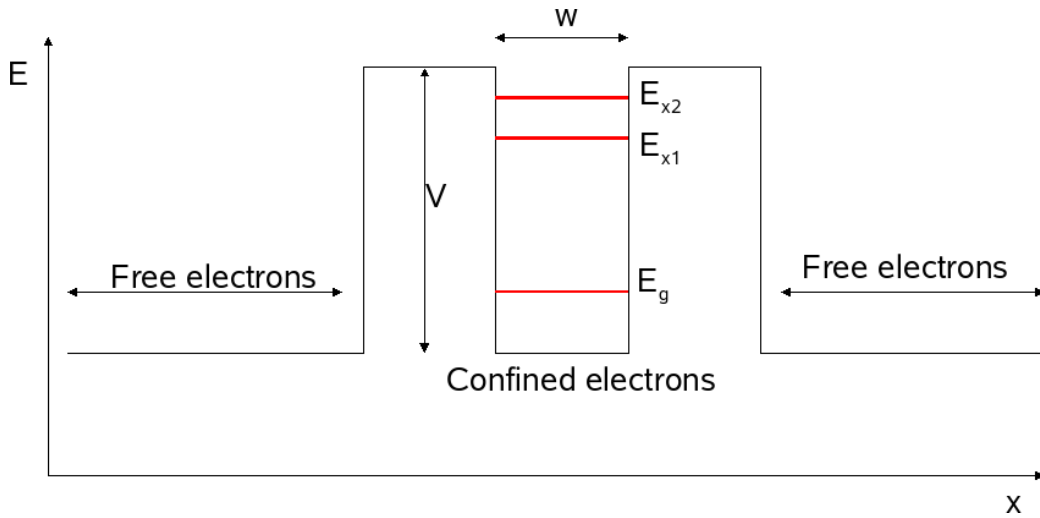


Figure 1.2.1: A diagram of the energy levels of a quantum well formed between 2 finite potential barriers with separation w

with energy levels given by:

$$E = \frac{\hbar^2 \pi^2 n_x^2}{8m^* L_x^2} + \frac{\hbar^2 \pi^2 n_y^2}{8m^* L_y^2} + \frac{\hbar^2 \pi^2 n_z^2}{8m^* L_z^2}. \quad (1.2.4)$$

If the barriers around the well are finite, then it is possible for the electron to penetrate the barrier and move through the classically forbidden region into or out of the well. In a system such as the one illustrated in figure 1.2.1, it is necessary for the electron approaching the well to possess the correct energy to occupy one of the free quantum states within the well. The tunnelling probability is therefore not only dependent upon the height and width of the barriers, but also on the “energy matching” between the approaching particle and the well energy levels.

In figure 1.2.2, we see an electron (1) approaching from the left. It has a non-zero probability of being reflected by the barrier (2), or, providing it possesses the correct energy, of penetrating both barriers and exiting the other side (3). [7]

One possible method of creating such a confining potential is to take advan-

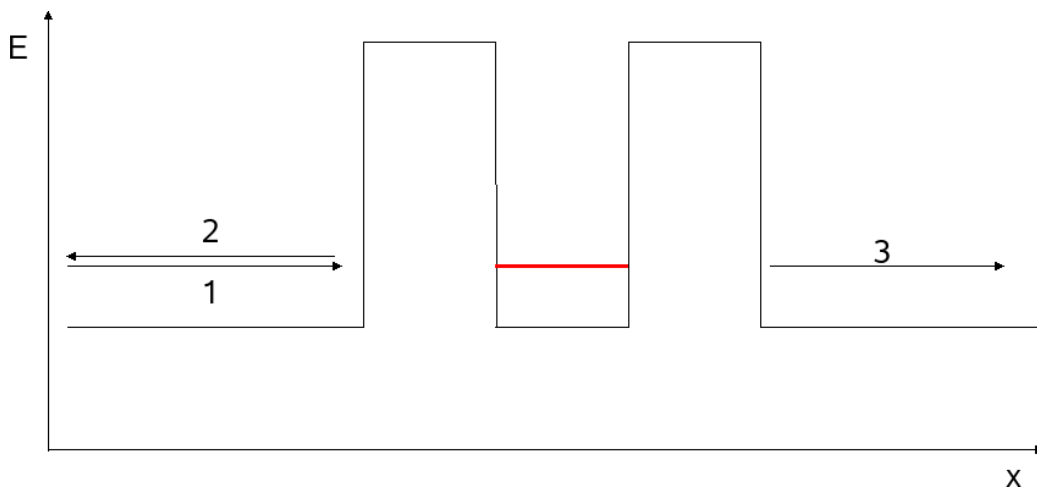


Figure 1.2.2: Tunnelling through a barrier into and out of a quantum well

tage of the different bandgaps between two otherwise closely related semiconductors. Two such suitable materials, and the two we will be studying, are Gallium Arsenide and Indium Arsenide. The lower bandgap of the InAs, sandwiched between two layers of the higher bandgap GaAs, creates a well in the conduction band of the material, enabling electrons to be trapped within, and an equivalent well in the valence band in which holes may be trapped. This configuration is shown in figure 1.2.3.

We will see in section 1.3 how it is possible to create islands of InAs within a GaAs substrate. This creates a zero dimensional quantum dot, in which the electron is strongly confined in all three spatial dimensions. Figure 1.2.4 shows an example of the x , y , and z energy levels which arise in a quantum dot. The energy of a carrier confined within the dot has energy equal to the sum of the confinement energies in each spatial dimension, as shown in [1.2.4]. In figure 1.2.4, we see a dot which is particularly tightly confined in the z direction, meaning no excited state is present in this spatial dimension.

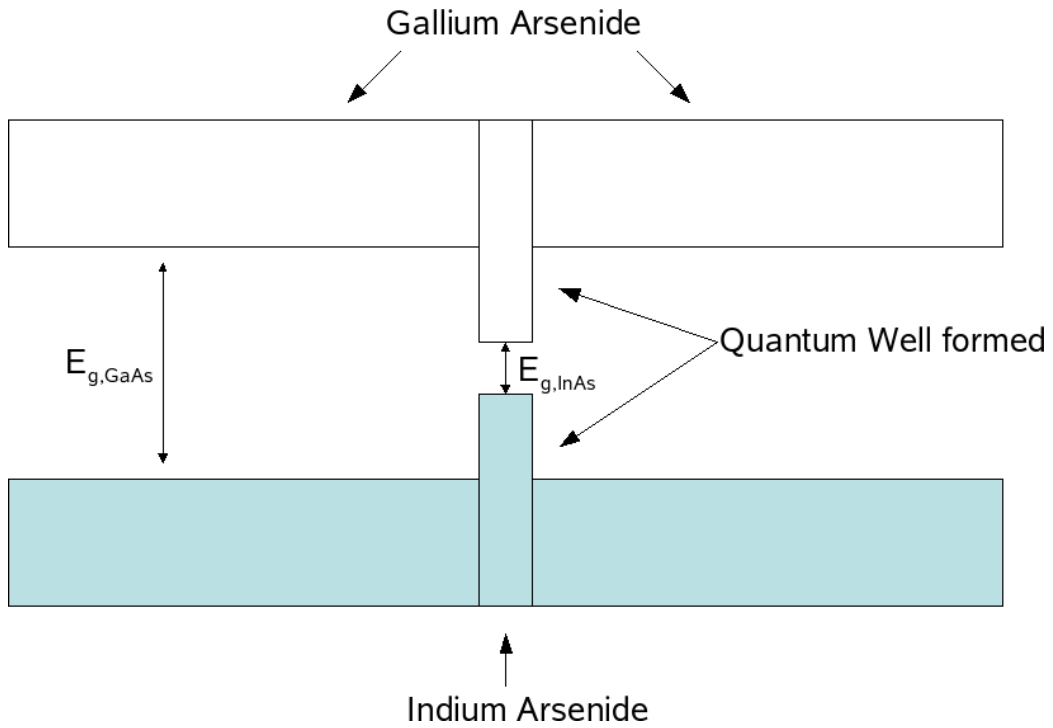


Figure 1.2.3: A quantum well formed by surrounding a layer of InAs with GaAs.

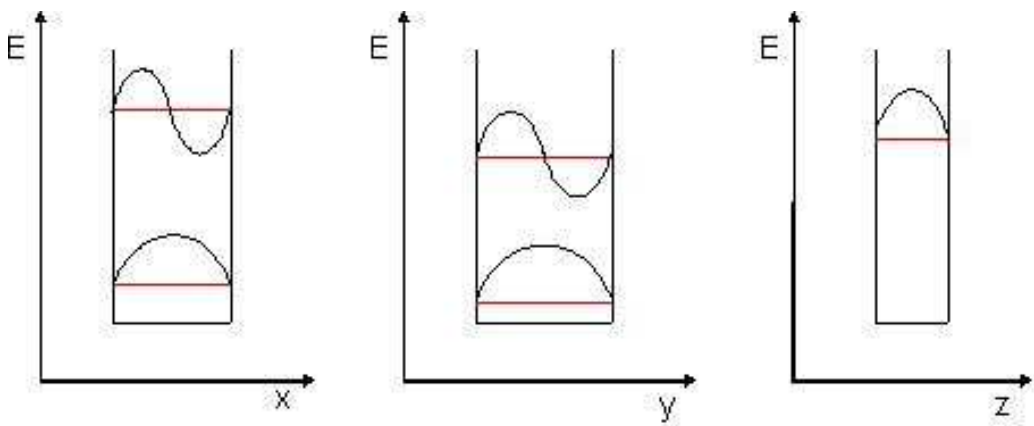


Figure 1.2.4: The bottom 2 energy levels in a dot for each dimension; if the dot is more tightly confined in the z axis, it is likely that there will be no excited states present.

Property	GaAs	InAs
Band Gap 300L (eV)	1.42	0.35
Band Gap 0K (eV)	1.52	0.42
Light Hole Effective Mass m_e	0.082	0.026
Electron Effective Mass m_e	0.067	0.022

Table 1.1: Material properties used in simulation

1.3 Experimental Information

A large motivation behind this work was the opportunity to work closely with an experimental group within the department. The exact specifications of the system we modelled were therefore specifically chosen to replicate the actual samples used in the experiments as closely as possible [8, 9]. The experimental samples were grown using molecular beam epitaxy (MBE) and Stransky-Krastanov growth. This is possible on materials such as GaAs and InAs because they have a lattice mismatch of approximately 7%. Both are III-V compounds with zinc-blend structure and direct band-gaps. The exact properties of GaAs, InAs and AlAs can be seen in table 1.1.

As the Indium Arsenide is deposited upon a Gallium Arsenide substrate using a standard MBE technique, initially a single layer of InAs forms, known as the wetting layer. As more material is deposited, the strain caused by the lattice mismatch between the two materials prevents further uniform growth and small islands of InAs are formed. The InAs MBE is then stopped, and the system is “capped” with a layer of GaAs. The InAs islands are now surrounded by GaAs, effectively making them quantum dots. By growing this layer within the intrinsic region of a p-i-n junction, the layout seen in figure 1.3.3 may be fully realised. Due to the process by which they have been grown, the quantum dots vary in size

by up to 5nm laterally and 2nm vertically, with an approximately Gaussian distribution. The formation and structure of the wetting layer and the morphology of the dots are important factors in the electronic structure and optical properties of the final system. Work is ongoing in these areas, see work done by Chen *et al* [11] and McGee *et al* [12].

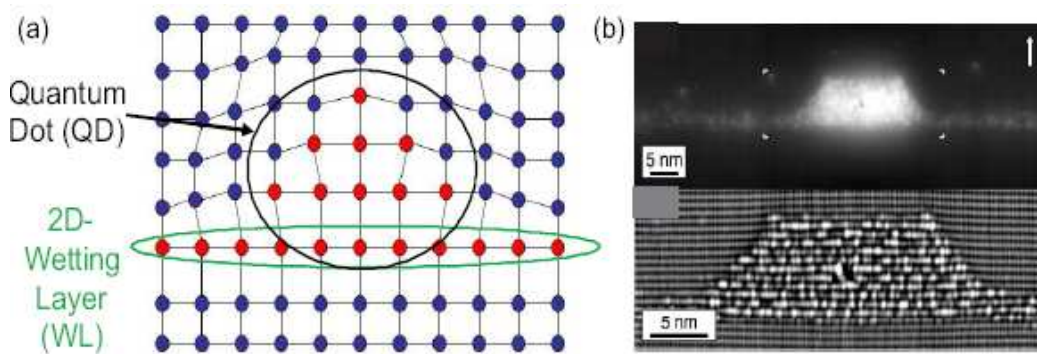


Figure 1.3.1: Stranski-Krastanov growth of InAs/GaAs quantum dots. Image taken from Gong *et al* (2004) [13].

The samples used in the experiments were grown in two batches. Batch A was grown in Sheffield by Prof. Mark Hopkinson, and batch B was grown in Nottingham by Prof. Mohammed Henini. Further details of the growth techniques used can be found in [8]. In samples containing dots, the InAs quantum dot layer was grown in the intrinsic region of a p-i-n junction, as shown in figure 1.3.2.

The samples were then analysed at the University of Nottingham by a group headed by Prof. Laurence Eaves and Dr. Amalia Patane [14, 15]. The samples were cooled using an Oxford Instruments continuous gas flow cryostat, capable of maintaining a temperature of 3.6 ± 0.05 K, and a vacuum pressure of 10^{-6} mbar. Magnetic field experiments were performed using a superconducting magnet capable of generating fields up to 14 T.

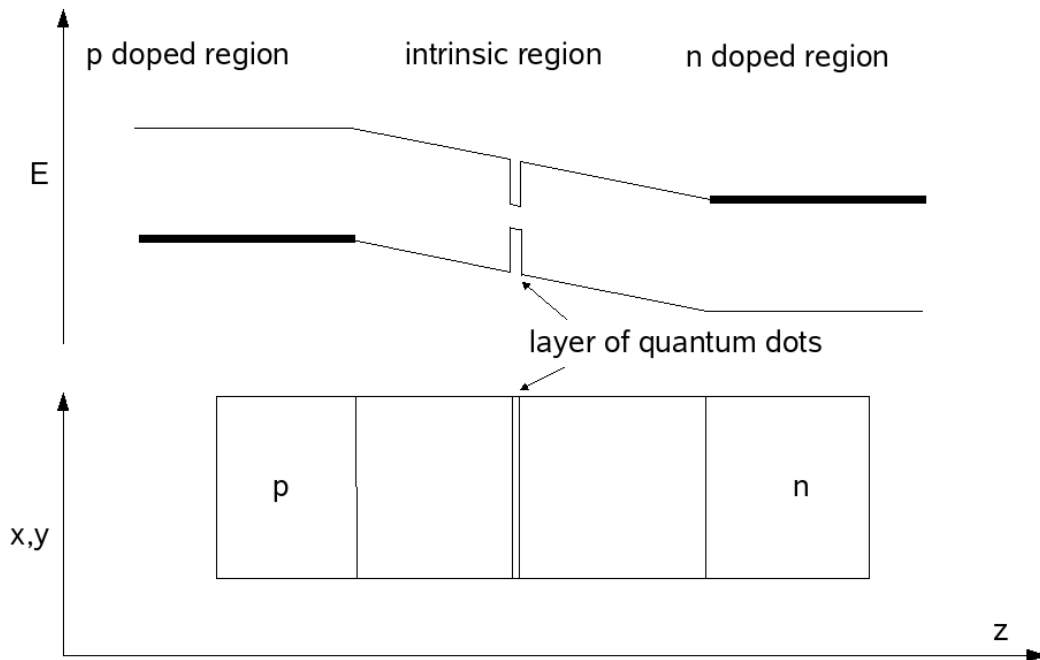


Figure 1.3.2: InAs dots within a p-i-n junction. The dots are confined approximately in the centre of the intrinsic region

For EL measurements, a Trias 550 series spectrometer and Si Charge Coupled Deviced Detector were used. This system is capable of a spectral resolution of 3.8meV, and is effective at detecting photons in the range 400-950nm.

The majority of IV measurements were performed using a Keithley 2400 digital multimeter, with a current sensitivity of approximately 100pA.

1.4 Outline of Thesis

In Chapter 2 we present the mathematical model we use to analyse the full system which forms the basis of the computational simulation seen in Chapter 3. First we model the quantum dots and calculate their energy levels using a quantum harmonic oscillator model. We then go on to calculate the electron and hole tunnelling rates into the dots from the n and p contacts using a WKB approximation, and the intradot recombination rate using Fermi's Golden Rule. Finally we present the full rate equations for all the processes in the system, and solve them analytically to find a steady state solution.

Chapter 3 goes into more detail about the exact method of implementing the model numerically. The simulation is based on a stochastic model, not dissimilar to the Monte Carlo method. First we generate an array of 2500 dots within a p-i-n junction and calculate all their relevant properties. We are then able to calculate the necessary rates of carriers moving into, within and out of the dots. A stochastic simulation is then used to find the populations of the dots, and this is then fed back into the system to update the relevant rates.

In Chapter 4, we now aim to improve our model by including the effects of the Coulomb interaction in the simulation, which have previously been neglected.

In Chapter 5 we analyse the model in more detail, and look at the effect of including some secondary interactions within the model, including studying changes in the spatial correlation length of the fluctuations in the Coulomb field, the inclusion of Auger processes in the model, and the effect of delayed and direct recombination on the simulated electroluminescence of the model.

Finally in Chapter 6 we study a particular regime seen in the results of the 2500

dot model involving correlated tunnelling of electrons and holes into the same dot, and use the master equation method to derive some of the key features of the process. We first study an isolated dot in this correlated tunnelling regime, and then expand the model to include two dots interacting with each other. We then use the master equation method to predict the current and current noise through a variety of situations.

Chapter 2

Mathematical Model

Here we present the mathematical model we use to analyse the full system which forms the basis of the computational simulation seen in Chapter 3. First we model the quantum dots and calculate their energy levels using a quantum harmonic oscillator model. We then go on to calculate the electron and hole tunnelling rates into the dots from the n and p contacts using a WKB approximation, and the intradot recombination rate using Fermi's Golden Rule. Finally, we present the full rate equations for all the processes in the system, and solve them analytically to find a steady state solution.

2.1 Quantum Dots

In section 1.2, we introduced the concept of a quantum dot formed by a small island of Indium Arsenide surrounded by Gallium Arsenide, and explained in section 1.3 how this could be achieved experimentally using Stranski-Krastanov epitaxial growth techniques. We now model these dots using a quantum harmonic os-

cillator model (QHO), as seen in figure 2.1.1. Other models, such as an infinite or finite square well are also valid approximations, but the division between the InAs and the GaAs at the boundaries of the dots is not perfectly rigid, and the change in potential on any occupying carrier can be seen as approximately parabolic. The effect of the deposition of the “capping layer” onto the dot acts to compress the dot on the z axis, implying a clearer potential division in this dimension. Therefore a two dimensional QHO model with infinite hard walls in the z axis remains the most logical and accurate of the soluble models [16, 17]. Much work has been done on characterising the electronic structure of dots, as this is an extremely important basis for understanding their optical properties [12, 18, 19, 20, 21].

The Quantum Harmonic Oscillator model used assumes the quantum dots have an approximately parabolic potential in the xy plane, with hard walls in the z axis:

$$V(\mathbf{r}) = \frac{1}{2}K\mathbf{r}^2 + V_0(z), \quad (2.1.1)$$

where K is a constant, and

$$V_0 = \begin{cases} 0 & |z| < d/2 \\ \infty & |z| > d/2 \end{cases}, \quad (2.1.2)$$

where d is the width of the dot along the z axis.

The general form of the wavefunction of an electron trapped in such a potential is:

$$\Psi_{l,m,n}(x, y, z) = \pi l_x l_y \sqrt{2^l l! 2^m m! l_z^{1/2}} e^{-\frac{x^2}{2l_x^2}} e^{-\frac{y^2}{2l_y^2}} H_l(x/l_x) H_m(y/l_y) \cos(n\pi z/l_z). \quad (2.1.3)$$

[17]

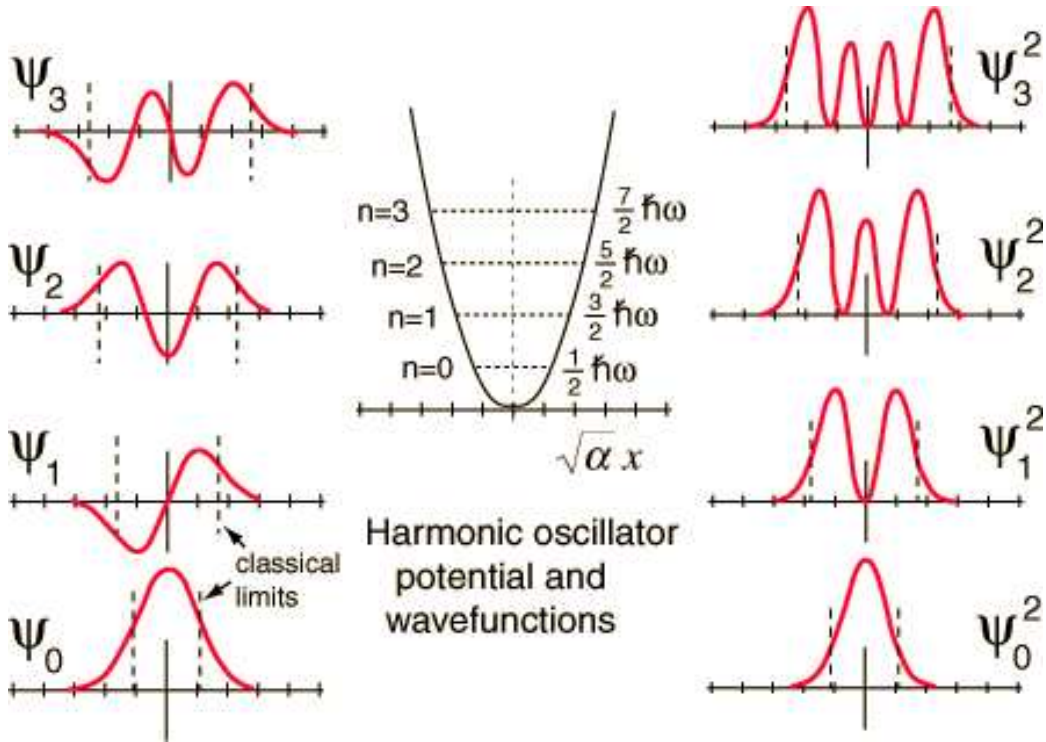


Figure 2.1.1: Diagram of a the groundstate and first three excited states of a 1D Quantum Harmonic Oscillator Model. Image taken from [22]

The electron and hole energy levels can be found in terms of the specific dimensions of the potential,

$$E_{lmn} = (l + m + 1)\hbar\omega_c + \frac{\hbar^2\pi^2 n^2}{2m^*l_z^2} \quad (2.1.4)$$

The ground states and first two excited states of an electron in a QHO can be

seen in figure 2.1.2. We must also be sure to include other relevant features seen in the experiment, such as the GaAs conduction and valence bands at 1.52eV, and also the “wetting layer” energy level with electron hole transition energies at 1.43eV [23, 24], as discussed in section 1.3. The conduction (valence) band and wetting layer energy levels are continuous levels: the carriers that occupy them are not confined to the dimensions of the dots, and they are available for resonant tunnelling at a wider value of energy levels than the dot states.

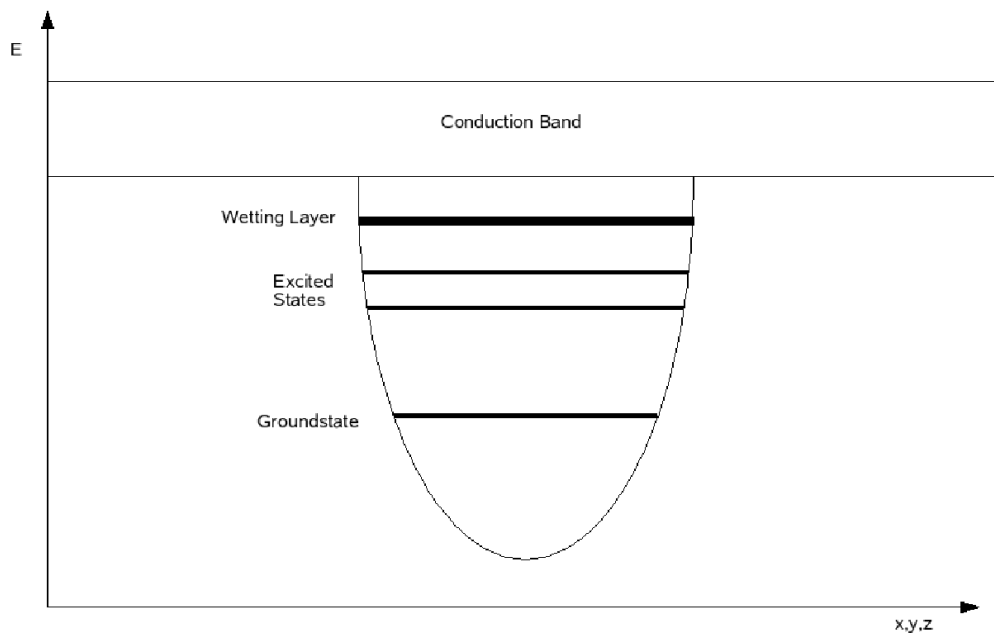


Figure 2.1.2: The energy levels included in the simulation

The dimensions of the quantum dots being modelled are distributed around a mean height, width and depth of $x=20\pm 3\text{nm}$, $y=20\pm 3\text{nm}$, and $z=3\pm 0.5\text{nm}$, where we define the dot array as lying in the xy plane. The total energy of the carrier in the dot is the sum of the energies for each dimension. The wetting layer energy falls between the first and second excited states in the x and y dimensions, and below the first excited state in the z dimension, which is higher than the conduction

band and thus merges into the continuum. Therefore there is one ground state and two excited states available for resonant tunnelling within each dot.

We also need to model the energy levels of the hole states within the InAs dot. These are slightly different to the electron levels as the holes occupy different sub-bands within the valence band. We need to consider the position of the light hole, heavy hole and cut-off bands, and which ones are relevant to the simulation. The holes occupying each sub-band will have different effective masses, which will directly affect their ability to tunnel into the dots, and the energy levels used [4]. This is accounted for when the hole levels are calculated.

2.2 Quantum Tunnelling

The physics of semiconductor p-i-n junctions were introduced in section 1.1, and the concept of inserting a layer of quantum dots within the intrinsic region was mentioned. A diagram of such an arrangement is shown in figure 2.2.1.

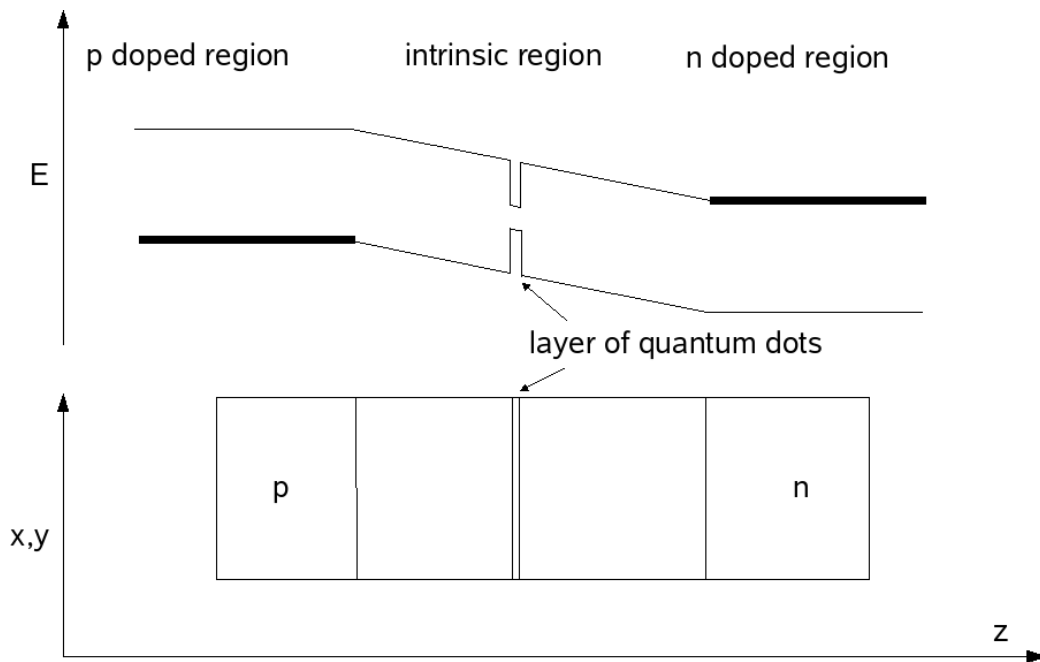


Figure 2.2.1: p-i-n junction with a layer of dots embedded within the intrinsic region

We see the layer of dots centrally located within the intrinsic region, and the populations of electrons and holes occupying the “n” doped and “p” doped regions respectively. In order to proceed, we must calculate the carrier populations from the doping concentrations of the two respective regions. From this we can then formulate the Fermi energy and attempt frequency at the experimental temperature of 4.2 Kelvin.

Experimentally doping concentrations are given as $N_A = 4 \times 10^{18} \text{ cm}^{-3}$ in the

p contact and $N_D=2 \times 10^{18} \text{cm}^{-3}$ in the n contact. From this we can calculate the electron (nn) and holes (pp) carrier densities [4]:

$$nn = N_D e^{-E_A/k_B T}, \quad (2.2.1)$$

and

$$pp = N_A e^{-E_D/k_B T}, \quad (2.2.2)$$

where E_A and E_D are the acceptor and donor level energies respectively.

We can now use the Joyce-Dixon approximation [4] to calculate the Fermi energies within the contacts:

$$E_{F_n} = k_B T \ln \left(\frac{nn}{N_C} \right) + \frac{nn}{\sqrt{8N_C}}, \quad (2.2.3)$$

where N_C is the density of states in the GaAs conduction band. The equivalent p contact equation is:

$$E_{F_p} = k_B T \ln \left(\frac{pp}{N_V} \right) + \frac{pp}{\sqrt{8N_V}}, \quad (2.2.4)$$

where N_V is the density of states in the GaAs valence band.

The Fermi velocity is therefore given by:

$$v_{F_{n(p)}} = \sqrt{2E_{F_{n(p)}}/m^*}. \quad (2.2.5)$$

From the carrier populations we can now calculate the electron (hole) attempt frequency, $f_{n(p)}$, for

$$f_{n(p)} = \left(\frac{1}{2} \right) nn(pp) v_{F_{n(p)}} \rho_{dots}, \quad (2.2.6)$$

where ρ_{dots} is the proportion of the xy plane of the intrinsic region taken up by the dots. The factor of 1/2 comes from the fraction of the carriers in the doped region moving both towards the intrinsic region at any given moment.

We may now calculate the tunnelling rate of the carriers moving into a particular dot i at resonance. We denote this rate as T_i , and use the WKB approximation, shown below:

$$T_{in(p)} = f_{n(p)} e^{-\int_0^{s_i} k(x) dx}, \quad (2.2.7)$$

where s_i is the distance between the contact and dot i , and k_i is the inverse decay length of the carrier in the intrinsic region. [7]

In order to calculate s_i and k_i , we must make a simple model of the section of the intrinsic region the carriers tunnel through between the contact and the dot in question. We do this using a triangular barrier approximation, as shown in figure 2.2.2.

We see that the potential the carrier must tunnel through is dependant upon the bias voltage. As the voltage increases towards flat band conditions, the barrier effectively becomes lower and narrower, leading to an exponential increase in the tunnelling rate.

The tunnelling distance, s_i varies according to

$$s_i(V) = s_i(0) \frac{(E_{GaAs} - V)}{E_{GaAs}}, \quad (2.2.8)$$

where E_{GaAs} , the energy gap of the GaAs substrate, has a value of 1.52eV, and the

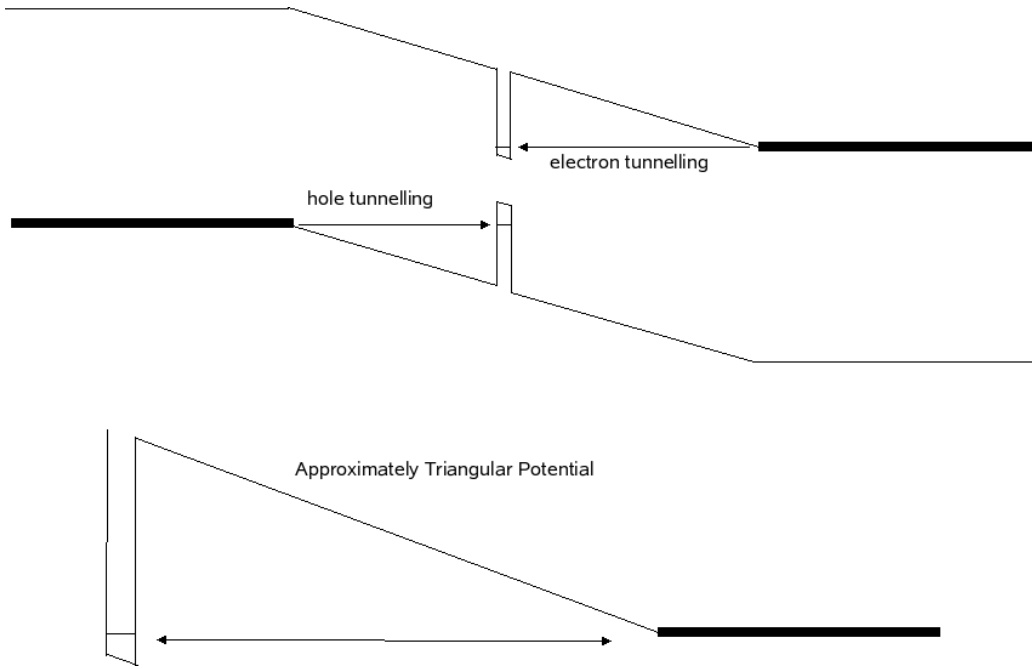


Figure 2.2.2: Model of a triangular barrier

wavevector in the barrier k_i varies by

$$k_i(V) = \sqrt{\frac{2m^*(E_{GaAs} - V)(s_i(V) - x)}{\hbar}}. \quad (2.2.9)$$

This gives us a tunnelling rate of

$$T_{in(p)} = f_{n(p)} e^{-\sqrt{\frac{8m^*3}{\hbar^2}}}, \quad (2.2.10)$$

Therefore we are able to calculate how the tunnelling rate changes with bias voltage, and for a range of starting size dimensions. Simply by adjusting some of the initial parameters, we are able to calculate the effect on the rate of the system temperature, the dot distribution density, the size of the intrinsic region, and the position of the dot array within that region. The effect of changing bias voltage

on the p-i-n junction can be seen in figures 2.2.3, 2.2.4 and 2.2.5.

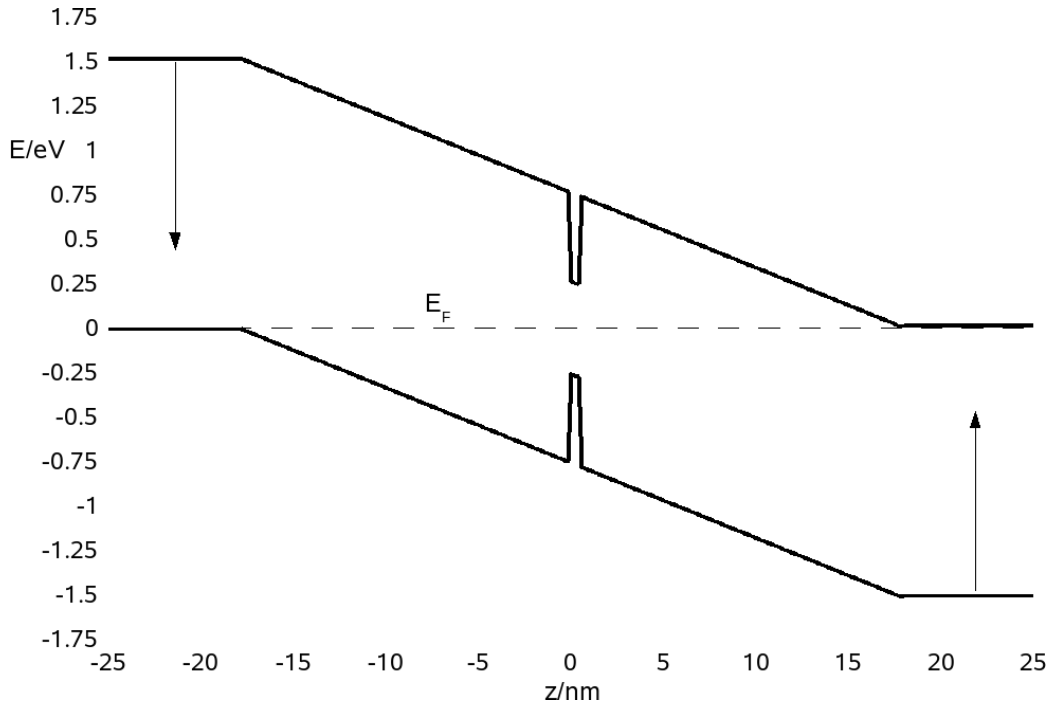


Figure 2.2.3: p-i-n junction at zero Volts

Of course, the carriers are only able to tunnel into dots when the bias voltage is such that they possess the correct energy for resonant tunnelling to occur. We must now take into account the effect of this. The width of this resonance can be calculated from the overlap of the dot state energies and the contact Fermi energies at the experimental system temperature of 4.2K. The resonance function, R_{ij} , for energy level j and dot i , is related to the overlap in energy between the carrier states in the contact and on the dot [25]:

$$R_{ij}(V) = A_{ij}F(E/eV)D(E)\delta(E - E_{ij}), \quad (2.2.11)$$

where $F(E/eV)$ is the Fermi distribution at 4.2 K and voltage V , $D(E)$ is the

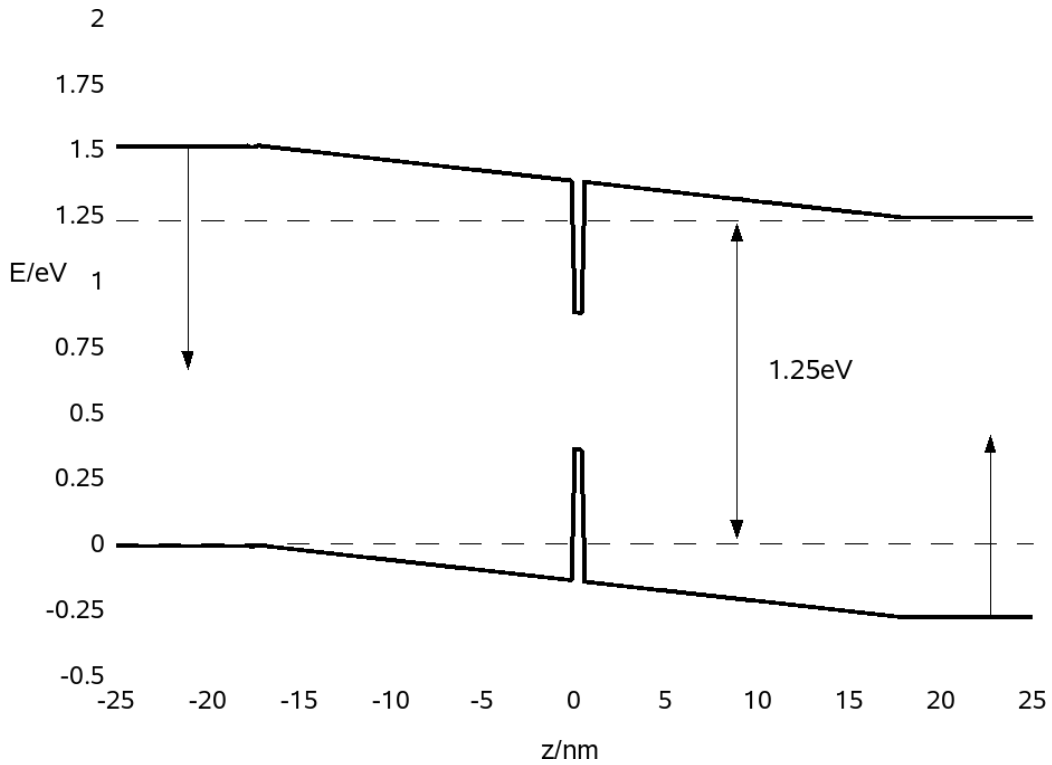


Figure 2.2.4: p-i-n junction at typical resonant bias voltage of 1.25 V

density of states in the conduction/valence band, and A_{ij} is a normalisation constant, which sets $R_{ij}(V) = 1$ at the exact moment of resonance. If the voltage is adjusted away from this point, the tunnelling current falls away sharply on either side.

A simple diagram showing resonant tunnelling can be seen in figure 2.2.6.

The final tunnelling current into energy level j of dot i , α_{ij} can therefore be calculated, by combining the background tunnelling rate T_i and the normalised resonance function R_{ij} . All the rates have a dependence on the bias voltage of the system

$$\alpha_{ij}(V) = T_i(V)R_{ij}(V). \quad (2.2.12)$$

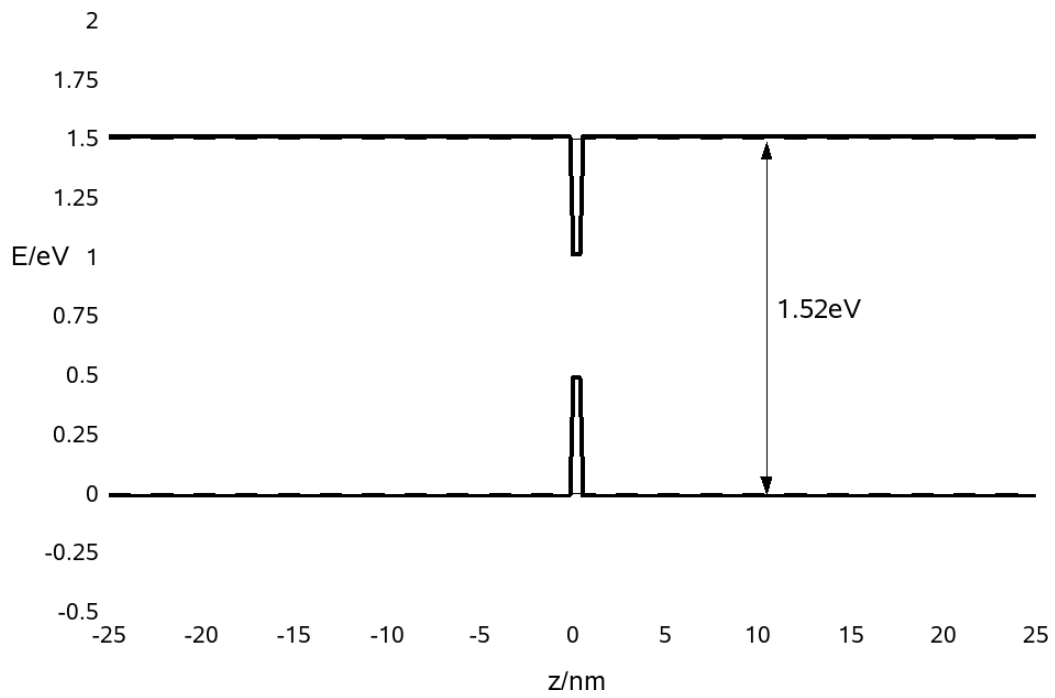


Figure 2.2.5: p-i-n junction at 1.52V (flat band conditions)

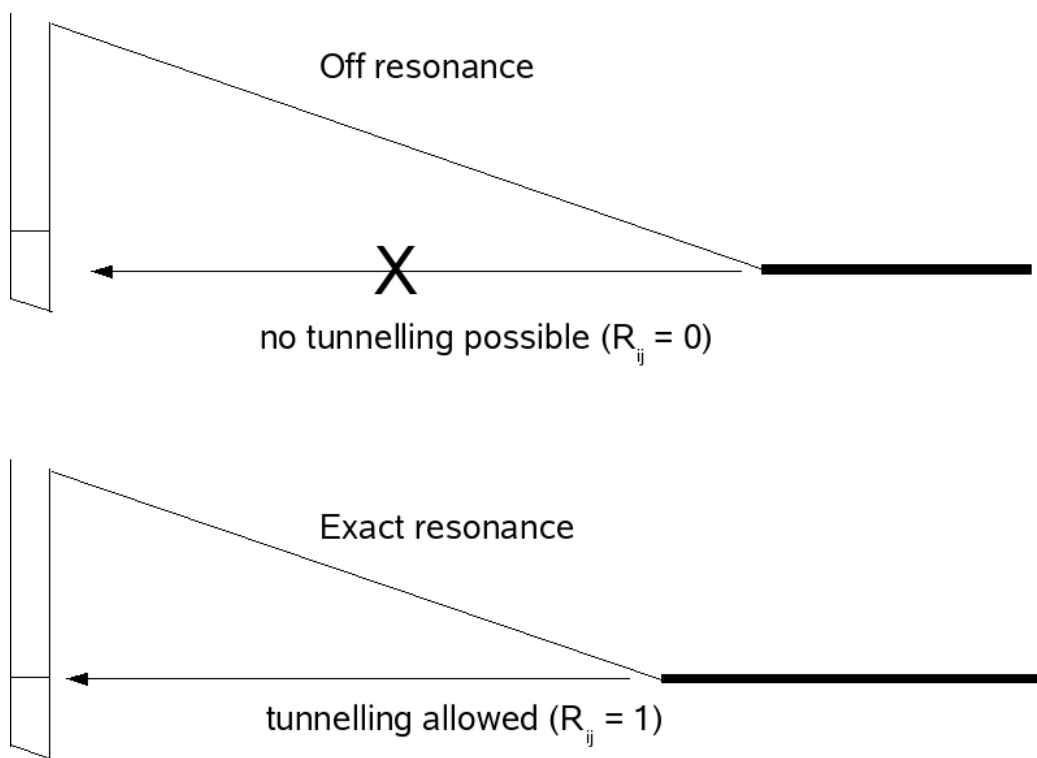


Figure 2.2.6: resonant tunnelling

2.3 Recombination Processes

Now we have calculated the rate at which electrons and holes can tunnel from the contacts and into the dot array, we need to calculate the rate at which they spontaneously recombine. There are two main processes involved. Firstly, if the dots tunnel into an excited state or a higher level such as the wetting layer or conduction/valence band, they are able to “relax” into a lower level [26, 27], typically the unoccupied groundstate of an individual dot, through interaction with an LO phonon. For this process to occur, the gap in energy levels needs to be close to an integer multiple of the GaAs LO phonon energy, which is 36meV [28].

Secondly, if there are an electron and a hole occupying the same dot, it is possible for excitonic recombination to occur, emitting a photon. This is the process we address first.

If there is an exciton present on a dot, or spatially aligned in the wetting layer or conduction/valence bands, there is a possibility of spontaneous radiative recombination. We denote this process γ_{ij} , and the probability of it occurring is calculated according to Fermi’s Golden Rule, by formulating the overlap integral between the two states in question [7].

The transition $\psi_e \gamma^\dagger \psi_h$ can be found by calculating the dipole transition matrix element between the electron and hole pair states.

Using Fermi’s Golden Rule, we can calculate the transfer rate between the two states, which we can see is proportional to the overlap integral between them, in this case the electron state, ψ_{ije} and the hole state, ψ_{ijh} .

$$\gamma_{ijk} = \frac{e^2 \omega^3}{8\pi \epsilon \hbar c^3} \psi_{ije} \cdot \psi_{ijh} \quad (2.3.1)$$

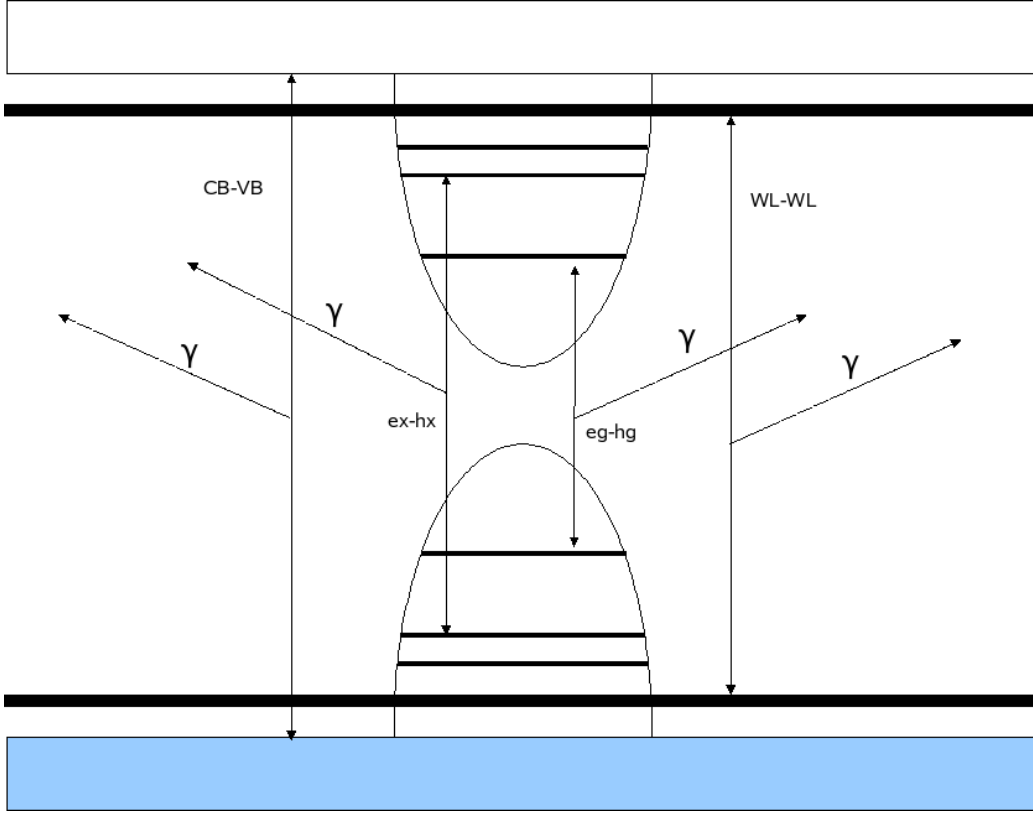


Figure 2.3.1: Excitonic Recombination within a dot

In section 2.1, we defined the electron groundstate wavefunction as

$$\psi_{000} = \pi l_x l_y l_z^{1/2} e^{-\frac{x^2}{2l_x^2}} e^{-\frac{y^2}{2l_y^2}} H_0(x/l_x) H_0(y/l_y) \cos(\pi z/l_z). \quad (2.3.2)$$

We also know that the first electron excited state [7] looks like:

$$\psi_{010} = \pi l_x l_y \sqrt{2} l_z^{1/2} e^{-\frac{x^2}{2l_x^2}} e^{-\frac{y^2}{2l_y^2}} H_0(x/l_x) H_1(y/l_y) \cos(\pi z/l_z). \quad (2.3.3)$$

By calculating this integral numerically, we can see that the transition rate for recombination of electrons and holes is considerably higher if the carriers are

occupying equivalent states, as the overlap integral between them will necessarily be far greater. Groundstate to groundstate and excited state to excited state transfer therefore occurs at a considerably quicker rate than between an excited state and a ground state.

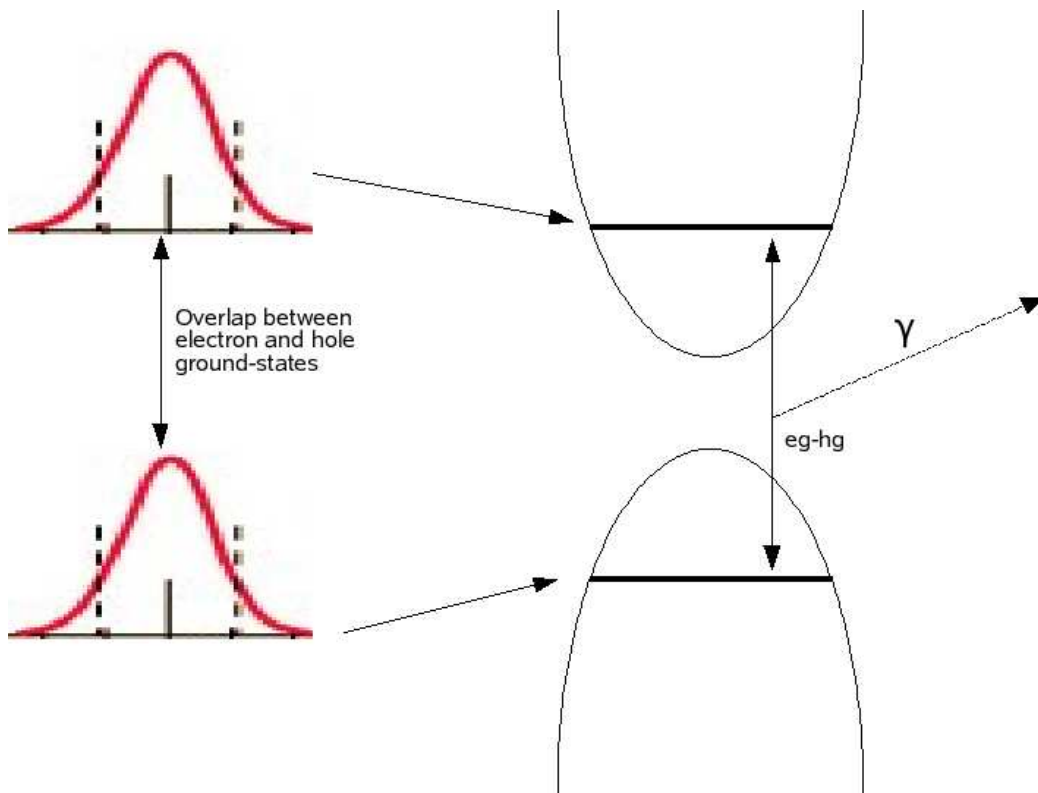


Figure 2.3.2: Overlap integrals between energy levels

Once the exciton recombines, a photon is emitted. The energy of the photon is equal to the difference in energies between the two states in question. For groundstate to groundstate recombination, the energy of the emitted photon is in the region of 1.25eV.

Figure 2.3.3 shows the possible phonon assisted relaxation pathways within a quantum dot. For a system with five energy levels, there are ten such pathways.

Each relaxation process $\psi_g^\dagger \beta^\dagger \psi_x$ involves the emission of an LO phonon (labelled as β) with an energy equal to the drop in energy between the two levels involved in the process. As seen in section 1.3, the energy of an LO phonon in GaAs is 36meV, so phonon assisted relaxation can only occur when the gap between the states is close to an integer multiple of this energy. This includes carriers in the conduction/valence band and wetting layer which become trapped in the dot. As we only consider a first excited state for the x and the y wavefunction components, selection rules preventing same parity relaxation are not applicable.

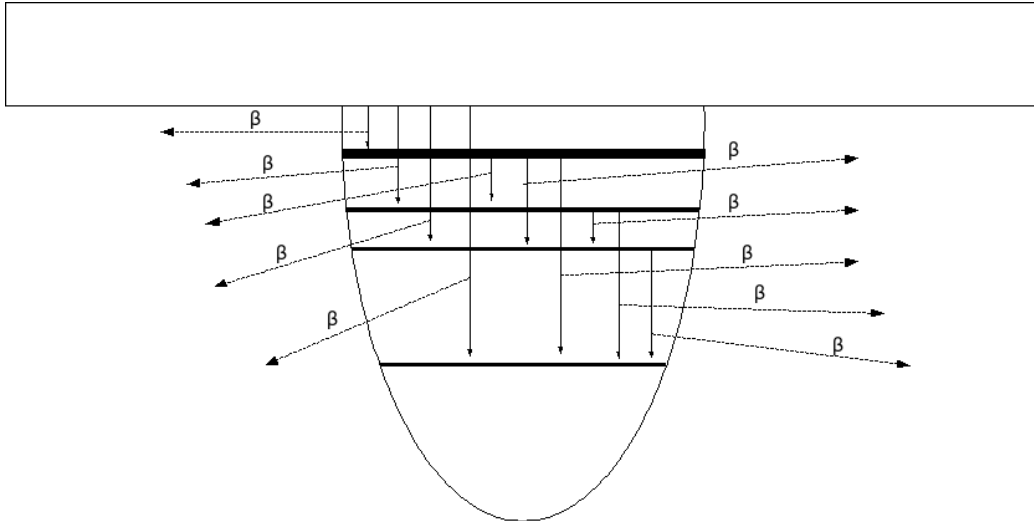


Figure 2.3.3: Phonon Assisted relaxation mechanism

We must also take into account the concept of the “phonon bottleneck” effect. It is known that although this has a noticeable effect in intra-dot relaxation dynamics, it is not sufficient to reduce the intra-dot relaxation rate enough to make the timescale comparable to the excitonic recombination rate [29]. Therefore for the purposes of our simulation, we choose to neglect this effect.

2.4 Full Rate Equations

We have now identified the three key processes that shape the evolution of the system: carriers tunnelling from the contacts into the dots, which we denote as process α , phonon assisted relaxation between states within the dot, denoted as process β , and excitonic recombination, denoted as γ . In order to analyse further, we simplify the system to a four level system, with a single groundstate (g) and excited state (x) for electrons (e) and holes (h). The population of the contact (c) is also necessary. o denotes the occupancy of the state in question. The full rate equations are:

$$\frac{do_{xe}}{dt} = \alpha_{xe}o_{ce}\left(1 - \frac{o_{xe}}{2l}\right) - \beta_e o_{xe}\left(1 - \frac{o_{ge}}{2l}\right) - \gamma_x o_{xe}o_{xh}, \quad (2.4.1)$$

$$\frac{do_{xh}}{dt} = \alpha_{xh}o_{ch}\left(1 - \frac{o_{xh}}{2l}\right) - \beta_h o_{xh}\left(1 - \frac{o_{gh}}{2l}\right) - \gamma_x o_{xe}o_{xh}, \quad (2.4.2)$$

$$\frac{do_{ge}}{dt} = \alpha_{ge}o_{ce}\left(1 - \frac{o_{ge}}{2l}\right) + \beta_e o_{xe}\left(1 - \frac{o_{ge}}{2l}\right) - \gamma_g o_{ge}o_{gh}, \quad (2.4.3)$$

$$\frac{do_{gh}}{dt} = \alpha_{gh}o_{ch}\left(1 - \frac{o_{gh}}{2l}\right) + \beta_h o_{xh}\left(1 - \frac{o_{gh}}{2l}\right) - \gamma_g o_{ge}o_{gh}. \quad (2.4.4)$$

We can now proceed further and define a full Hamiltonian for the system. We define the dot array to be the system of the Hamiltonian, which interacts with its environment by way of the three process, α , β and γ .

We will now use an approach known as the master equation method. This is an open systems approach to quantum mechanics, which makes it possible to

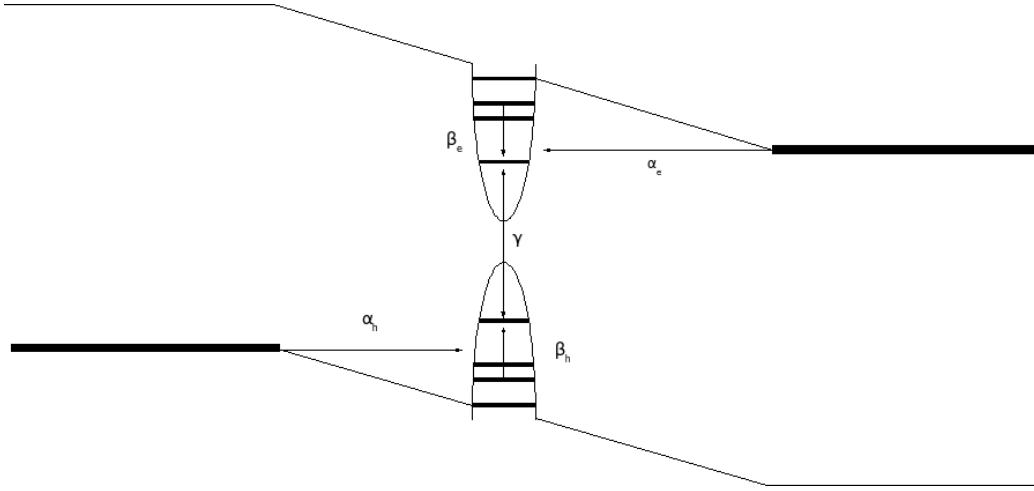


Figure 2.4.1: Totality of Processes used in Model

solve complex problems by separating the system, the evolution of which we are interested in, from the environment, the evolution of which we are not. We proceed by describing the problem in terms of the system, S , the “bath”, B , and the interactions between them, I . We define Hamiltonians for each term, and isolating the density matrix of the system, $\rho(t)$ from the total density matrix $\chi(t)$.

The Hamiltonian can be split into the system Hamiltonian, the bath Hamiltonian and the interaction Hamiltonian:

$$\hat{H}_{tot} = \hat{H}_B + \hat{H}_S + \hat{H}_I \quad (2.4.5)$$

We then define:

$$\hat{H}_B = \sum_{i,j} \left\{ \varepsilon_{\alpha ij} \alpha_{ij}^\dagger \alpha_{ij} + \varepsilon_{\beta i} \beta_i^\dagger \beta_i + \varepsilon_{\gamma j} \gamma_j^\dagger \gamma_j \right\} \quad (2.4.6)$$

$$\hat{H}_S = \sum_{i,j,k} \varepsilon_{ij} a_{ijk}^\dagger a_{ijk} \quad (2.4.7)$$

$$\hat{H}_I = \sum_{i,j,k} \varepsilon_{\alpha_{ij}} a_{ijk}^\dagger \alpha_{ijk} + \varepsilon_{\beta_i} a_{gik}^\dagger a_{xik} \beta_i^\dagger + \varepsilon_{\gamma_j} a_{ejk} a_{hjk} \gamma_j^\dagger. \quad (2.4.8)$$

The index i denotes electron or hole states, j denotes excited or ground states and k denotes spin up or spin down states. a_{gik}^\dagger and a_{ijk} are thus the Fermionic creation and annihilation operator for the system state ijk . α_{ij}^\dagger and α_{ij} are the creation and annihilation operators for the carriers in the leads, β_i^\dagger and β_i are the bosonic creation and annihilation operators for the phonons associated with the relaxation process, and γ_j^\dagger and γ_j are the bosonic creation and annihilation operators for the photons emitted by excitonic recombination. The factor ε represents the associated energy with each state or process.

We also define

$$\hat{H}_0 = \hat{H}_S + \hat{H}_B. \quad (2.4.9)$$

If we assume that the spin up and spin down carriers operate independantly, we are able to suppress the third index k , and are then able to compile a list of 16 system states, which can be defined in terms of which combination of the four energy levels are occupied by a carrier, shown in figure 2.4.2.

We define the relationship between $\chi(t)$, the total density matrix of the system and $\rho(t)$, the reduced density matrix to be

$$\rho(t) = Tr_B(\chi(t)). \quad (2.4.10)$$

We also define the initial bath density matrix to be

$$R(0) = Tr_S(\chi(0)). \quad (2.4.11)$$

system state	ex	eg	hx	hg
0	0	0	0	0
1	0	0	0	1
2	0	0	1	0
3	0	0	1	1
4	0	1	0	0
5	0	1	0	1
6	0	1	1	0
7	0	1	1	1
8	1	0	0	0
9	1	0	0	1
10	1	0	1	0
11	1	0	1	1
12	1	1	0	0
13	1	1	0	1
14	1	1	1	0
15	1	1	1	1

Therefore, by making the Born approximation, we are able to trace out the unwanted parts of the ensemble. The Born approximation states that the Bath is large enough to remain unaffected by any changes in the state of the system, and therefore does not evolve in time. Therefore we can use the initial bath density matrix for the entirety of the model. We can now find a steady state solution for the dot system itself. This can be achieved using a master equation approach[30], where the master equation describing the evolution of $\rho(t)$ is given by the Liouville operator:

$$\dot{\rho}(t) = \mathcal{L}\rho(t). \quad (2.4.12)$$

Because $\rho(t)$ does not contain any off diagonal elements, we are able to simplify this expression by taking the trace of $\rho(t)$ and converting it into a vector. In turn, this means that

We wish to find the matrix \mathcal{L} , which controls the evolution of the system in

time. To do this, we need to use the Markov approximation, which states that the future time evolution of the system is only dependant upon the present state of the system and not on any previous states. This means that the bath must be large enough to absorb any fluctuations without reflecting them back to the system. We can now define the interaction Hamiltonian as a sum over a set of general system and bath operators:

$$\hat{H}_I = \sum_i S_i \otimes B_i. \quad (2.4.13)$$

Having defined the system and bath operators for each index i , we convert them into the interaction picture using the relationship:

$$S = e^{iH_0t/\hbar} S e^{-iH_0t/\hbar} \quad (2.4.14)$$

We now calculate the bath correlation functions using the equation:

$$C_{kl}(t, t') = Tr_B [B_k(t) B_l(t') R_0] \quad (2.4.15)$$

From this point, we can derive the equation of motion for ρ :

$$\frac{d}{dt} \rho(t) = -i [H_S, \rho(t)] - \sum_k (S_k D_k \rho(t) - D_k \rho(t) S_k + \rho(t) E_k S_k - S_k \rho(t) E_k), \quad (2.4.16)$$

where we define D_k as

$$D_k = \lim_{t \rightarrow \infty} \int_0^t d\tau \sum_l C_{kl}(\tau) S_l(-\tau) \quad (2.4.17)$$

and E_k as

$$E_k = \lim_{t \rightarrow \infty} \int_0^t d\tau \sum_l C_{lk}(-\tau) S_l(-\tau). \quad (2.4.18)$$

We therefore find \mathcal{L} to be:

$$\left(\begin{array}{cccccccccccccccc} X_0 & 0 & 0 & 0 & 0 & 0 & \gamma_g & 0 & 0 & \gamma_x & 0 & 0 & 0 & 0 & 0 & 0 \\ \alpha_{hx} & X_1 & 0 & 0 & 0 & 0 & 0 & \gamma_g & 0 & 0 & 0 & 0 & 0 & 0 & 0 & 0 \\ \alpha_{hg} & \beta_h & X_2 & 0 & 0 & 0 & 0 & 0 & 0 & 0 & 0 & \gamma_x & 0 & 0 & 0 & 0 \\ 0 & \alpha_{hg} & \alpha_{hx} & X_3 & 0 & 0 & 0 & 0 & 0 & 0 & 0 & 0 & 0 & 0 & 0 & 0 \\ \alpha_{eg} & 0 & 0 & 0 & X_4 & 0 & 0 & 0 & \beta_e & 0 & 0 & 0 & 0 & \gamma_x & 0 & 0 \\ 0 & \alpha_{eg} & 0 & 0 & \alpha_{hx} & X_5 & 0 & 0 & 0 & \beta_e & 0 & 0 & 0 & 0 & 0 & 0 \\ 0 & 0 & \alpha_{eg} & 0 & \alpha_{hg} & \beta_h & X_6 & 0 & 0 & 0 & \beta_e & 0 & 0 & 0 & 0 & \gamma_x \\ 0 & 0 & 0 & \alpha_{eg} & 0 & \alpha_{hg} & \alpha_{hx} & X_7 & 0 & 0 & 0 & \beta_e & 0 & 0 & 0 & 0 \\ \alpha_{ex} & 0 & 0 & 0 & 0 & 0 & 0 & 0 & X_8 & 0 & 0 & 0 & 0 & 0 & \gamma_g & 0 \\ 0 & \alpha_{ex} & 0 & 0 & 0 & 0 & 0 & 0 & \alpha_{hx} & X_9 & 0 & 0 & 0 & 0 & 0 & \gamma_g \\ 0 & 0 & \alpha_{ex} & 0 & 0 & 0 & 0 & 0 & \alpha_{hg} & \beta_h & X_{10} & 0 & 0 & 0 & 0 & 0 \\ 0 & 0 & 0 & \alpha_{ex} & 0 & 0 & 0 & 0 & 0 & \alpha_{hg} & \alpha_{hx} & X_{11} & 0 & 0 & 0 & 0 \\ 0 & 0 & 0 & 0 & \alpha_{ex} & 0 & 0 & 0 & \alpha_{eg} & 0 & 0 & 0 & X_{12} & 0 & 0 & 0 \\ 0 & 0 & 0 & 0 & 0 & \alpha_{ex} & 0 & 0 & 0 & \alpha_{eg} & 0 & 0 & \alpha_{hx} & X_{13} & 0 & 0 \\ 0 & 0 & 0 & 0 & 0 & 0 & \alpha_{ex} & 0 & 0 & 0 & \alpha_{eg} & 0 & \alpha_{hg} & \beta_h & X_{14} & 0 \\ 0 & 0 & 0 & 0 & 0 & 0 & 0 & \alpha_{ex} & 0 & 0 & 0 & \alpha_{eg} & 0 & \alpha_{hg} & \alpha_{hx} & X_{15} \end{array} \right) \quad (2.4.19)$$

where we can define

$$X_n = - \sum_{m, m \neq n} \mathcal{L}_{mn} \quad (2.4.20)$$

It is now straightforward to find a stationary solution $\dot{\rho} = 0$ by finding the zero eigenvalue of the system and its associated eigenvector.

We can analyse this matrix numerically and find its corresponding eigenvalues and eigenvectors for any values of α , β and γ we wish. Using MatLab, we can then find the eigenvector which corresponds to the zero eigenvalue, representing the steady state solution. The zero eigenvector is real and unique. After normalisation this will provide us with the probability of occupation of each state.

Obviously as the rates vary considerably in the model, the steady state solution will also vary accordingly. Figure 2.4.2 shows the variation of occupation probability of the four energy levels with bias voltage, along with the probability of the dot being completely empty, between 1 and 1.5V. The model assumes the resonant condition. That is to say, the data shown is for a dot resonant at the exact voltage in question. If resonance was not assumed, the plot would be zero at every point other than the resonant voltage.

The groundstate occupancies are higher than the excited state occupancies, which can be attributed to the asymmetric carrier relaxation between them. The hole tunnelling rate is the limiting factor at low voltages, until it crosses the recombination rate at approximately 1.32V. Subsequently, we see the hole levels occupancies probabilities increasing from zero at 1V to 0.97 at 1.5V. The switch over of limiting factors from hole tunnelling rate to excitonic recombination rate has an interesting effect on the electron level occupancy probabilities, which remains high between 1 and 1.15V before dropping off only to peak again between 1.35 and 1.5V. This can be understood in the following manner: below 1.15V, the hole tunnelling rate is particularly low, leading to very small numbers of holes occupying the dot; this in turn means that virtually every electron which tunnels

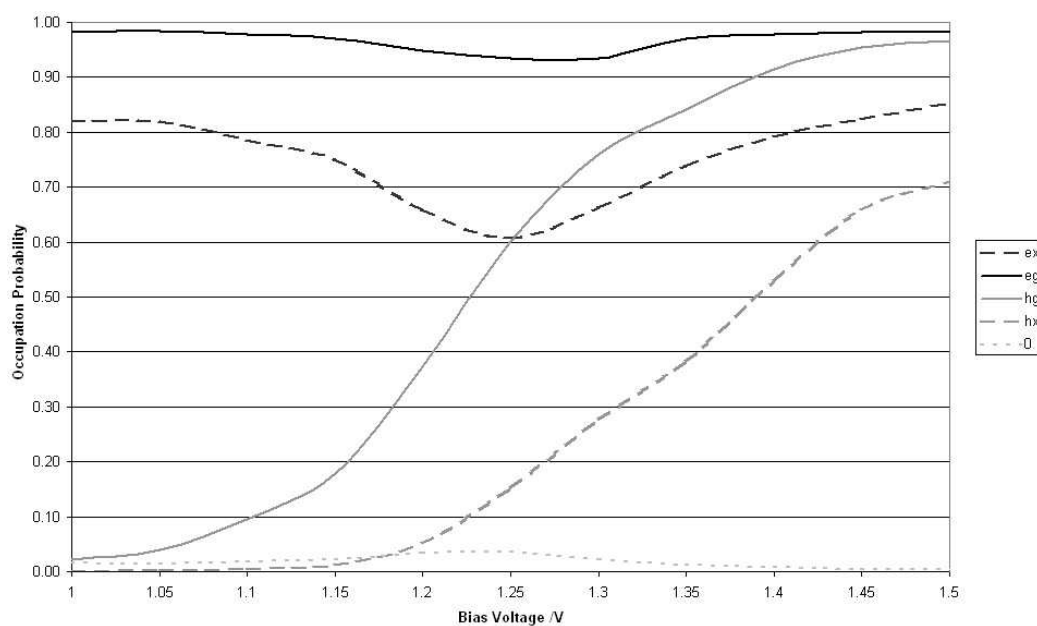


Figure 2.4.2: Variation of level occupation probability with bias voltage

onto the dot remains there, unable to recombine. Alternately, above 1.35V, the electron tunnelling rate approaches a factor of 10 higher than the recombinations rate, meaning that any electron which combines is immediately replaced. This can be seen as a switch from a “static” to a “dynamic” equilibrium. Between 1.15 and 1.35V, the three rates become comparable, and a lower equilibrium is maintained.

Chapter 3

Implementation

This chapter goes into more detail about the exact method of implementing the model numerically. The simulation is based on a stochastic model, not dissimilar to the Monte Carlo method. First we generate an array of 2500 dots within a p-i-n junction and calculate all their relevant properties. We are then able to calculate the necessary rates of carriers moving into, within, and out of the dots. A stochastic simulation is then used to find the populations of the dots, and this data is then fed back into the system to update the relevant rates.

3.1 Calculating The Energy Levels

The energy levels of each dot are calculated using a series of random numbers. The dots are generated with an adjustable predefined mean and standard deviation in both dot size and dot separation, which can be adjusted to co-ordinate with the experimental data attributed to the sample we wish to model.

The random numbers are generated using the “ran2” algorithm taken from

[31], with computer clock time used as a seed. `ran2` has a period of 10^{18} , which is more than sufficient for this simulation, which uses in the region of 2×10^{11} random numbers per run. It generates numbers linearly distributed between 0 and 1, which can then be adjusted to fit a Gaussian distribution where necessary.

The simulation generates five electron energy levels and five hole energy levels for each dot. The levels represented are the dot groundstate, with spatial quantum numbers (1,1,1), two excited states (2,1,1) and (1,2,1), a semi-localised energy level representing the wetting layer, and a bulk GaAs state in which the carriers are free to move around within the array. The exact energy levels of the groundstate, excited states are calculated according to the model used in section 2.1, using the randomly generated dot dimensions. As a semi-localised state, the energy of wetting layer is also dependent upon the size generated for the dot, albeit with a smaller mean distribution centred on 1.43eV. It is assumed that the GaAs conduction and valence band edges will not be perfectly uniform; the presence of impurities in the system will most likely lead to small fluctuations. The energy of the GaAs conduction and valence band states is centered at 1.52eV, with fluctuations with a standard deviation of only 1meV, which are distributed independently of the dot size. Figure 3.1.2 shows the ten energy levels generated for each dot.

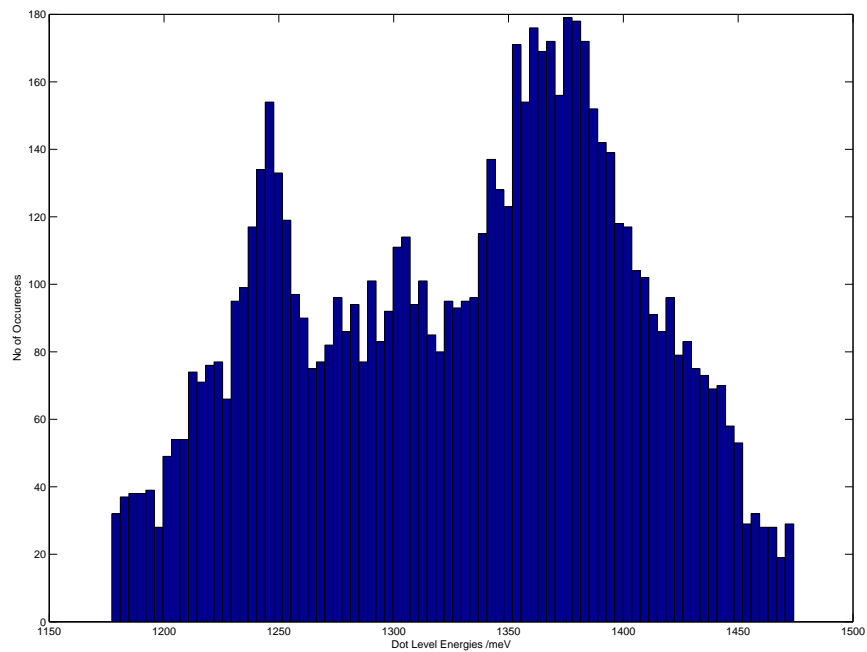


Figure 3.1.1: Distribution of electron dot energy levels generated by the simulation. The values on the x axis denote the bias voltage at which the state will become resonant during the simulation

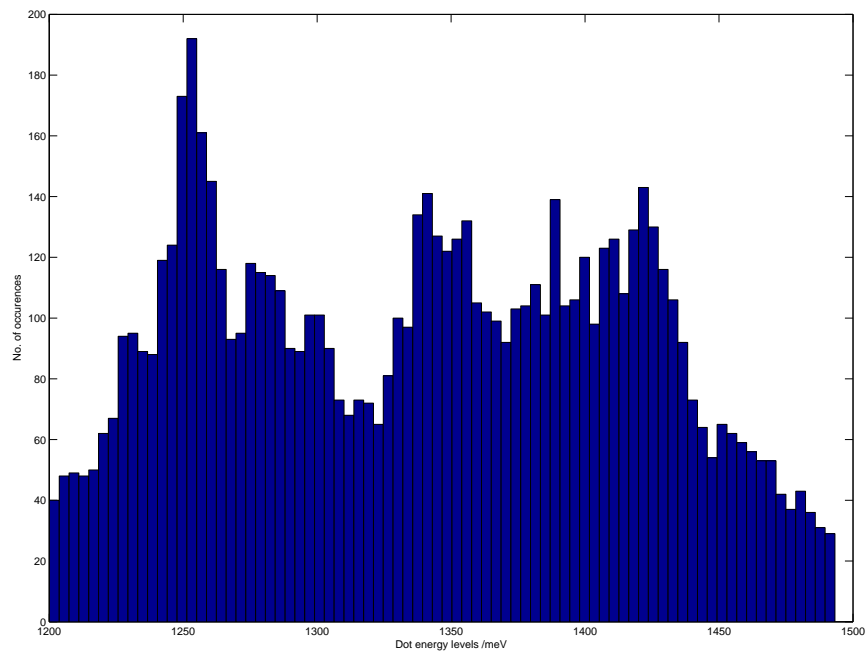


Figure 3.1.2: Distribution of hole dot energy levels generated by the simulation. The values on the x axis denote the bias voltage at which the state will become resonant during the simulation

3.2 Calculating the Rates

Having generated our energy level array, we can now adjust the bias voltage in the simulation and fill the dots with carriers. In order to calculate the occupations of each dot, we must first calculate the theoretical tunnelling rate, α . This is defined as:

$$\alpha_{ij} = T_i R_{ij} (1 - o_{ij}/2), \quad (3.2.1)$$

where T is the background tunnelling rate, R is the resonance function, o is the occupation, and i and j are the dot and level index respectively. The electron and hole tunnelling rates are calculated separately but using an identical method. The occupation will be initially generated using the theoretical tunnelling rate and fed back into the equation. The $(1 - o_{ij}/2)$ term is a result of Pauli's Exclusion principle. Each energy level can be occupied by two carriers simultaneously, providing they have different spins. The formula can be justified in the following way: if the level is unoccupied, all carriers in the contact are eligible to tunnel; if the level is completely occupied, then no carriers are eligible; and if the level is occupied by one carrier, then on average half of the carriers will possess the opposite spin and will thus be eligible. For computational purposes, the carriers are not individually assigned spins, so this term is necessary to create the same effect.

The rates T_i and R_{ij} , need to be calculated separately.

The background tunnelling rate, T_i , is calculated using the WKB approximation as described in section 2.2. T_i is the maximum tunnelling rate into a single dot energy level on exact resonance. We previously defined T_i as:

$$T_{in(p)} = f_{n(p)} e^{-2k_i x_i}, \quad (3.2.2)$$

where $f_{n(p)}$ is the n(p) contact attempt frequency calculated in section 2.1, k_i is the wavevector associated with the tunnelling region between the contact and the dot, and x_i is the separation between the contact and the dot.

We are able to calculate k_i and x_i using the initial parameters of the system, which we may wish to vary in order to replicate experimental method, and a simple triangular barrier method, which introduces a bias voltage dependence in $T_{in(p)}$. This was demonstrated in section 2.2.

Using this method, the simulation therefore produces a logarithmic plot of $T_i(V)$ in figure 3.2.1.

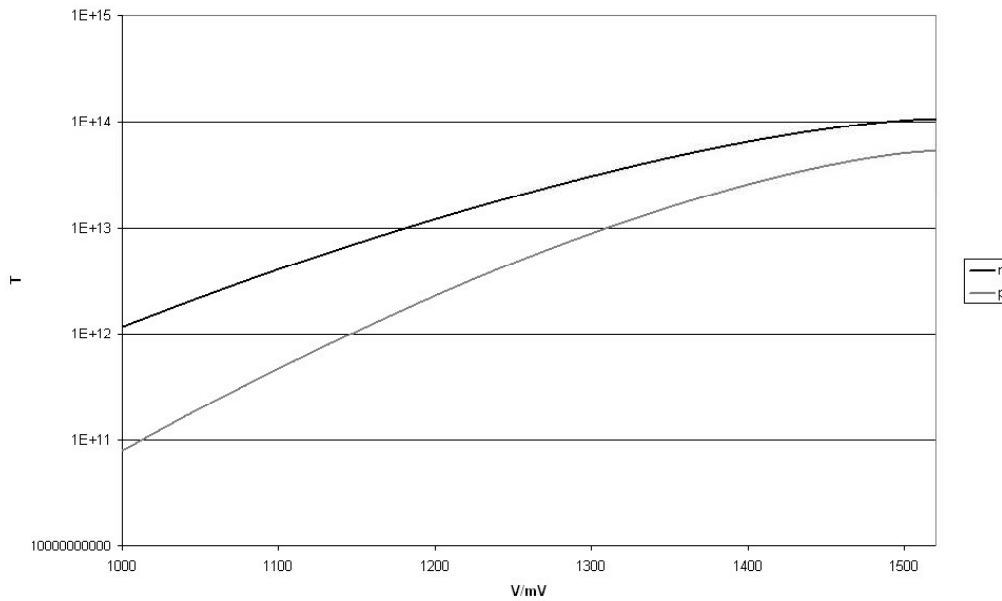


Figure 3.2.1: Background tunnelling rate $T_{in(p)}$

The figure shows $T_{in(p)}(V)$ levelling off as it approaches flat band (1.52V).

This is due to the fact that an increase in voltage at this point leads to a comparatively smaller decrease in k_i than at lower voltages. At this point, the background tunnelling rate is identical for all 2500 dots.

We now need to calculate the resonance function R_{ij} , for each level j , of each dot i . This is calculated from the energy overlap between the the dot level and the energy distribution of the carriers in the contacts. The density of states within the dot is modelled as a delta function, and the energy density of the carriers in the contact can be calculated by multiplying the 3D density of states within a GaAs conduction (valence) band by the Fermi distribution of electrons (holes) within the available states.

The density of states in the conduction band is given by:

$$D(E) = \frac{8\sqrt{2}\pi m^{*3/2}}{h^3} \sqrt{E - E_F}. \quad (3.2.3)$$

The Fermi distribution of particles within these states is given by:

$$F(E) = \frac{1}{(e^{(E-E_F)/k_B T} + 1)}. \quad (3.2.4)$$

Therefore the resonance function behaves according to:

$$R_{ij} = A_{ij} D(E) F(E) \delta(E - E_{ij}). \quad (3.2.5)$$

We know that when the energy levels of the two are perfectly aligned, R_{ij} is equal to one, and we normalise the integral with the factor A_{ij} to ensure that this is the case. Figure 3.2.2 shows the resonance function against bias voltage of a randomly selected dot.

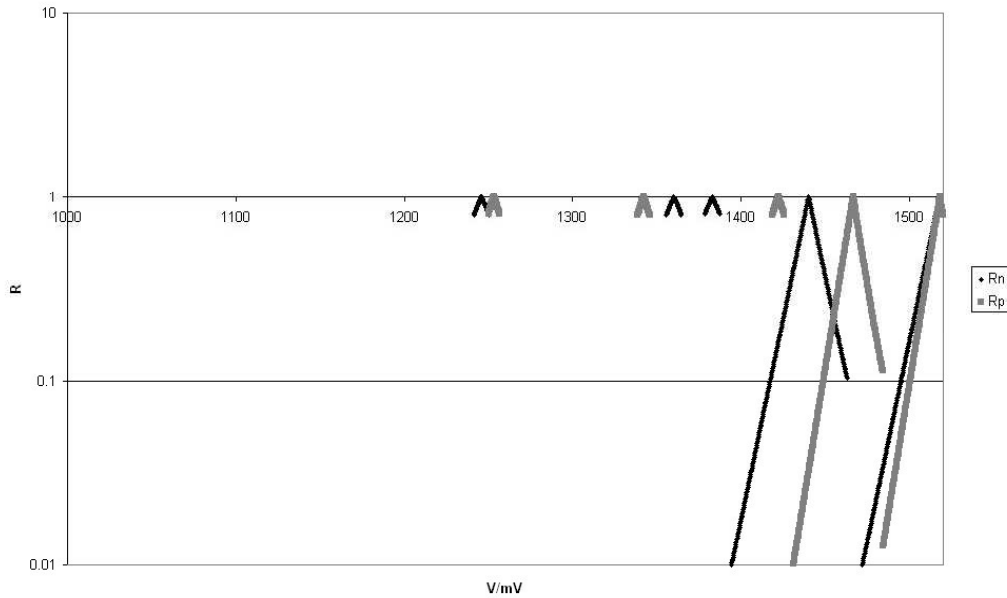


Figure 3.2.2: Resonance Function for a randomly chosen dot

The groundstate, excited state, wetting layer and conduction/valence bands are all visible. One thing of particular interest is the appearance that the hole resonance function appears squashed up towards flat band conditions compared to the electron resonance function, and the wetting layer and conduction/valence band resonances are no longer aligned. This is due to the asymmetric positioning of the dot layer within the intrinsic region.

This is also clear in figure 3.2.3, which shows the sum of the resonance functions for all 2500 dots.

We now need to calculate the rates of the other two processes in the system, the radiative recombination and non-radiative relaxation rates.

The non-radiative process allows carriers to relax from the conduction band and wetting layer into energy levels within the dots, and also from excited states to ground states within the same dot. This process was described in section 2.3,

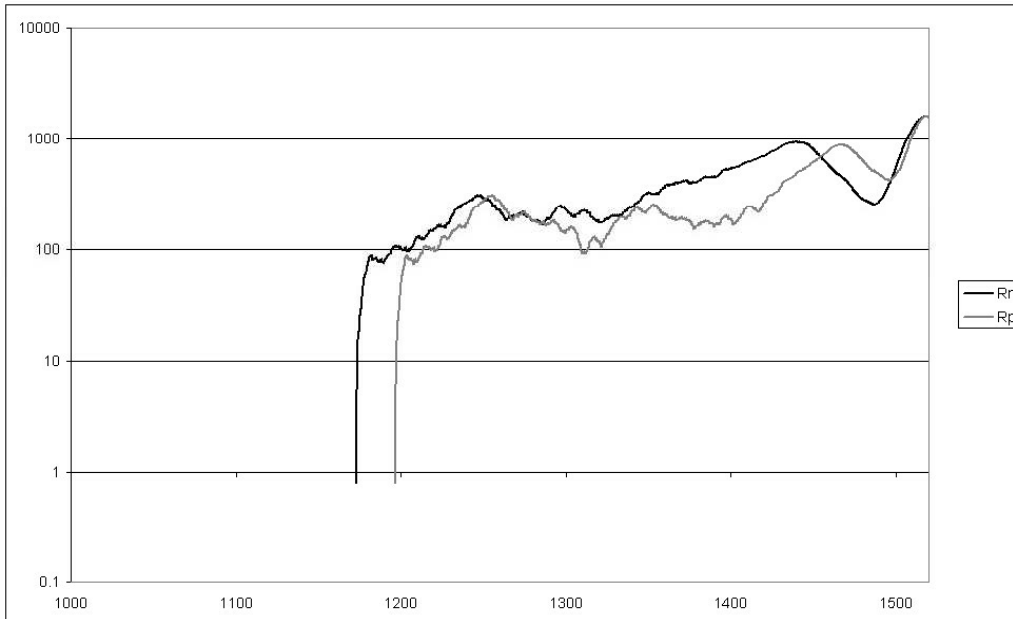


Figure 3.2.3: total resonance for all 2500 dots

and is the highest transition rate in the simulation, with a mean transition rate of $1 \times 10^{15} \text{ s}^{-1}$. In previous experimental data, the relaxation can be seen to occur for all relative energy differences. Therefore we make the assumption that all states are able to relax provided there is an empty state available, without taking into account their relative energy differences.

As with the tunnelling rate, this process must also take into account Paulis exclusion principle, because if the level to which the carrier is attempting to relax is already occupied, the process will be dependent upon the spin of the carrier. If the process involves a carrier in dot i relaxing from state j to state k , we proceed by multiplying the initial rate by a factor of $o_{ij}(1 - o_{ik}/2)$.

The excitonic recombination rate was shown in chapter 2 to be proportional to the overlap integral between the relevant occupied electron and hole states, and thus this rate is calculated in the computational model for each energy level of

each dot.

Neither of these rates have a bias voltage dependence, and therefore they need only be calculated once at the start of the simulation. Figure 3.2.4 shows typical recombination and relaxation rates superimposed onto the products of T and R for all 2500 dots. This allows us to be able to compare the relative orders of magnitude of the various processes.

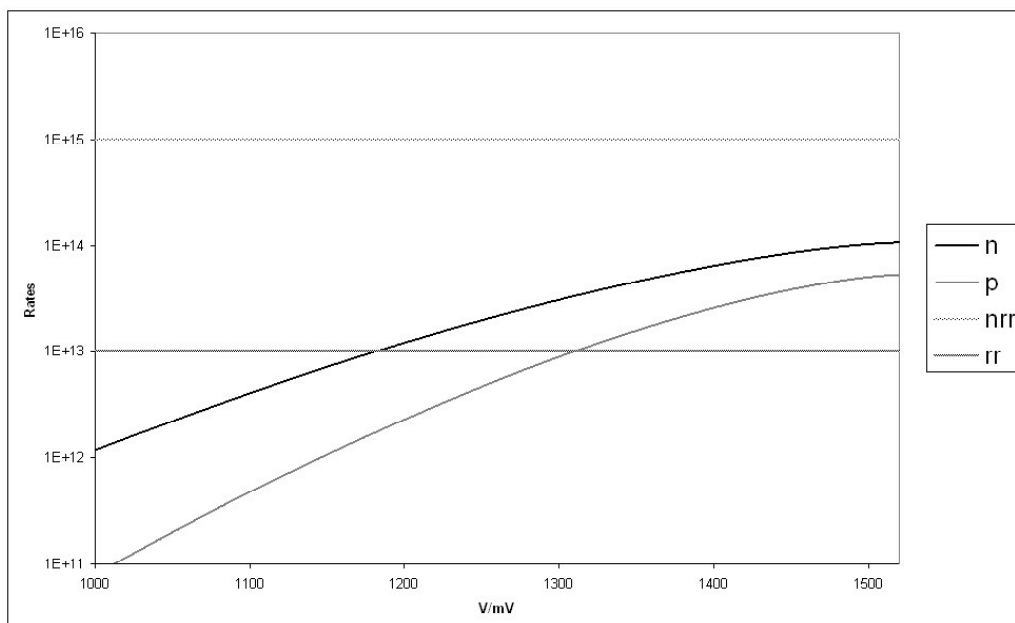


Figure 3.2.4: Comparison of rates of all major processes

Here we can see that at low bias voltages, the tunnelling rates are the limiting factor, but above approximately 1.3V, the excitonic recombination rate becomes the limiting rate.

3.3 Calculating the Populations

Now that we have calculated or estimated every relevant rate within the system, we are in a position to run a stochastic simulation over a large number of timesteps and over a range of bias voltages, and allow the dots to be continually filled and emptied of carriers. For the simulation to be valid, it is important that the calculated theoretical rates are recoverable from the rates generated by the stochastic process. In order to fill and empty the dots stochastically, we generate a large number of random numbers, the details of which were discussed in section 3.1.

We use the random numbers generated to fill and empty the dots at each timestep. We do this by comparing a random number x to the product of the relevant rate and the timestep, which we denote as X .

If $x < X$, the process will take place. If $x > X$, the process does not take place.

For each of the 5 electron energy levels and 5 hole energy levels, for each of the 2500 dots, this process is repeated to simulate the tunnelling rate into the dots. Any carriers occupying excited states are then given the chance to relax into states of lower energy (this is consistently the fastest process in the model), the carriers are then given the chance to recombine in accordance with the radiative recombination rate. For each timestep, a total of 87,500 random numbers are used to empty and fill the levels of the 2500 dots.

The full simulation involves increasing the bias voltage from 1V to 1.52V (flat band) in increments of 0.25mV. For each increment, the system runs through 1000 timesteps. Thus the model simulates a total of 1.82×10^{11} separate processes.

The timestep is kept constant throughout the simulation at a value of 5×10^{-14} .

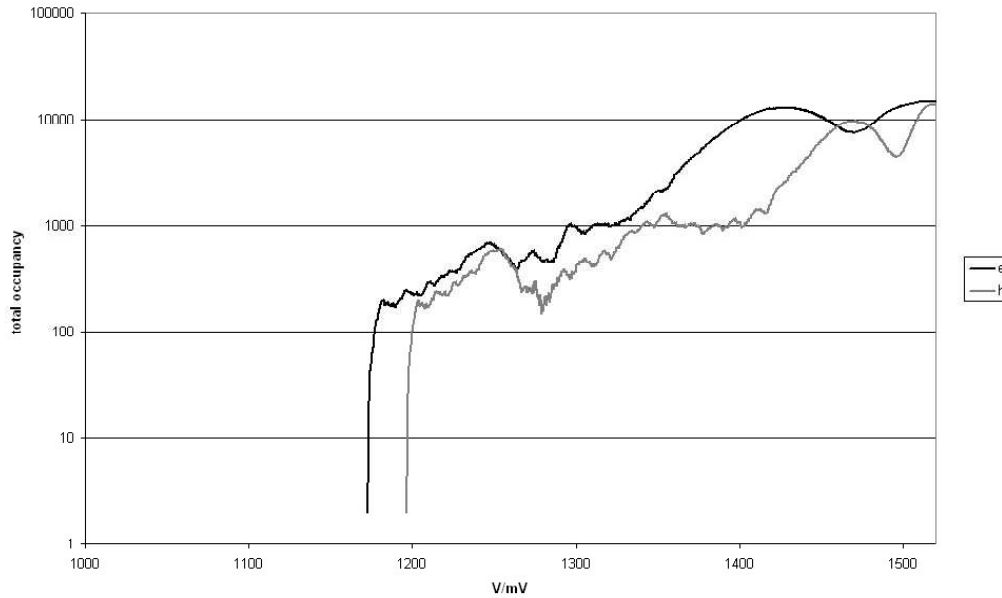


Figure 3.3.1: Numbers of electrons and holes occupying the dot array at each voltage

Therefore we expect to see 500 recombination events for every 1000 opportunities, and the limiting rate never has a probability of completion of greater than 50% at any voltage. At the lower voltages where the groundstate levels first become resonant, the hole tunnelling rate is the limiting factor. The probability of a hole tunnelling event at around 1.2V is approximately 10%, which is high enough for a current to be visible over 1000 timesteps. Therefore the stochastic transport results should be representative of the theoretical rates seen in figure 3.2.1. Figure 3.3.1 shows the number of electrons and holes occupying the dot array at each voltage.

We can see from figure 3.2.4 that above approximately 1.3V, the excitonic recombination process becomes the limiting rate. Therefore, above this voltage, the carriers enter the dots at a greater rate than they are able to recombine, and a

surplus of carriers will build up between 1.3V and flat band, as seen in figure 3.3.1. As would be expected, the build-up of the carriers can be seen to approximately follow the contours of the relevant resonance functions.

We are now in a position to extract from the simulation a prediction of the transport characteristics of the system. By combining the resultant electron and hole tunnelling rates over 1000 timesteps, we can calculate a current against voltage plot, shown in figure 3.3.2.

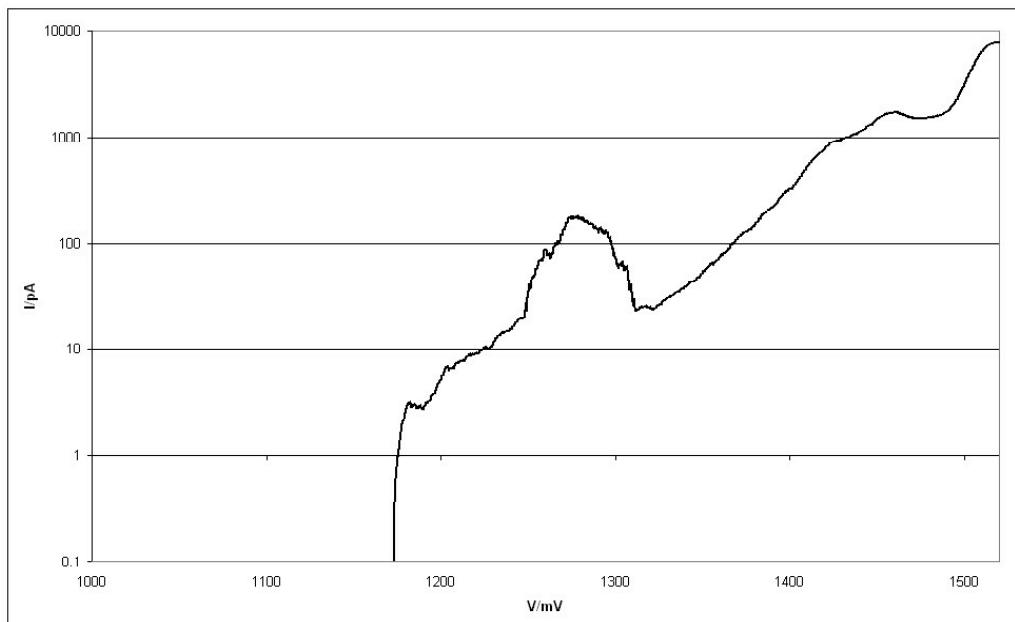


Figure 3.3.2: Current vs voltage plot for transport through the dot array

We can see a general exponential increase in current, as to be expected for a p-i-n junction. The peak at 1.43eV is visible, caused by carriers tunnelling directly into the wetting layer states. Most obviously though, we can see a large increase in tunnelling between 1.25 and 1.3eV, caused by direct tunnelling into the dot ground and excited states.

If we measure the energy levels every time a recombination event occurs, we

can calculate the energy of the corresponding photon. This then allows us to construct a photon energy spectrum for each voltage. Figure 3.3.3 shows the number of photons produced at each voltage, figure 3.3.4 shows the photon energy spectra for a range of bias voltages, and in figure 3.3.5, the two values are combined into a colour-scale plot.

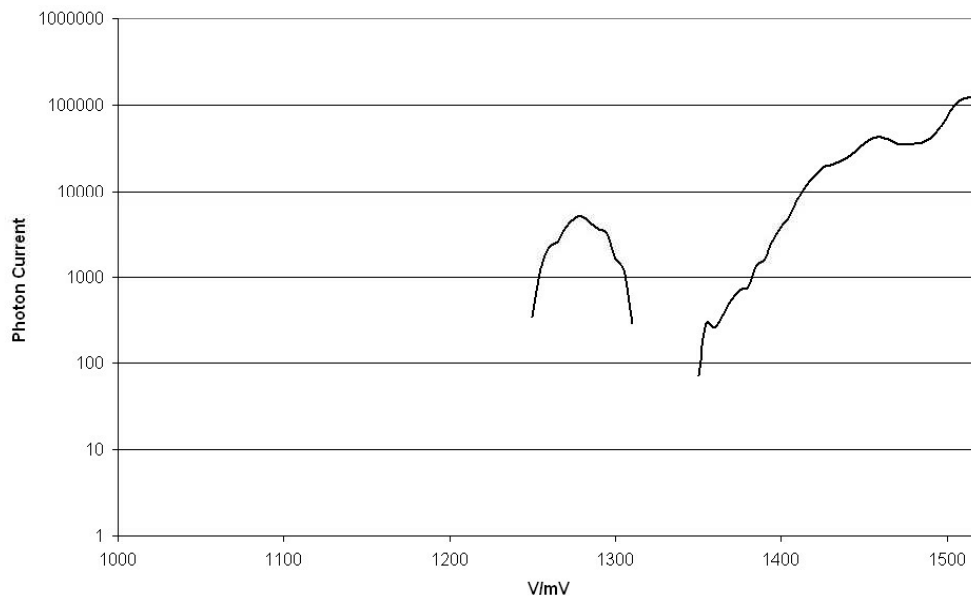


Figure 3.3.3: The number of photons emitted per 1000 timesteps for each voltage

The number of photons emitted at each voltage, as shown in figure 3.3.3, is closely related to the IV characteristics seen in figure 3.3.2. Comparing the two plots, we can see that between 1.08 and 1.25eV and between 1.3 and 1.35eV, the carriers are able to tunnel into the dot states, but recombination does not occur. The tunnelling current between these voltages is therefore limited by Pauli's exclusion principle. The jump in current between 1.25 and 1.3eV is therefore caused by the electrons and holes being able to tunnel simultaneously into the same dots and immediately recombine. As the dots are continuously emptying, Pauli's exclu-

sion is no longer the limiting factor, and hence the remarkable jump in current.

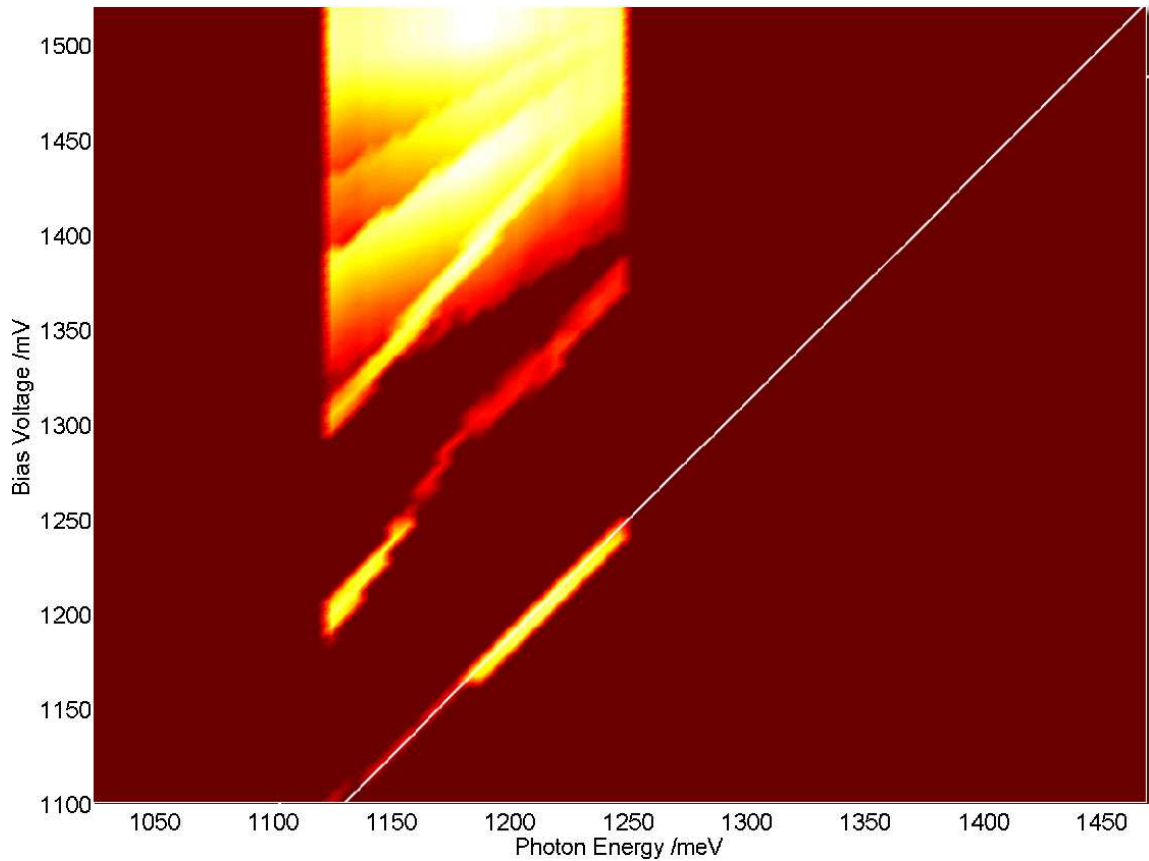


Figure 3.3.4: EL colour-scale plot of photon energy against bias voltage

Figure 3.3.5 shows a colourscale plot of the electroluminescence characteristics of the system between bias voltages of 1.2 and 1.52V. A number of features can readily be identified. The photons emitted vary in energy between approximately 1.2 and 1.3eV, showing that they have all been emitted via groundstate to groundstate recombination. We can see two discrete diagonal lines at lower bias voltages before an block of emission begins at around 1.35V. The lowest emission line follows the $eV = hf$ condition. This therefore corresponds to carrier tunnelling directly into the dot groundstates before recombination. We see a second

line offset from the first by a gap of between 70 and 100meV, which indicates that carriers are tunnelling into excited states and relaxing into the groundstate before recombining. At higher bias voltages the wetting layer and further excited states come in to play, leading to several lines on top of each other. At 1.51-1.52V we see the carriers begin to move around the conduction and valence bands before dropping down into dot groundstates and emitting from all the dots simultaneously.

One particularly interesting region is the jump in intensity between 1.25 and 1.3V. This corresponds to the previously mentioned peak in the IV curve. This can be understood by considering the effect of the asymmetric array location within the intrinsic region on the resonance functions of each dot. As the electron ground-state energies are distributed around 1.28eV and the hole energy levels at around 1.22eV, it should be impossible for both levels to be resonant with both species simultaneously. However the asymmetry means that the hole resonance function is “squashed up”, as shown in figure 3.2.2. This means that for the bias voltage region in question, a range of smaller dots are simultaneously resonant with both species, allowing immediate recombination, and a hugely increased current and photocurrent.

Now that we have extracted the necessary data from the simulation, it is appropriate to compare our simulated plots with the experimental data seen in Section 1.3. We can see that some similarities are visible between the experimental and computational El plots. A clear “S” shape curve is visible in both plots, but the emission lines in the computational plots, although in approximately the correct location, are noticeably thinner than the experimental plot. We will now attempt to improve our model by adding in the effects of the Coulomb interaction between

the charged carriers occupying the dots.

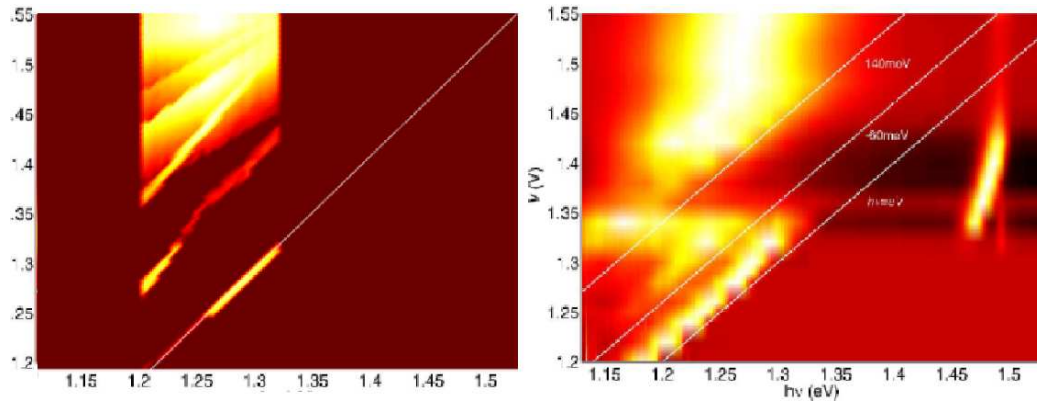


Figure 3.3.5: Comparison of experimental and theoretical EL colour-scale plots

Chapter 4

Including the Coulomb interaction

We have seen that the computational model produces predictions for transport and electroluminescence which bear some similarities to experimental data. However, when dealing with the resonant tunnelling of charged carriers into a small island, the effect of the interactions between them will have a noticeable effect on the dynamics of the system. We now aim to improve our model by including the effects of the Coulomb interaction in the simulation, which have previously been neglected. The effects of Coulomb interactions on the dot wavefunctions and transport has been studied several times before in other contexts, for example in [32, 33], and also in [34, 35]. The effects of Coulomb charging effects on transport through quantum dots remains an area of productive research; see for example work done by Kiesslich [36, 37, 38].

4.1 Mathematical Model

The Coulomb energy of a screened point charge is given by [5]:

$$E_C = \frac{1}{4\pi\epsilon} \frac{q}{r} e^{-k_0 r}, \quad (4.1.1)$$

where

$$k_0 = \sqrt{\frac{m^* e^2 k_F}{\epsilon \pi \hbar^2}}, \quad (4.1.2)$$

and

$$k_F = (2\pi^2 n)^{1/3}. \quad (4.1.3)$$

The force between two such point charges is therefore:

$$\mathbf{F}_C = \frac{1}{4\pi\epsilon} \frac{q^2}{r^2} e^{-k_0 r} \hat{\mathbf{r}}. \quad (4.1.4)$$

If two electrons are confined within a structure such as a quantum dot, they will repel each other according to Coulomb's law, but providing the confining potential is sufficient, both remain trapped within the structure. In order to calculate the extra separation between two electrons in our quantum harmonic oscillator model when accounting for the Coulomb interaction, we can simply compare the confining force pushing the particles together with the Coulomb force pushing them apart.

$$\frac{1}{4\pi\epsilon} \frac{e^2}{x^2} e^{-k_0 x} - m\omega^2 x = 0 \quad (4.1.5)$$

Solving this numerically, we are able to find an average separation between carriers in the same dot of 5.54nm, as shown in figure 4.1.1. Putting this value back into [4.1.1], we are able to find a value for the Coulomb energy between two electrons in a quantum dot of 12.8meV. As this is also the change in energy if a

valence electron leaves the dot, it is valid to assume that the Coulomb energy between an electron and a hole occupying the same dot is -12.8meV . We also need to examine the case in which a carrier is occupying the semi-localised wetting layer state. Using the same method, we find that the average separation between carriers in the wetting layer state is 12.5nm , giving an associated Coulomb energy of 2.5meV .

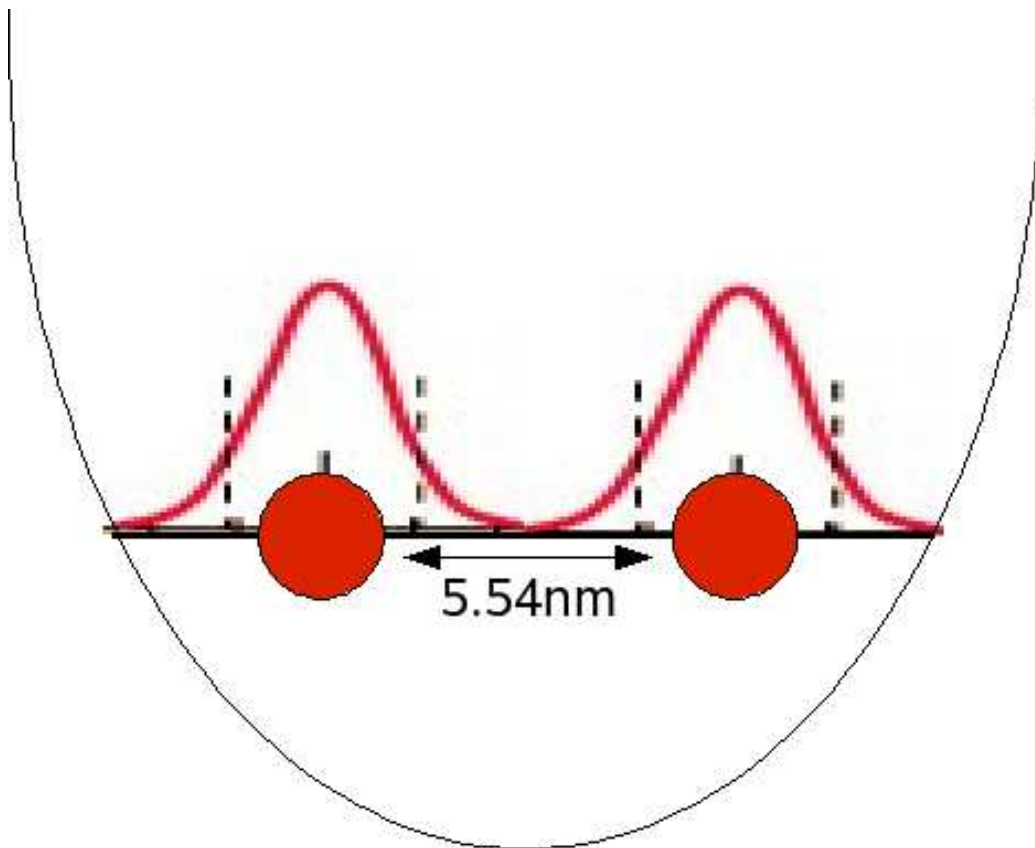


Figure 4.1.1: Average separation between two electrons in a QHO

This is the extra energy that an electron must possess to resonantly tunnel into a dot already occupied by a second electron. The inverse case is also true, in that a hole will be able to tunnel into a dot occupied by an electron with an energy

12.8meV below resonance. The overall effect is equivalent to the dot energy levels “shifting” by 12.8meV in opposite directions for each carriers species. If the dot is occupied by a hole, the electron tunnelling resonant energy drops by 12.8meV, and the hole tunnelling resonant energy rises by the same amount. This effect is shown in figure 4.1.2.

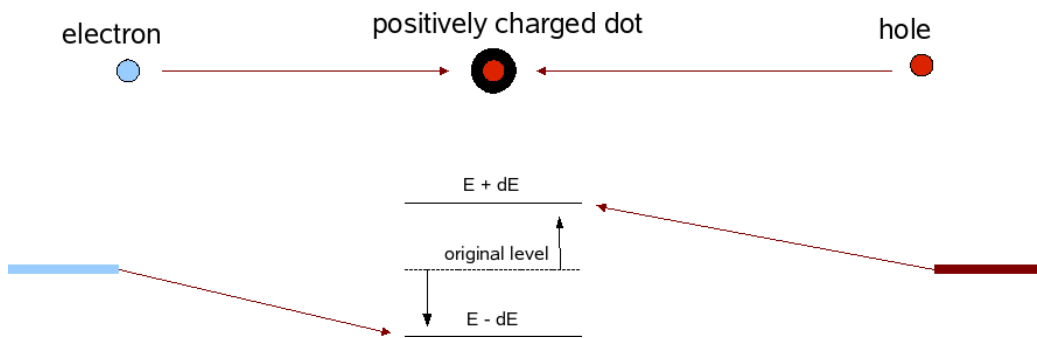


Figure 4.1.2: The energy levels shift in the opposite direction for each carrier species

This Coulomb energy therefore affects the bandstructure around the quantum dot array in a quantitative manner. The distortion around a particular dot will be affected by the net charge on that dot, and also, to a lesser degree, on the respective charges around its neighbouring dots.

The mean separation between two nearest neighbouring dots is dependant upon the dot density within the array. For a typical dot density of between 10^{10} and $10^{11}m^{-1}$, the average separation between the dots is 30-100nm, as shown in figure 4.1.4, giving a Coulomb interaction energy of between 0.05 and 0.5meV. This is a small energy in comparison with 12.8meV, but if several neighbouring dots possess the same net charge, it is enough to significantly affect resonant tunnelling probabilities. We do not take into account neighbouring dots further away than 100nm.

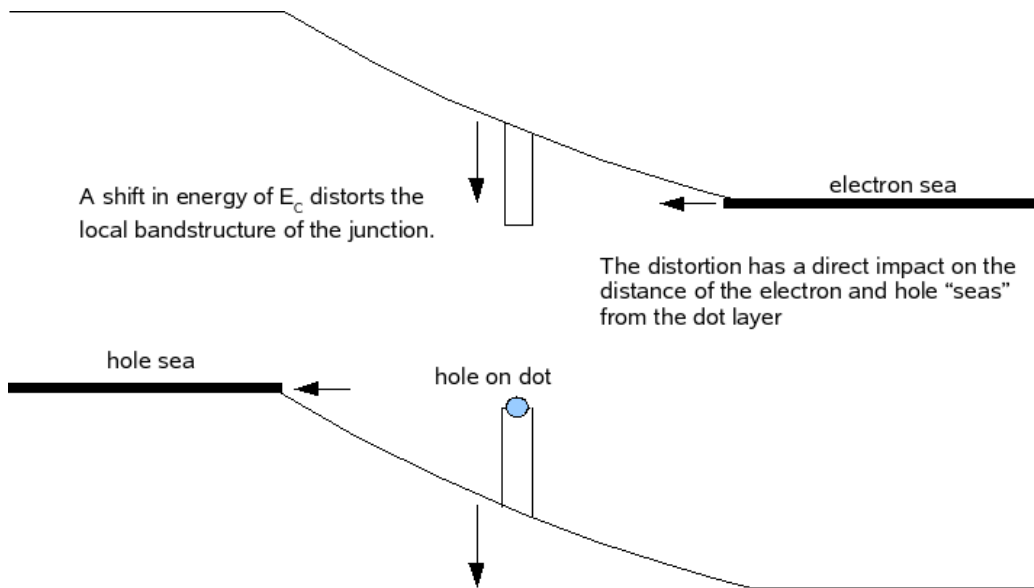


Figure 4.1.3: Bandstructure distortion caused by the presence of a charged carrier on the dot

As the bias voltage is increased in the simulation, the electron and hole "Fermi seas" in the contacts creep closer towards the dot array. As they get closer, they also feel the Coulomb force due to dot occupations. This results in a non-uniform distance between the contacts and the dot array as the free carriers are pushed away from and pulled towards the charged dots. For example, if an area of neighbouring dots all possessed a positive charge, a "finger" would extend out of the electron sea towards it. The reduced tunnelling distance would enable electrons to tunnel at a greater rate, cancelling the net positive charge, and provide a negative feedback loop within the dot system. This concept is shown in figure 4.1.5.

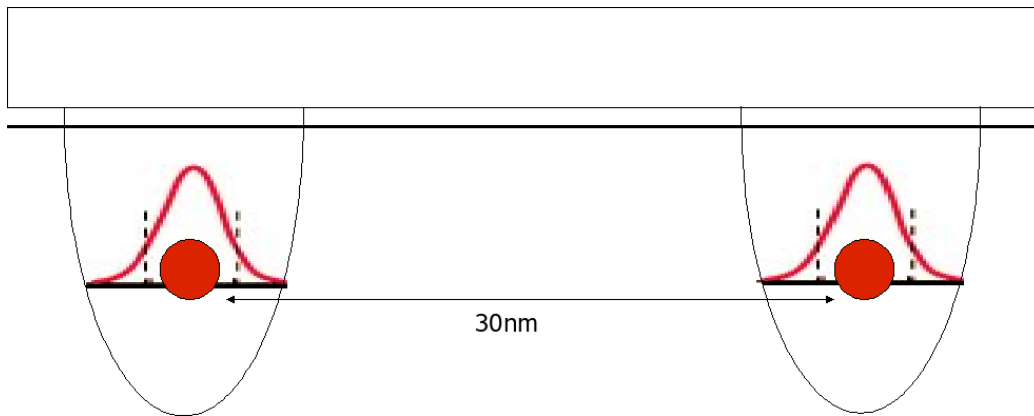


Figure 4.1.4: Typical separation between neighbouring dots



Figure 4.1.5: "Fingers" extending from contacts towards dots caused by distortion of the electric field due to the presence of carriers on the dots

4.2 Implementation and Results

Once the dot occupations are known, the Coulomb energies are calculated, and the energy levels and resonance functions are adjusted accordingly. All ten energy levels within the dot must be adjusted, as all are affected by the presence of a carrier species. The contact sea distortion is also calculated, and the tunnelling rate is adjusted.

The Coulomb energy affecting each dot is calculated not only from the net charge on the dot in question, but also the net charge of its nearest eight neighbours. The energy levels of the dots fluctuate as carriers tunnel onto them and their neighbouring dots and subsequently recombine. The effect this has on the resonance function can be seen in figure 4.2.1.

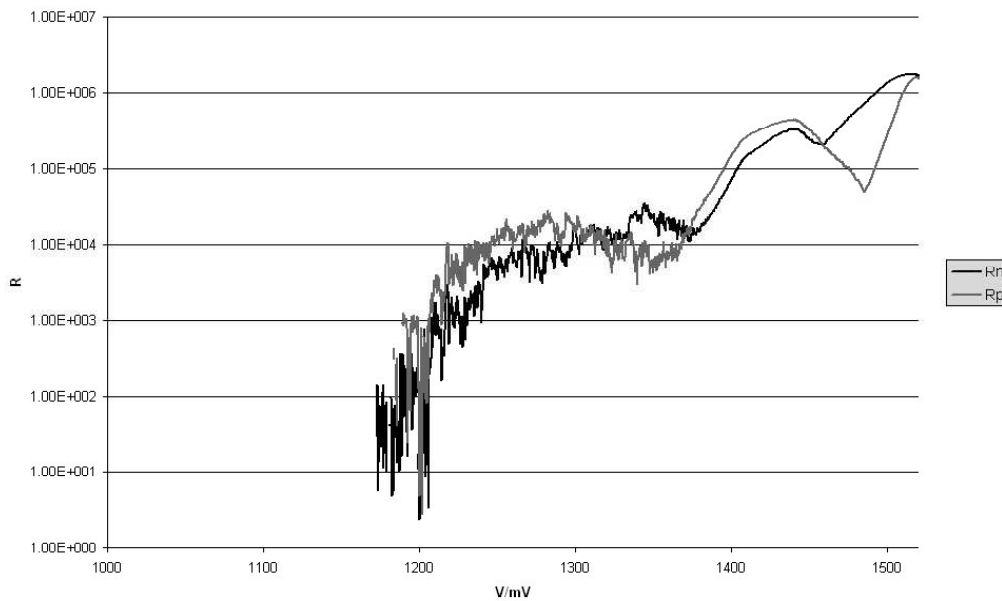


Figure 4.2.1: Resonance Function for all dots with Coulomb interaction included in the simulation

The contact-to-dot distance also fluctuates as the Coulomb energy around the

dots change. This leads to a change in the distance the carriers must tunnel to get onto the dot. In effect this is a simple negative feedback mechanism: a dot occupied by a hole will pull the electron sea closer, whilst pushing the hole sea further away, encouraging carriers of the opposite species to tunnel preferentially. The fluctuations in the tunnelling distances can be seen in figure 4.2.2, and the effect on the tunnelling currents can be seen in figure 4.2.3.

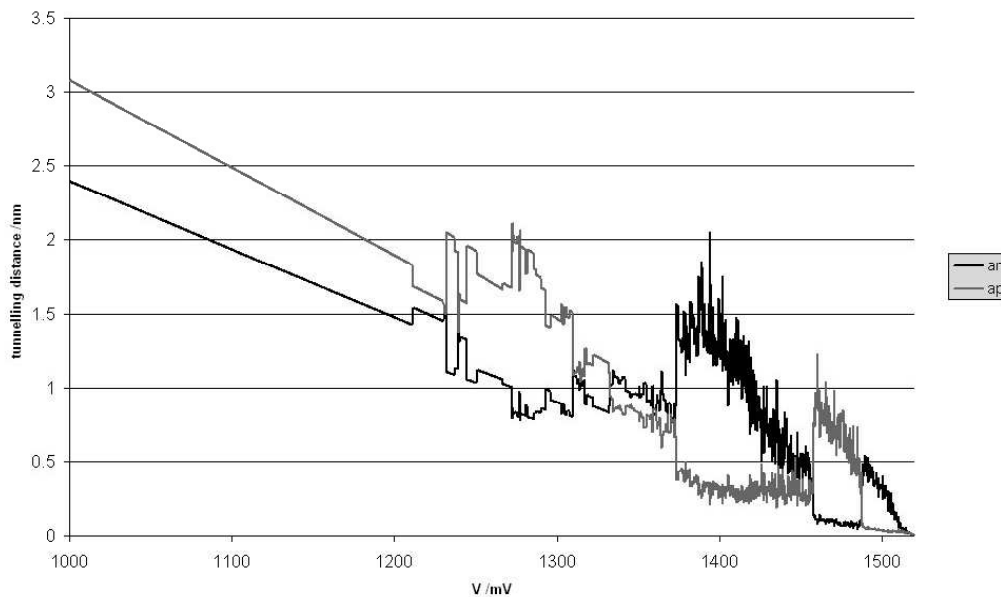


Figure 4.2.2: Fluctuations in tunnelling distance

We can now see what effect the inclusion of the Coulomb interaction has upon the transport and electroluminescence properties of the system. Figure 4.2.4 shows the modified IV plot for the system. We compare this with figure 3.3.2, the IV plot without the Coulomb interactions included, and we see that the effect of the interaction has been to “smooth out” the large jump in current between 1.25 and 1.3V over a wider range of voltages.

Figure 4.2.5 shows the photon current plot, which follows the same pattern as

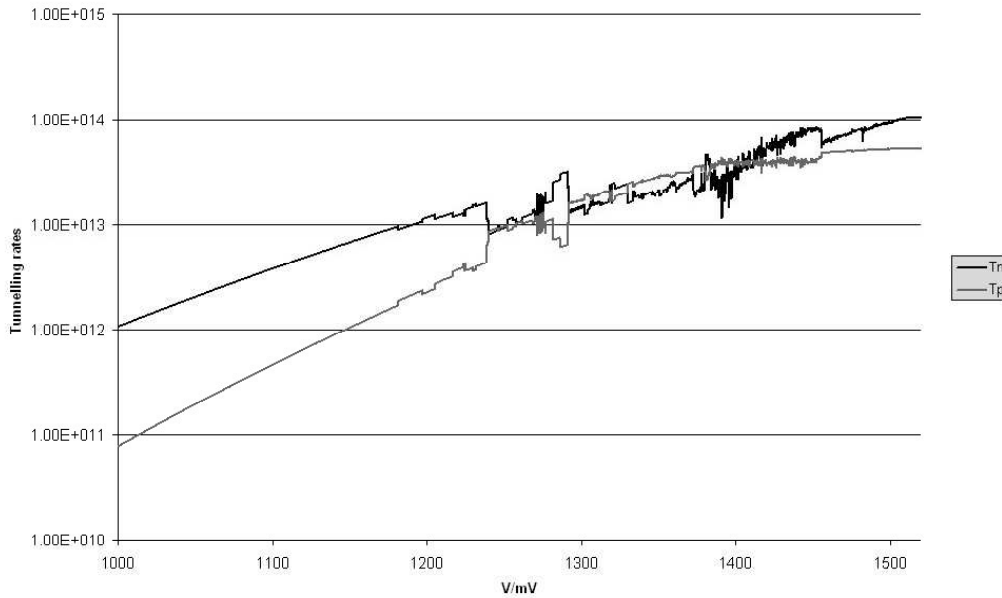


Figure 4.2.3: Fluctuations in the background tunnelling rate caused by the fluctuations in tunnelling distance

the transport current, with the large jump seen in the non-Coulomb case (figure 3.3.3), disappearing, to be replaced by an array of smaller peaks, as dots move in and out of resonance as their energy levels fluctuate.

The electroluminescence characteristics can be seen in figure 4.2.7, and are then compared with experimental results, seen in figure 4.2.8. The effect of the inclusion of the Coulomb interaction is clear for bias voltages below 1.35V; the two distinct lines we saw in figure 3.3.5 have been replaced by a continuum of luminescence, with four diagonal lines visible underneath. The lowest line is emitting at a lower voltage than that seen in the non-Coulomb case. This is caused by the negatively charged dots pulling the hole energy levels down into resonance at a lower bias voltage than the one at which they would normally be resonant. The other three lines at higher bias voltages are caused by similar effects between the

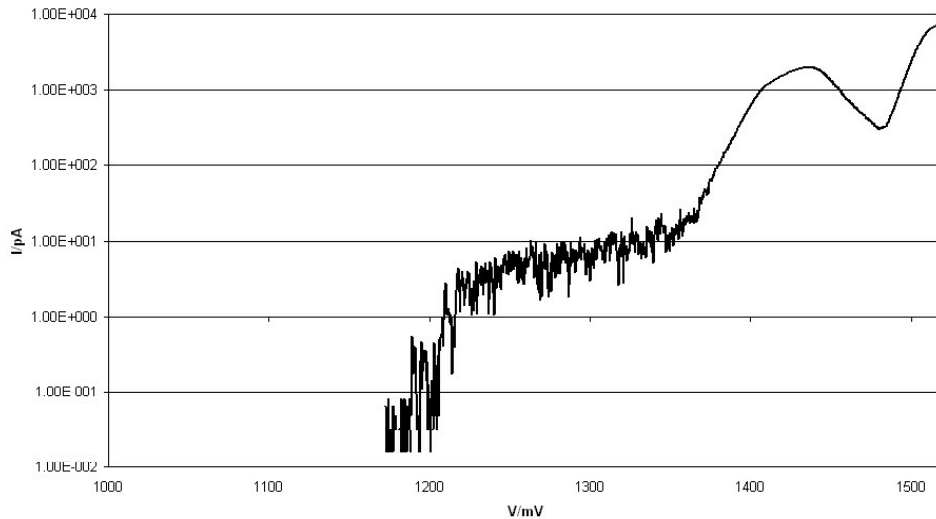


Figure 4.2.4: IV plot with Coulomb Interaction

groundstates and excited states. Again, the large increase at higher bias voltage is caused by relaxation into the dots from the wetting layer and conduction/valence bands. The colourscale plot is clearly in much better agreement with the experimental data now that the Coulomb interaction has been included, suggesting that Coulomb effects are an important consideration in modelling dot electroluminescence. The near-vertical emission line on the right of the picture, at a photon energy of approximately 1.5eV is caused by upconversion luminescence, which will be dealt with in greater detail in chapter 5. Focussing on the rest on the plot, we see that the remainder of the experimental colourscale plot is extremely similar to the simulated version, and a noticeable improvement from figure 3.3.5.

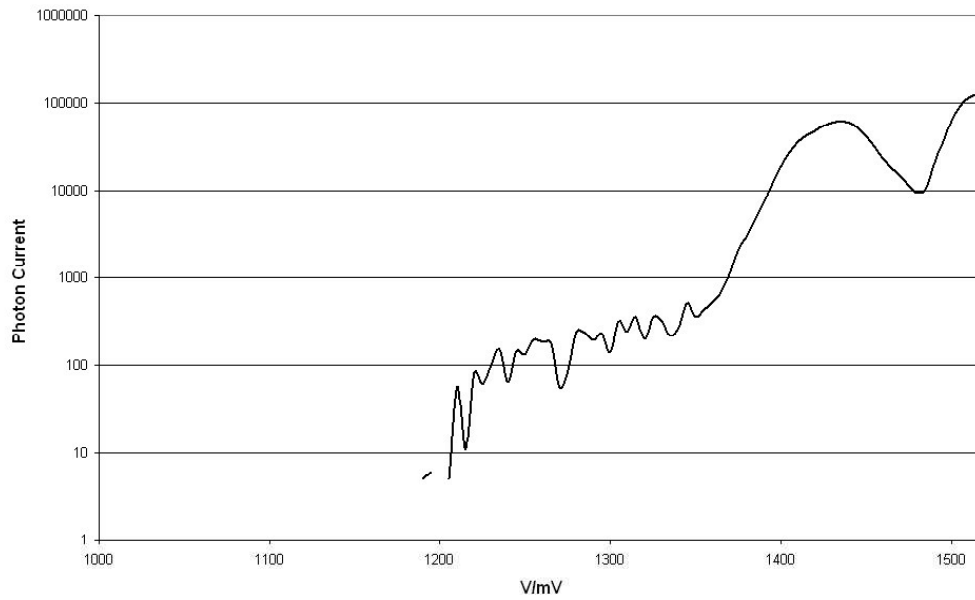


Figure 4.2.5: Photon Emission plot with Coulomb Interaction - the graph shows the number of photons emitted every 1000 timesteps for each voltage

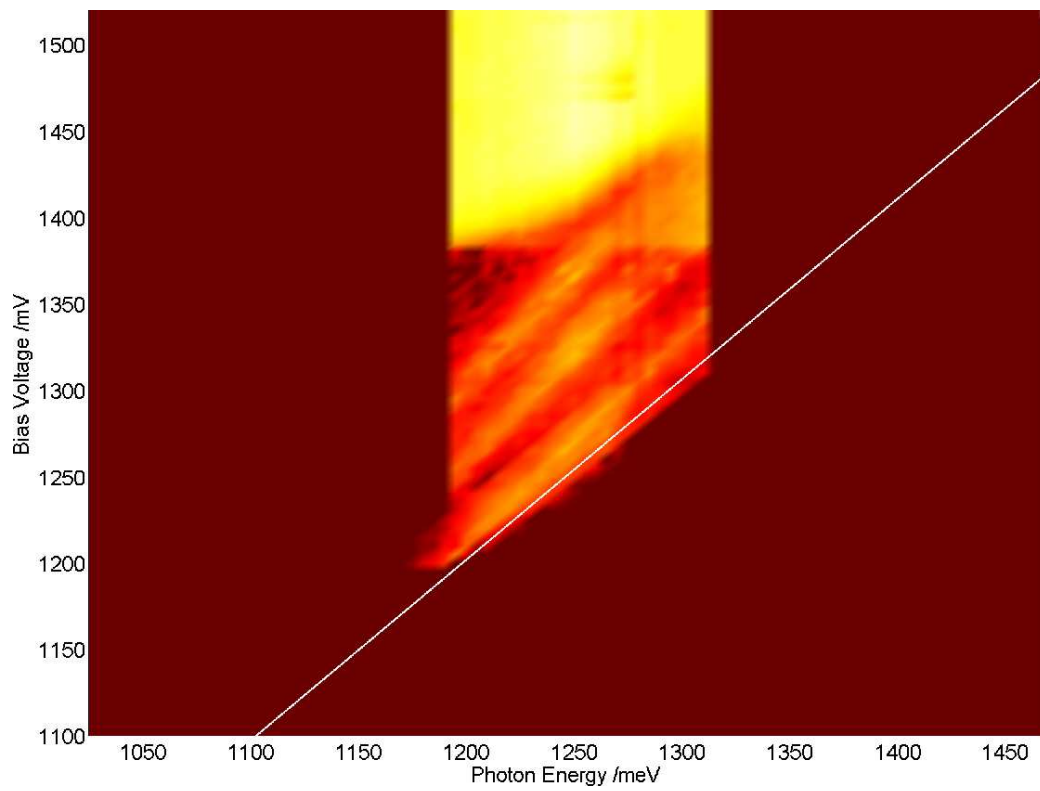


Figure 4.2.6: EL colourscale plot with Coulomb Interaction

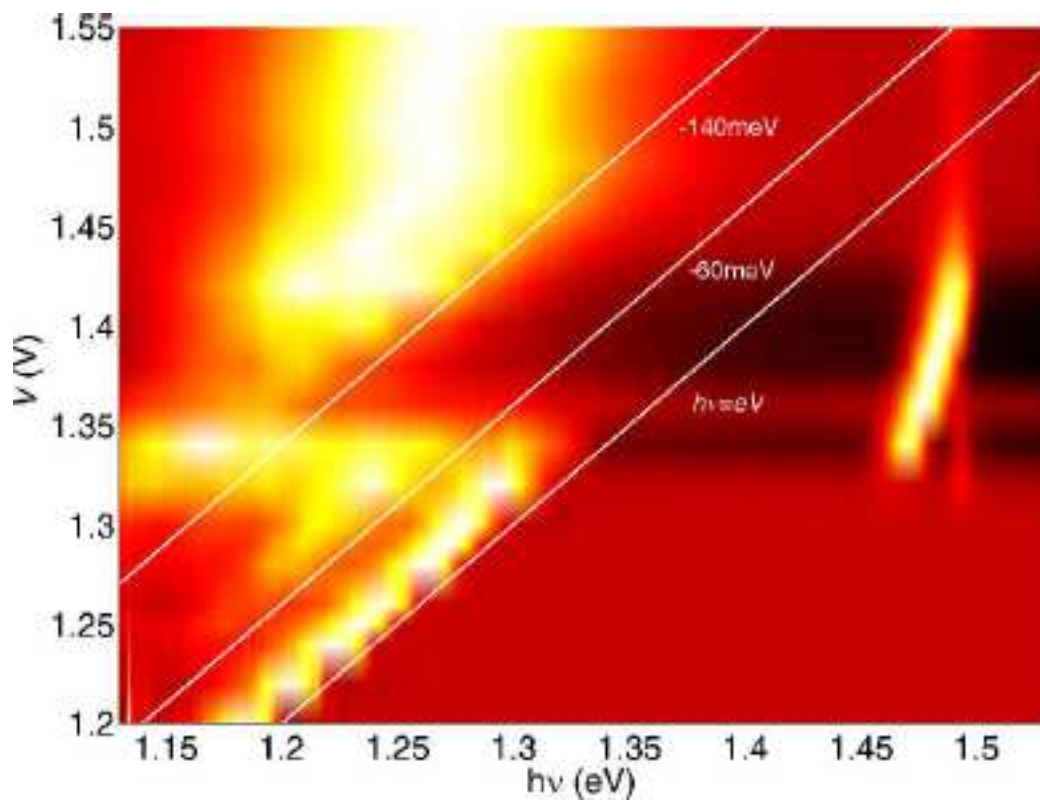


Figure 4.2.7: Experimental EL colourscale plot

Chapter 5

Analysis of Simulation

This chapter analyses the model in more detail, and looks at the effect of including some secondary interactions within the model.

5.1 Delayed Recombination Effects

For a single QD in a p-i-n junction, we can raise the Bias Voltage so that either the electron levels or the hole levels are aligned to the relevant junction, and resonant tunnelling may occur. However, with the inclusion of the Coulomb Interaction between the electrons and holes tunnelling onto the dot, we see that once one species has tunnelled onto the dot, the energy levels will shift by an amount, U (which we estimate for a typical dot to be approximately 13meV), and no further tunnelling may take place, as the resonant condition will be lost. If we combine this with a linear increase or decrease in bias voltage, the result is a delayed tunnelling effect, in which each carrier is able to tunnel just once at each resonant voltage, and then radiatively recombine once its counterpart has tunnelled on after an increase or

decrease in current. For a typical QD, with a single ground-state and two excited states present, just 5 photons will be emitted over the full voltage sweep, as shown in figure 5.3.1.

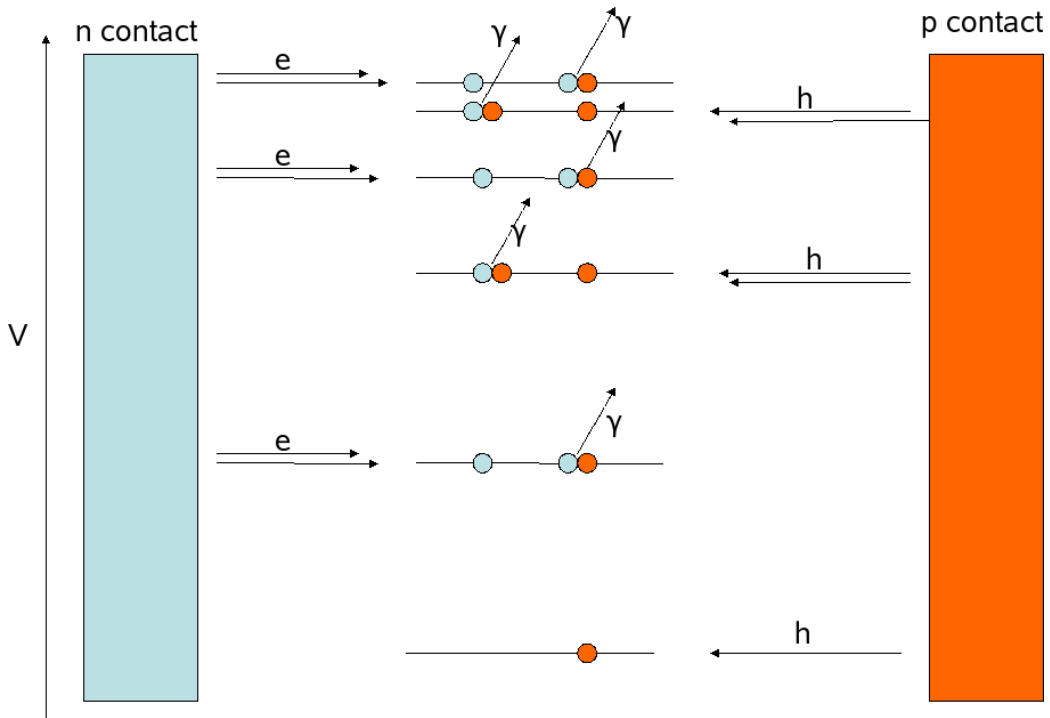


Figure 5.1.1: Only a limited number of photons can be emitted via delayed recombination as the voltage increases

This delayed recombination effect, in which photons are only emitted after a change in bias voltage should show up in the computational simulation of the system. One way to test for this effect is to introduce a parameter which removes all the carriers from the dot at every change in voltage, and compare the results with the normal case. This parameter is denoted as the “leakage current, but it is not proposed that it is a real effect in the system, although it is not entirely unlikely that carriers may escape from the dots on some timescale. Figure 5.1.2 shows the EL characteristics of the system with and without the leakage current present.

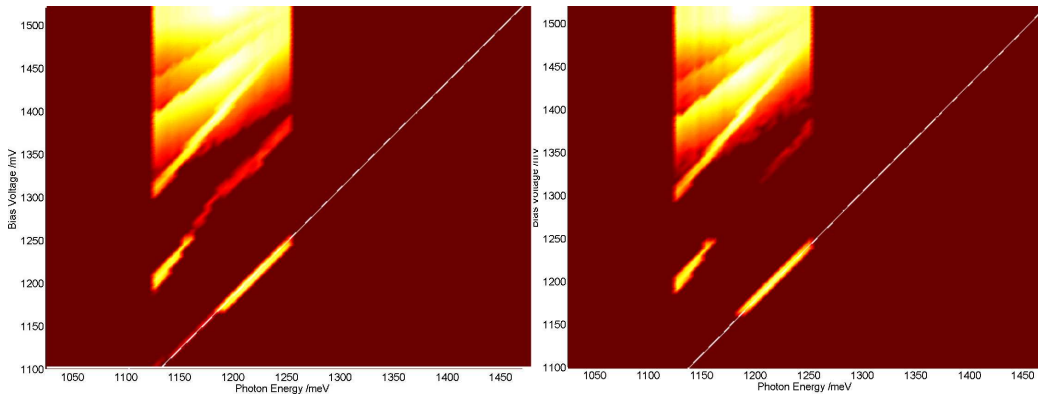


Figure 5.1.2: EL colour-scale plot with leakage current without Coulomb interactions compared to no leakage case

We can clearly see two noticeable differences between the two plots, highlighting the areas where the delayed recombination is the primary mechanism of photon emission. The two areas in question are at bias voltages 1.2-1.25V and 1.3-1.35V. The remainder of the luminescence is thus caused by direct recombination within the system.

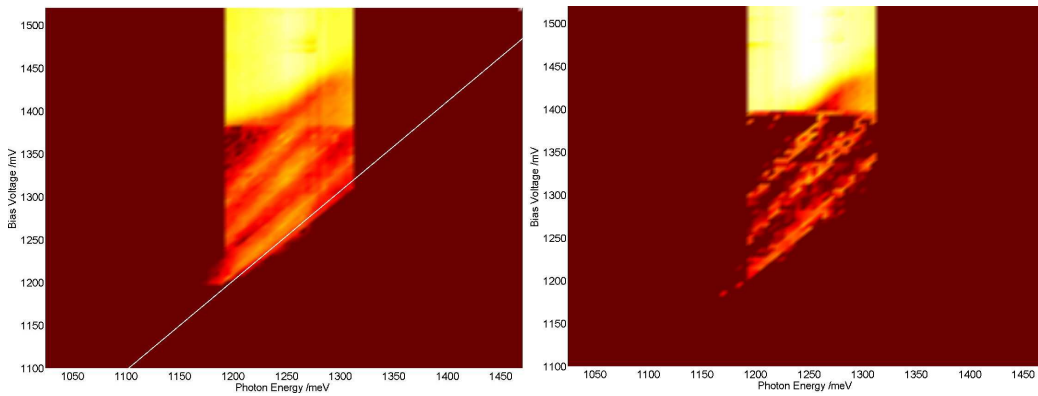


Figure 5.1.3: EL colour-scale plot with leakage current with Coulomb interactions compared to the no leakage case

We can also repeat the investigation for the case in which the Coulomb interaction is included. Figure 5.1.3 shows the resultant colourscale plot comparison.

The effect here is also clear, the solid lines of direct carrier recombination electroluminescence remain the same, but the emission from the gaps is noticeably decreased, as any remaining carriers are removed before delayed recombination can take place. This demonstrates neatly the areas of electroluminescence which are a result of Coulomb-modified direct carrier recombination, and which are a result of delayed recombination.

In chapter 3, we analysed the “jump” in intensity of transport and luminescence between 1.25 and 1.3V, and concluded that it was caused by simultaneous electron and hole tunnelling into the same dot, caused by the asymmetric location of the dot array within the intrinsic region. We also saw that the inclusion of the Coulomb interaction flattened out this peak. Having now isolated the effects of delayed recombination, we can study what the effect is on the transport characteristics of the system for a range of symmetric and asymmetric dot configurations.

The total width of the intrinsic region is 16nm, and the alignment studied thus far was for the dot array to be placed offcenter, 7nm from the n contact and 9nm from the p contact. We denote the distance from the n contact as d , and the distance from the p contact is therefore $16 - d$. We now study the effects of three different configurations: $d = 5$, $d = 9$ and the symmetric case $d = 8$. A schematic of the cases A $d = 7$ and B $d = 9$ is shown in figure 5.1.4. We also define a third configuration C for the case $d = 5nm$.

We compare the three asymmetric samples both without and with Coulomb interactions included in the simulation. Figure 5.1.5 shows the IV curves for the $d = 5nm$, $d = 7nm$ and $d = 9nm$ configurations. Both curves feature a steady increase in current, punctuated by large peaks in the 1.2-1.4V region, which, as was discussed in chapter 3, is caused by the simultaneous resonant tunnelling of elec-

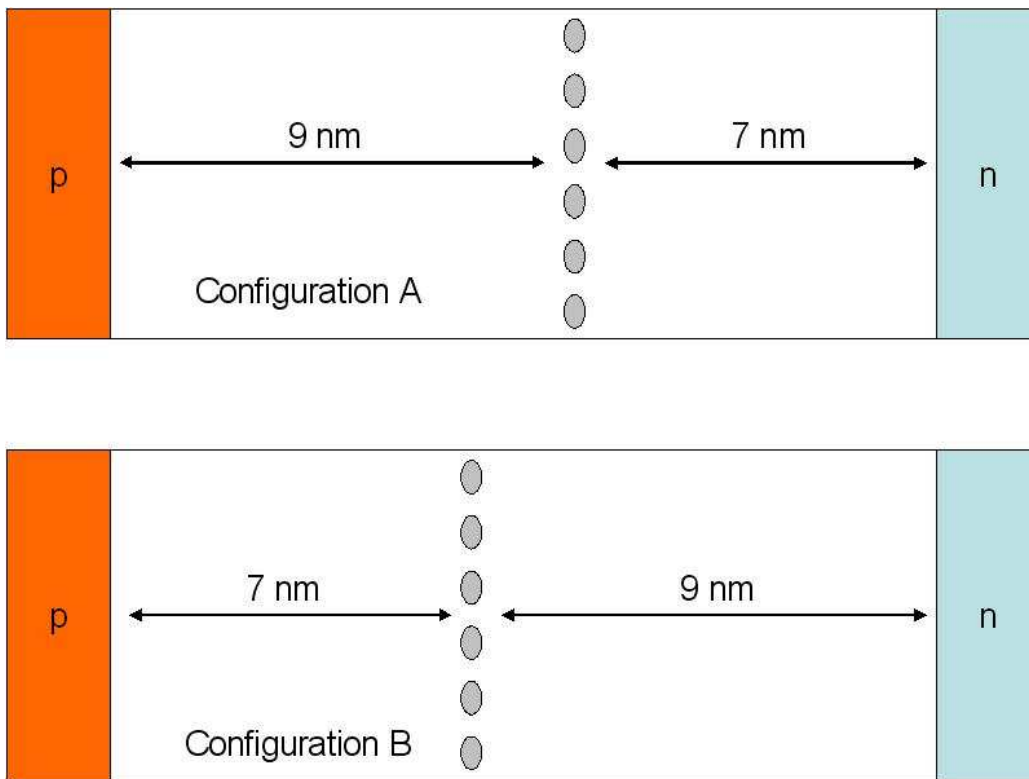


Figure 5.1.4: Two different dot array locations within intrinsic region

trons and holes due to the asymmetric nature of the configurations. Therefore it is expected that the two different asymmetric configurations should exhibit peaks at different bias voltages, as the region at which the simultaneous resonance occurs is dependent upon the exact nature of the asymmetry. For configurations A and B, the peaks occur when carriers are able to resonantly tunnel into the ground-states of the dots and recombine. For configuration C, we see two narrower peaks between 1.25 and 1.3V. In this case, the extreme asymmetry of the configuration allows for simultaneous tunnelling into the groundstates and excited states of the same dots. The carriers then relax non-radiatively into the groundstate before recombination.

Figure 5.1.6 shows the IV curves for configurations A and B, but this time

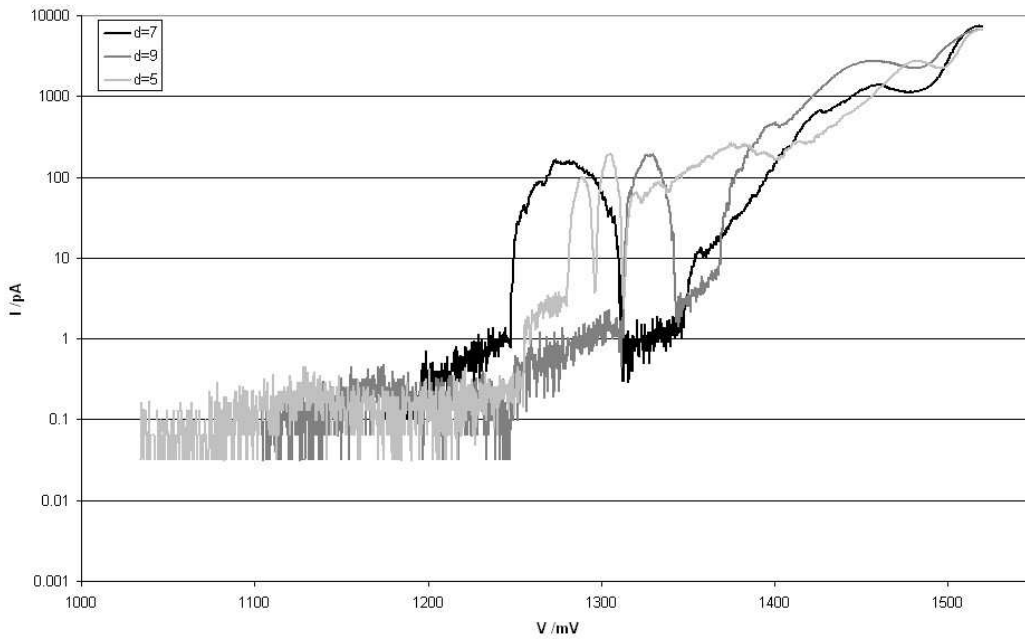


Figure 5.1.5: Comparison of IV plots for configurations A ($d=7$) and B ($d=9$) and C ($d=5$) with no Coulomb interactions included in the simulation

with the Coulomb interactions included. We see that any significant differences between the two curves in figure 5.1.5 have now been minimised. There are small differences between the curves, but the distinctive features have been removed by the feedback effects of the Coulomb interaction.

We also consider the symmetric case $d = 8nm$. For this case, no simultaneous resonant tunnelling is possible, and thus we expect not to see a peak in the 1.15-1.4v region, as seen in the asymmetric cases. In figure 5.1.7 we compare the symmetric $d = 8nm$ case both with and without Coulomb interactions included. The Coulomb interactions clearly allow for a degree of simultaneous resonant tunnelling between 1.1 and 1.4V, which would otherwise not be present. This leads to a noticeably increased current.

5.1. Delayed Recombination Effects

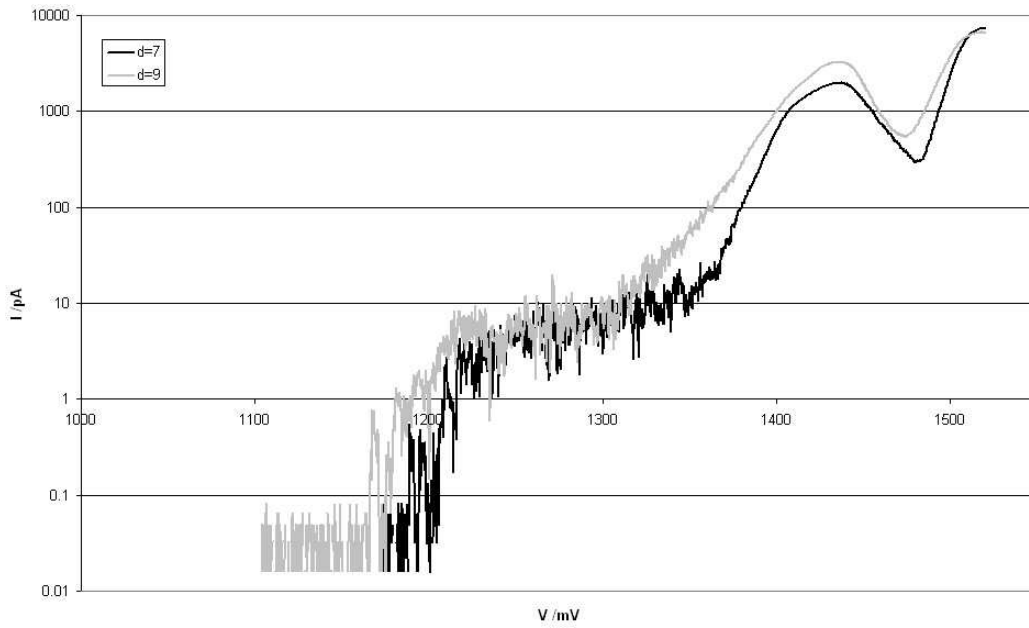


Figure 5.1.6: Comparison of IV plots for configurations A ($d=7$) and B ($d=9$) with full Coulomb interactions included in the simulation

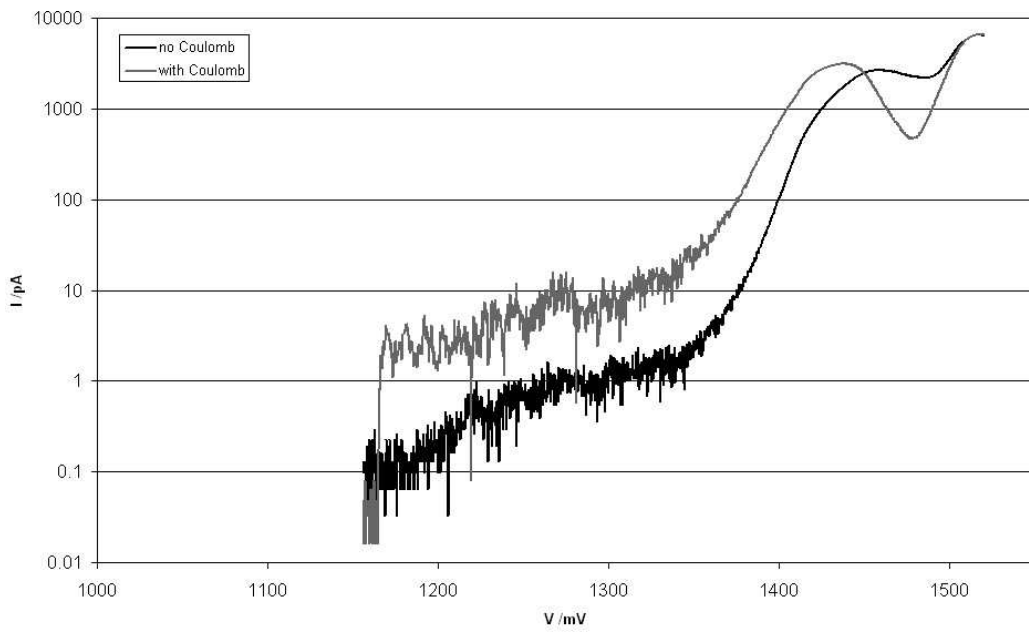


Figure 5.1.7: Comparison of IV plots for symmetric case $d = 8$ nm both with and without full Coulomb interactions included in the simulation

5.2 Many Dot Interactions

In section 4.1, we discussed the effect of the Coulomb interaction between carriers on neighbouring dots on the energy levels and the tunnelling rates from the contacts. The Coulomb interaction energy between two nearest neighbouring dots was given as approximately 0.5meV . If several neighbouring dots had a similar charge, the total interaction energy could approach 2 or 3meV , enough to repel or attract the contact carrier sea by 0.5nm , making a significant distortion in the tunnelling distance. This is shown in figure 5.2.1.

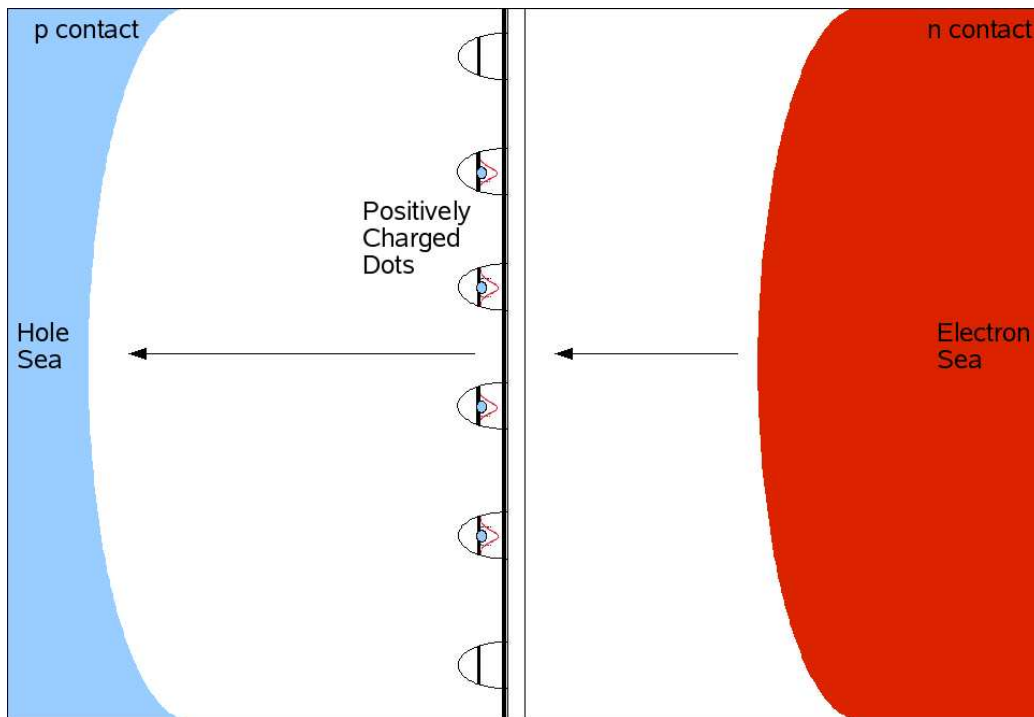


Figure 5.2.1: Neighbouring Dot Interactions

As the simulation is run, and carriers tunnel into the dots and subsequently recombine, the Coulomb interaction between the contacts and the dot array causes a constant flux in the tunnelling distance. We can take snapshots of these fluctua-

tions at a range of bias voltages, in order to be able to characterise the length scale over which these fluctuations take place.

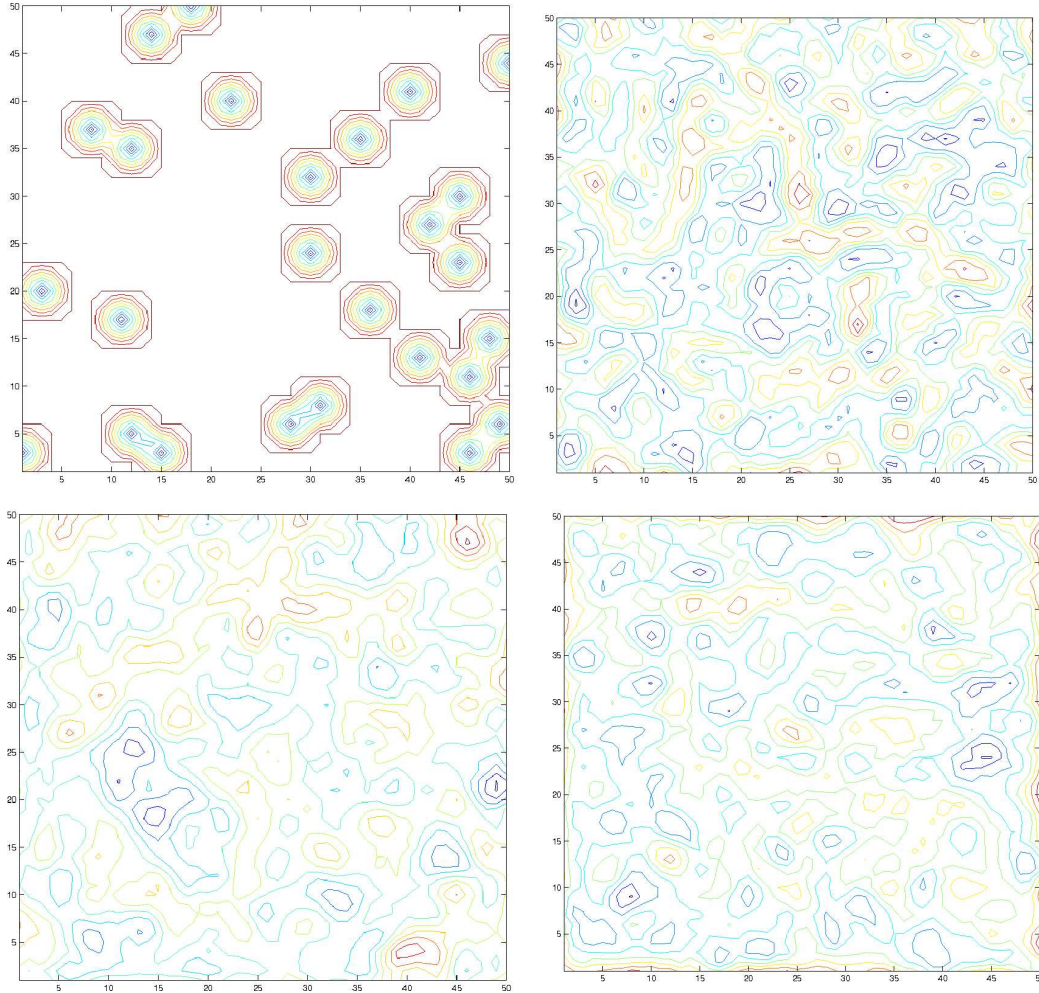


Figure 5.2.2: An xy plot of the dot array showing the distance of the electron Fermi sea from the dot. Bias Voltages: top left, 1.175V; top right, 1.375V; bottom left, 1.425V; bottom right, 1.475V.

A series of contour diagrams showing the Coulomb interaction induced deformation of the contact sea at a range of different bias voltages is shown in figure 5.2.2. At 1.175V, several dots are occupied, and we can see fluctuations in the Coulomb field around these points in the dot array. In extrema, a perfectly an-

tisymmetric electron hole distribution (ie. electrons and holes alternately placed on neighbouring dots) would have a mean fluctuation of the area occupied by an individual dot, while a perfectly symmetric distribution, for example a completely homogeneous dot occupation by electrons or holes, would have a fluctuation covering the entire array of 2500 dots.

We can study how the fluctuation varies between these two extreme cases as we increase the bias voltage. At 1.174eV, we see localised fluctuations as a handful of electrons begin to occupy the dots. The mean fluctuation diameter remains constant between 1.25 and 1.375V, before increasing dramatically to a peak at around 1.4V, and finally decreasing again at 1.475V. This effect is shown in figure 5.2.3, where we can see a clear peak in the correlation length at approximately 1.4V. We can compare the changes in correlation length to the changes in dot occupation, and the two plots are clearly related. As the tunnelling rate overtakes the recombination rate, the carriers start to fill up the dots, and this subsequently leads to larger Coulomb fields being generated around the array, affecting both the energy level resonances and the distortion of the electron and hole Fermi seas. This feedback effect in turn leads to a larger degree of fluctuation in the Coulomb field around the dot array, and larger correlations in the electron and hole sea distortions. In chapter 6, we will see that these fluctuations are not static, but rather are dynamic in time as carriers tunnel into the dots and recombine.

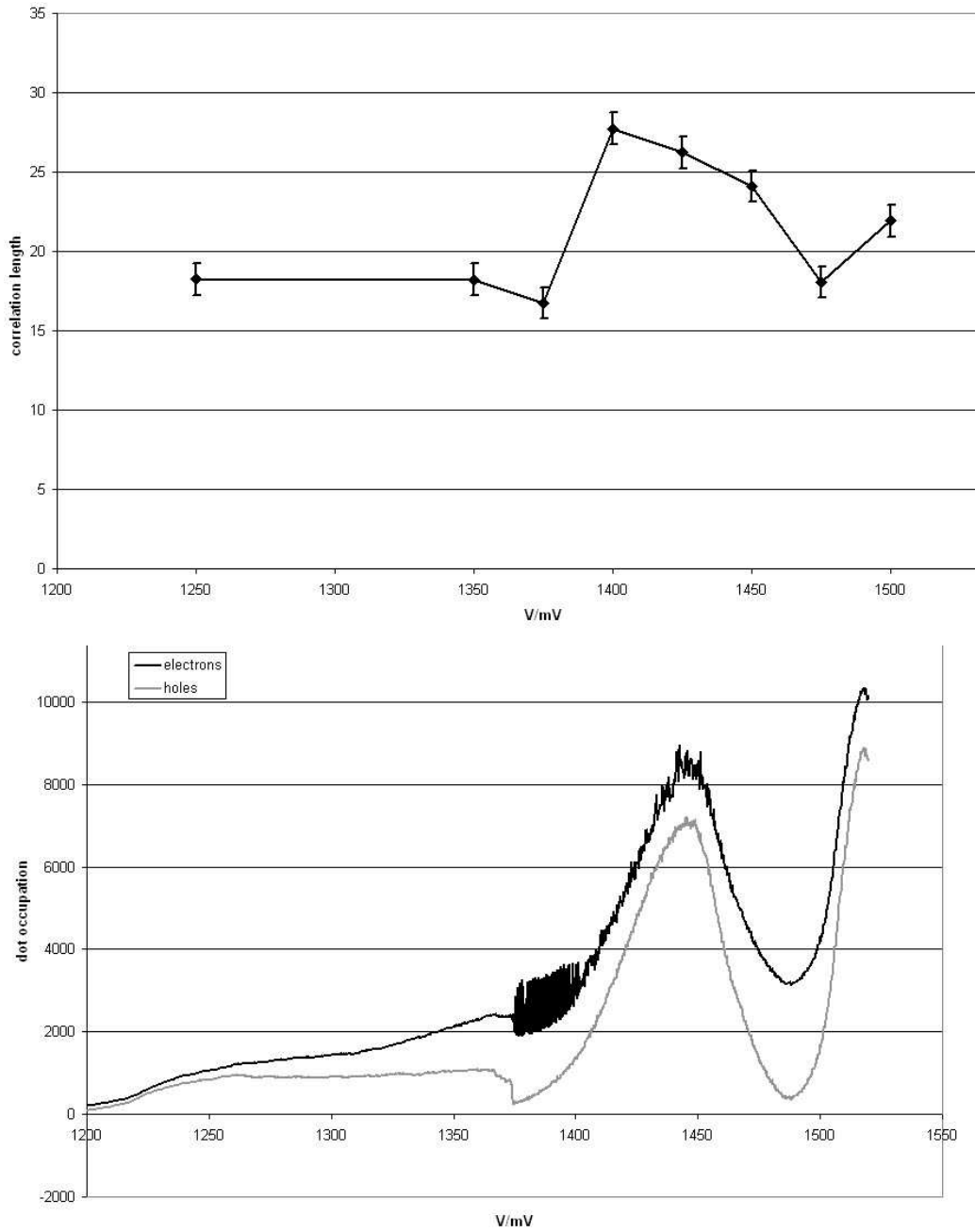


Figure 5.2.3: Variation of Coulomb field correlation length with bias voltage

5.3 Up Conversion Luminescence

Up Conversion Luminescence (UCL) is the emission of photons at energies larger than that supplied by the external energy source. It has previously been seen in self-assembled InAs/GaAs dots. [39] Figure 5.3.1 shows an experimental EL plot [8], which clearly shows a strong emission line on the right of the diagram, at higher photon energies than the bias voltage provided. In this section we discuss the process by which this UCL is being realised, and present a calculation of the effect of magnetic field on the luminescence.

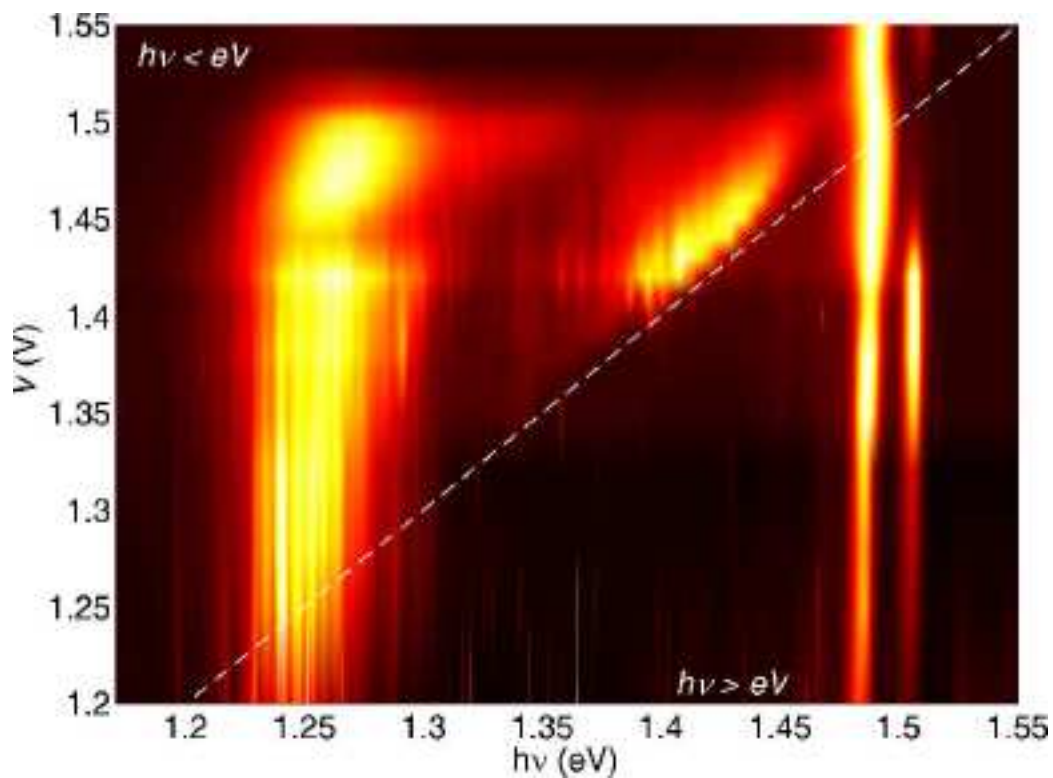


Figure 5.3.1: Evidence of UCL in experimental plots

Several processes have been suggested as possible mechanisms of UCL, including phonon assisted processes [39], multi-photon absorption [40], and Auger

processes [41]. Of these suggestions, multi-photon absorption can immediately be ruled out, as the experimental data is electroluminescence, as opposed to photoluminescence, as the device in question is not excited by light, and at a bias voltage of zero Volts, no emission was detected.

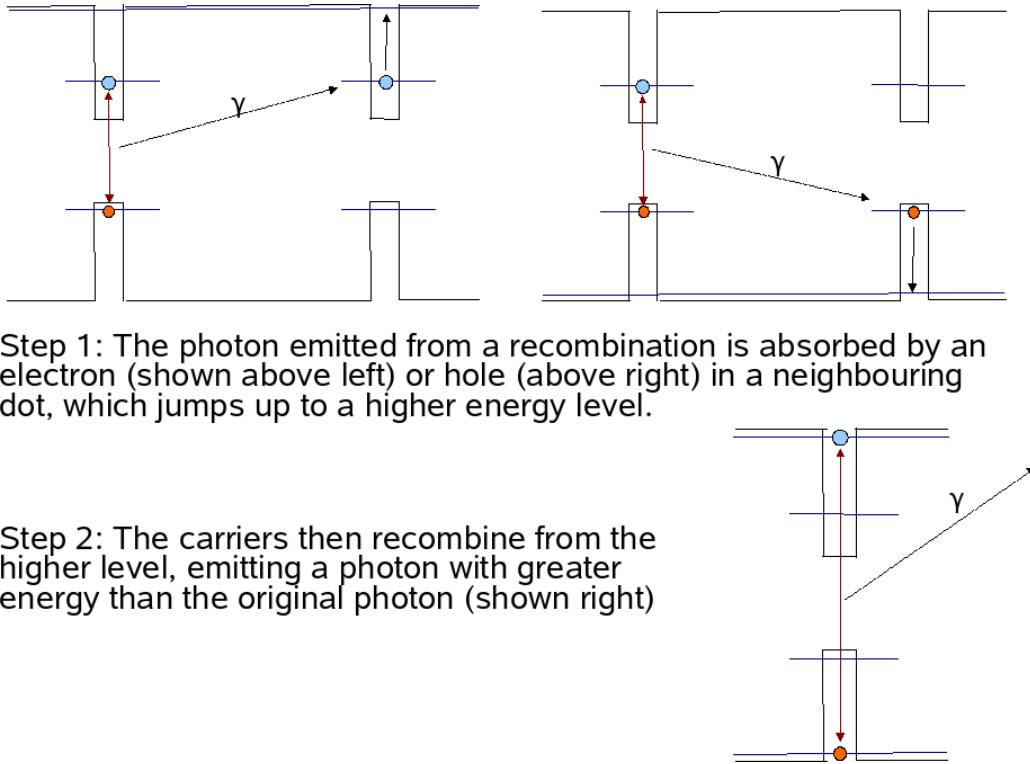
The concept of phonon assisted UCL was investigated when the experiments were performed. Increasing the temperature of the sample will increase the number of available phonons, thus indicating that if phonons are strongly involved in the UCL mechanism, the UCL will increase at increasing temperatures. In fact the UCL decreased, from which we may conclude that phonon assisted processes were not the dominant mechanism.

Auger processes involve the photon emitted by an excitonic recombination being reabsorbed by another electron or hole on that dot or a neighbouring dot. The carrier is then excited into the GaAs conduction (valence) band, from where it relaxes to the band edge, before either recombining excitonically, or relaxing into another dot. In order to include this process in the full simulation, we first need to calculate the overlap integral associated with the excitation process. The proposed mechanism is shown in figure 5.3.2.

For the Auger process, the transition between the electron groundstate and conduction band state, represented by $c_w^\dagger c_e$ is stimulated by a photon of energy $\hbar\omega$ in the region of 1.2 to 1.4eV. The probability per unit time that an atom in state $|e\rangle$ makes a transition to a state $|w\rangle$, stimulated by electromagnetic radiation is:

$$\frac{\pi e^2}{3\varepsilon\hbar^2} |\langle w|r|e\rangle|^2 \quad (5.3.1)$$

where ε is the permittivity of GaAs, e is the electronic charge, and $|\langle w|r|e\rangle|$ is



Step 1: The photon emitted from a recombination is absorbed by an electron (shown above left) or hole (above right) in a neighbouring dot, which jumps up to a higher energy level.

Step 2: The carriers then recombine from the higher level, emitting a photon with greater energy than the original photon (shown right)

Figure 5.3.2: Proposed Mechanism of Auger Process

the overlap between the 2 states.

For the transition:

$$V_{we}c_w^\dagger c_e, \quad (5.3.2)$$

the matrix element

$$V_{we} = \int dr \Psi_w \Psi_e. \quad (5.3.3)$$

We can therefore calculate the element by integration:

$$V_{we} = \int_0^{2\pi} d\theta \int_{-\Lambda/2}^{\Lambda/2} dz \cos^2(\pi z/\Lambda) \int_0^\infty d\rho e^{-(\rho-R)^2/l_w^2} e^{\rho^2/l_e^2} \quad (5.3.4)$$

where Λ is the confinement in the z direction, l_w and l_e are the radial confinement

lengths for the two states, and ρ and R are the locations of the two states.

We can rearrange to give:

$$V_{we} = \int_0^{2\pi} d\theta \int_{-\Lambda/2}^{\Lambda/2} dz \cos^2(\pi z/\Lambda) \int_0^\infty d\rho e^{-R^2/l_w^2} e^{-a^2\rho^2} e^{-b\rho} \quad (5.3.5)$$

where

$$a^2 = \frac{l_e^2 l_w^2}{l_e^2 + l_w^2} \quad (5.3.6)$$

and

$$b = \frac{-2R}{l_w^2} \quad (5.3.7)$$

Completing the integration gives:

$$V_{we} = 2\pi \left[z + \cos\left(\frac{2\pi z}{\Lambda}\right) \right]_0^\Lambda \frac{\sqrt{\pi} e^{-R^2/l_w^2}}{2} \left[\frac{e^{(b/2a)^2}}{a} \text{Erf} \left(\frac{b}{2a} + a\rho \right) \right]_0^\infty \quad (5.3.8)$$

$$= \frac{\pi^{3/2} \Lambda}{a} e^{-R^2/l_w^2} e^{(b/2a)^2} (1 - \text{Erf}(b/2a)) \quad (5.3.9)$$

We can now include this rate in our simulation, and study the effect on the resultant EL colour-scale plot, shown in figure 5.3.3.

We also show the experimental EL plot, which highlights the similarities between the two. The emission line at $hf = 1.52eV$ is visible in both, and continues below the $eV = hf$ point as UCL. The bright patch on the experimental plot at around 1.43eV is most likely direct emission from the wetting layer. This is not included in the simulation, and thus a corresponding bright patch is not visible in the numerical plot.

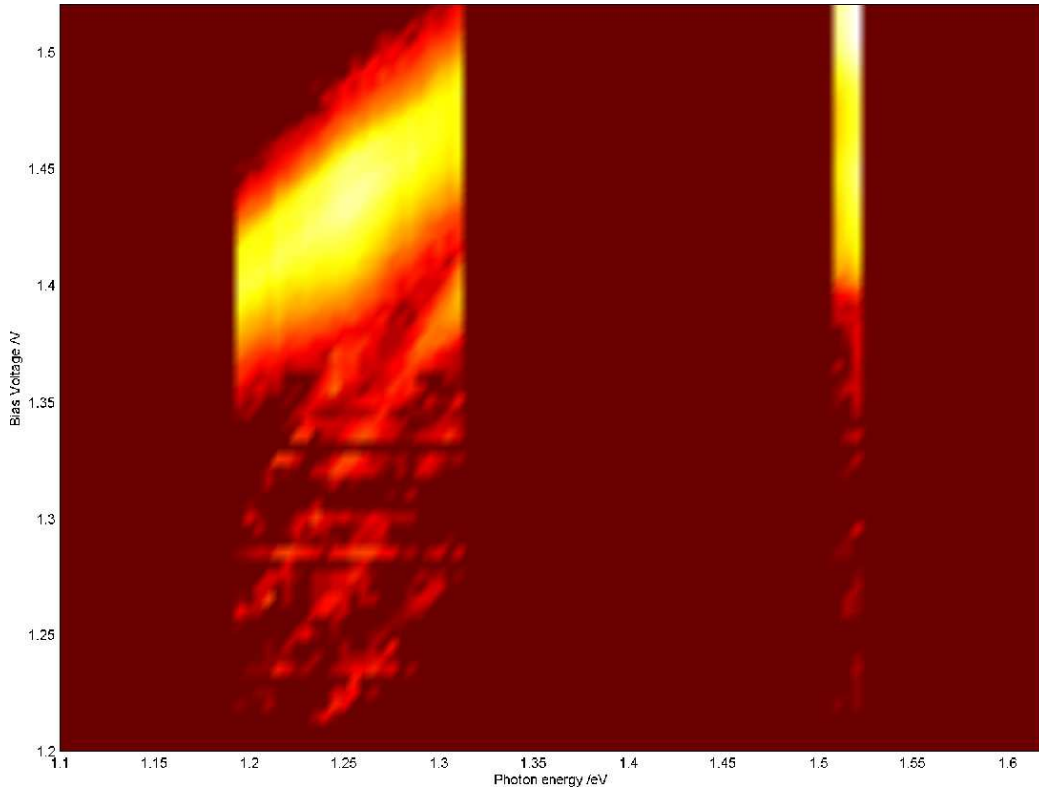


Figure 5.3.3: Simulated UCL colourscale plot and spectra

One way to test the validity of the Auger mechanism theory is to study the effect of a magnetic field on the experimental and theoretical results. l_w and l_e are the length scale of the wavefunctions within the dot and the conduction band. To assess how these are affected by magnetic field, we must take into account the magnetic confinement length l_B , which will affect the localization of the carrier within its potential.

The dependence of l_B on field strength is given by

$$l_B = \sqrt{\hbar/eB}. \quad (5.3.10)$$

We can see the effect of increasing magnetic field strength from 0T up to

14T is to reduce the up-conversion luminescence strongly at relatively low field strengths. This can be understood by considering the confinement effect of the magnetic field on the carrier wavefunction in the conduction/valence band, and the resulting reduction in the overlap integral.

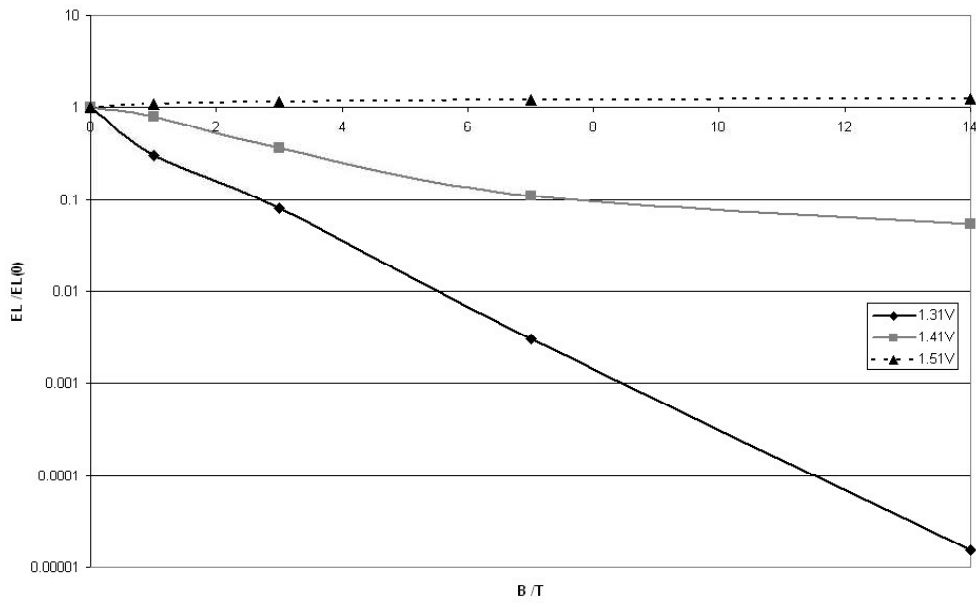


Figure 5.3.4: Simulated relationship of UCL current with Magnetic Field (logarithmic scale)

The results of the simulation clearly compare well with the experimental results, and offer some insight into what physical processes are likely to be occurring in the real system. However, it is relevant to consider the number of assumptions involved in the route from theoretical model to simulation. Had these assumptions been different, then it is important to consider the implications that this may have had on the results of the simulated data. Assumptions were made in the modelling of the dot energy levels, the calculation of the tunnelling, relaxation, and recombination rates, and the effect of the Coulomb interaction.

The effect of changing the energy levels of the dot would lead to a shift in both the bias voltages at which certain features are visible, and the energy of the photons emitted. We can see an example of these types of shifts in our study of the effect of varying the location of the dot array within the intrinsic region in section 5.1. This also enables us to work backwards from the experiment to the theory; as the location of key features matched up well with the simulation, this suggests that the model used to generate the dot energy levels was appropriate. The effects of a different set of rates would lead to a buildup of carriers at a different bias voltage, and the increased or decreased relevance of Coulomb effects. In the simulated results, the high relaxation rate combined with the low excited state to excited state recombination rate results in zero photon emission with energies between 1.32 and 1.5eV; whereas we can see from the experimental EL plot (figure 5.3.4) that there is evidence that such emission does exist. The effect of the Coulomb interaction on the IV and EL plots were to remove some features not seen in experimental results, suggesting that Coulomb interactions do play an important role in the transport of carriers through the dots. In summation, the notable similarity between simulated and experimental results suggests that the assumptions made in the theoretical

modelling of the system were appropriate.

Chapter 6

Correlated Tunnelling Regime

Analysis

In this chapter we study a particular regime seen in the results of the 2500 dot model involving correlated tunnelling of electrons and holes into the same dot, and use the master equation method to derive some of the key features of the process.

6.1 Correlated Tunnelling Regime

We saw in chapter 4 that when the Coulomb interaction is included in the simulation, the simultaneously resonant condition that led to the jump in tunnelling and recombination phenomena in chapter 3 becomes blocked by the Coulomb energy of the carriers. The Coulomb energy of the occupying carrier moves the dot energy levels away from resonance and prevents further tunnelling. There is a scenario in which the bias voltages at which the electron and hole levels becomes

resonant are separated by approximately 12.8 meV. In this case, once the correct bias voltage is reached a correlated tunnelling regime (CTR) will occur. First one carrier species will resonantly tunnel onto the dot, creating a shift in the dot energy levels, then the other species will now be in resonance, and will be able to tunnel, creating an exciton, and returning the energy levels to their original values. Note that this can be achieved for both the spin up and spin down carriers in the dot simultaneously, (but not independently), approximately doubling the effective rate. The principle steps of the regime can be seen in figure 6.1.1.

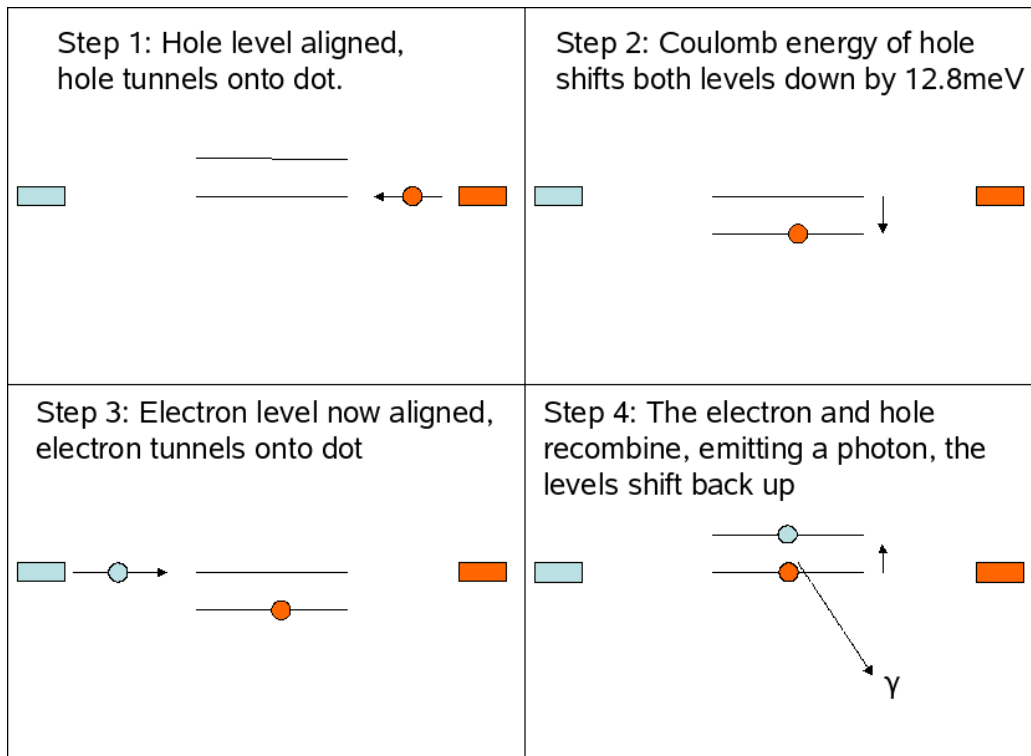


Figure 6.1.1: Correlated Tunnelling Regime Mechanism

The correlated tunnelling regime therefore results in a sizeable increase in the tunnelling current through the QD, and, more importantly, a significant current is generated without a change in bias voltage. The electron and hole groundstates

are initially separated by 30meV. We saw in chapter 3 that this gap does not mean that electrons and holes cannot be simultaneously resonant into the same dot, due to the effects of the asymmetric position of the dot array within the intrinsic region. For correlated tunnelling to occur, the two energy levels need to be offset by 12.8meV. This occurs twice - once for negatively charged dots, and once for positively charged. Once we include the subtle effects of the Coulomb interactions from neighbouring dots of course, the system becomes much more complicated and difficult to predict. We find that the conditions necessary for CTR to occur arise at two ranges of voltages, either side of the 1.25-1.3V condition of simultaneous resonance seen in chapter 3. CTR is only seen in the fraction of dots which possess both the right offset between electron and hole energy levels for CTR to occur, and have one of these levels in resonance. It is also possible for a dot to be pushed into or out of the regime by the energy shift caused by a carrier tunnelling onto a neighbouring dot.

We can see evidence of correlated tunnelling by studying time series data from the simulation. Figure 6.1.2 shows the tunnelling phenomena into an array of 100 dots over 100 timesteps. For dots 49, 76 and 80 in particular, we see electrons and holes tunnelling alternatively into the dots. Due to the effects of neighbouring dots and several energy levels being close to resonance simultaneously, the tunnelling is not perfectly alternate - ie. we occasionally see two electrons tunnel in a row, as the change in Coulomb energy, combined with a particular occupancy of nearby dots brings a second electron level into resonance, rather than the expected hole state.

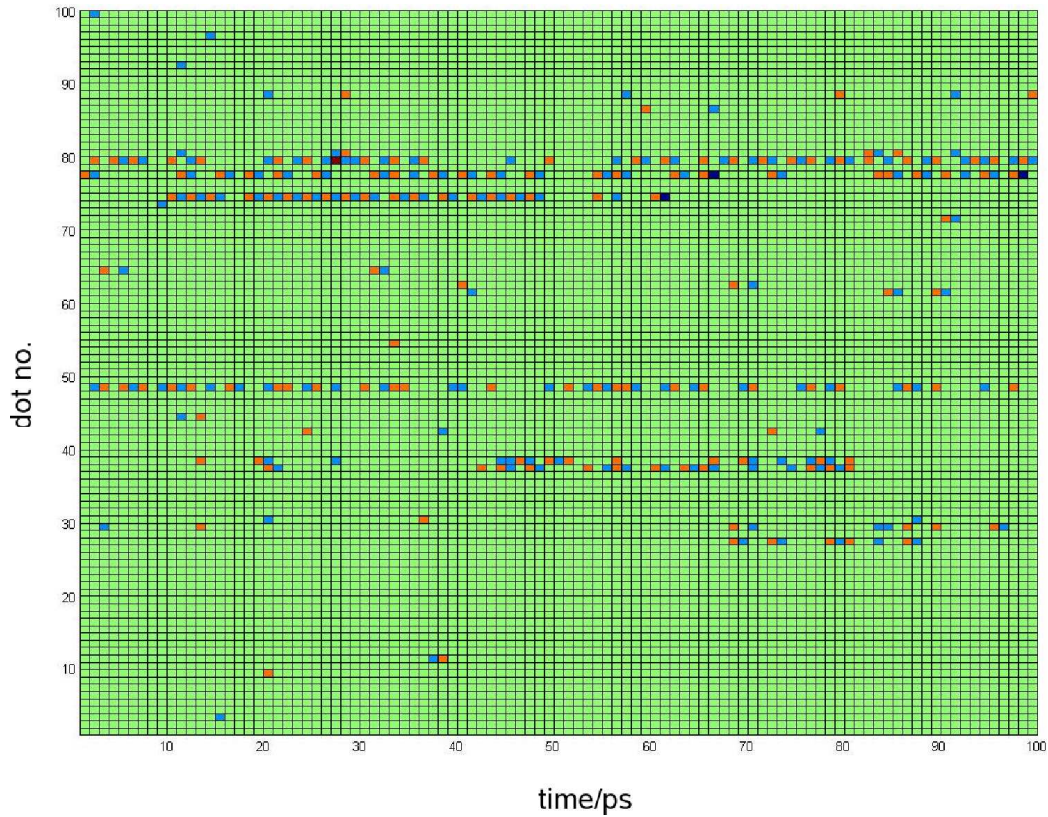


Figure 6.1.2: Time Series showing electrons and holes tunnelling sequentially. The figure shows the tunnelling events of 100 dots over a period of 100 timestep. The green squares indicate no tunnelling event, the blue squares indicate electron tunnelling, and the orange squares indicate hole tunnelling.

6.2 CTR in a single quantum dot

In the previous section, the possibility of a dot possessing the correct energy level distribution for correlated tunnelling state to occur was discussed. The regime can be seen to occur at a particular voltage at which one carrier species is directly resonant with the dot energy state, whilst the complementary species was off-resonance by an energy comparable to the Coulomb interaction energy between two electrons occupying a dot. The probability of this regime occurring at some voltage between zero and flat band was discussed in the previous section, and the

existence of such a regime in a large scale model was demonstrated.

We are now in a position to analyse this novel system in far greater detail.

We are able to describe the system as occupying one of three discrete possible states. For convenience, we decide that the p-contact is in direct resonance and the n-contact is off resonance by 12.8meV, and will become directly resonant when the QD is occupied by a single hole. On a qualitative level, the analysis would be exactly the same if the system were chosen to be the other way around. The three states the system can occupy are the “down” state, where the dot is unoccupied, the “zero” state, where the dot is occupied by a hole, and the “up” state, where the dot is occupied by an electron and a hole. There is no state where the dot is occupied solely by an electron, as the tunnelling rate from the n contact is zero for an unoccupied dot.

The three possible states can be seen in Figure 6.1.1. The system can be seen to move progressively from state up to state down to state zero, with the possibility of a backwards move not eliminated at this stage. Each movement between states is associated with a tunnelling or recombination rate. These rates can be taken from the rates calculated in the full 2500 QD system.

We now use two complementary methods to study the time evolution of the system. A small scale computer model is able to simulate the behaviour of the regime over 100,000 time-steps, from which we are able to calculate the transport and electroluminescent characteristics of the dot, as well as their associated noise characteristics. We are also able to analyse the system using the master equation method, the details of which are explained in greater detail in chapter 2 and [30]. This will provide us with predictions that we are then able to compare with the simulated data. Both of these methods have the advantage that we are not obliged

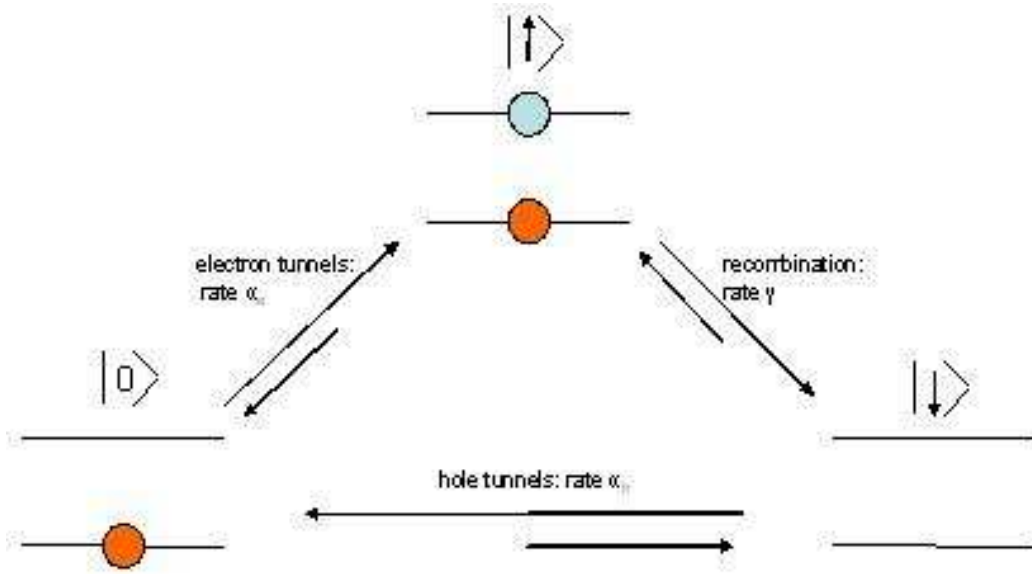


Figure 6.2.1: Three Possible States of CTR system

to input the tunnelling and recombination rates until the last step, allowing us to compare the effects of varying these rates.

The Hamiltonian for the system can be separated into expressions for the system, the bath, and the interactions:

$$H_{tot} = H_S + H_B + H_I \quad (6.2.1)$$

where

$$H_S = \varepsilon_{\uparrow} |\uparrow\rangle \langle\uparrow| + \varepsilon_{\downarrow} |\downarrow\rangle \langle\downarrow| \quad (6.2.2)$$

$$H_B = \sum_Q \left(\varepsilon_l \hat{l}_Q^\dagger \hat{l}_Q + \varepsilon_r \hat{r}_Q^\dagger \hat{r}_Q + \varepsilon_{\gamma} \hat{\gamma}_Q^\dagger \hat{\gamma}_Q \right) \quad (6.2.3)$$

Description	Bath Operator	Associated State Change
hole tunnels in from right contact	r	$ \downarrow\rangle \longrightarrow 0\rangle$
hole tunnels out into right contact	r^\dagger	$ 0\rangle \longrightarrow \downarrow\rangle$
electron tunnels in from left contact	l^\dagger	$ 0\rangle \longrightarrow \uparrow\rangle$
electron tunnels out into left contact	l	$ \uparrow\rangle \longrightarrow 0\rangle$
exciton recombines, photon emitted	γ^\dagger	$ \uparrow\rangle \longrightarrow \downarrow\rangle$
exciton forms, photon absorbed	γ	$ \downarrow\rangle \longrightarrow \uparrow\rangle$

Figure 6.2.2: Associations between bath and system processes, with a description of the corresponding event

$$\begin{aligned}
 H_I = \sum_Q \left(v_Q \hat{l}_Q^\dagger |0\rangle \langle \uparrow| + v_Q \hat{l}_Q |\uparrow\rangle \langle 0| + w_Q \hat{r}_Q |0\rangle \langle \downarrow| \right. \\
 \left. + w_Q \hat{r}_Q^\dagger |\downarrow\rangle \langle 0| + u_Q \hat{\gamma}_Q^\dagger |\downarrow\rangle \langle \uparrow| + u_Q \hat{\gamma}_Q |\uparrow\rangle \langle \downarrow| \right) \quad (6.2.4)
 \end{aligned}$$

We now wish to analyse this system using the interaction picture. We can separate the Hamiltonian into a series of System and Bath operators:

$$S_1 = |\uparrow\rangle \langle 0| e^{i\varepsilon_\uparrow t} \quad (6.2.5)$$

$$S_2 = |0\rangle \langle \uparrow| e^{-i\varepsilon_\uparrow t} \quad (6.2.6)$$

$$S_3 = |0\rangle \langle \downarrow| e^{-i\varepsilon_\downarrow t} \quad (6.2.7)$$

$$S_4 = |\downarrow\rangle \langle 0| e^{i\varepsilon_\downarrow t} \quad (6.2.8)$$

$$S_5 = |\downarrow\rangle \langle \uparrow| e^{-i\varepsilon t} \quad (6.2.9)$$

$$S_6 = |\uparrow\rangle \langle \downarrow| e^{i\varepsilon t} \quad (6.2.10)$$

where $\varepsilon = \varepsilon_\uparrow - \varepsilon_\downarrow$, and

$$B_1 = v\hat{l}e^{-i\varepsilon_l t} \quad (6.2.11)$$

$$B_2 = v\hat{l}^\dagger e^{i\varepsilon_l t} \quad (6.2.12)$$

$$B_3 = v\hat{r}^\dagger e^{i\varepsilon_r t} \quad (6.2.13)$$

$$B_4 = v\hat{r}e^{-i\varepsilon_r t} \quad (6.2.14)$$

$$B_5 = v\hat{\gamma}^\dagger e^{i\varepsilon_\gamma t} \quad (6.2.15)$$

$$B_6 = v\hat{\gamma}e^{-i\varepsilon_\gamma t} \quad (6.2.16)$$

From conservation of energy we can see that $\varepsilon_l = \varepsilon_\uparrow$, $\varepsilon_r = \varepsilon_\downarrow$, and $\varepsilon_\gamma = \varepsilon_\uparrow - \varepsilon_\downarrow$.

We can now calculate the correlation functions using the the Born-Markov approximation, and using the same method as was applied in chapter 2, we can define the Liouville equation:

$$\dot{\rho} = \mathcal{L}\rho, \quad (6.2.17)$$

where ρ is the density matrix and \mathcal{L} is the Liouville evolution operator, which can be expressed in matrix representation as

$$\mathcal{L} = 2\pi \begin{pmatrix} X_1 & J_\gamma(\varepsilon)(n_B(\varepsilon) + 1) & J_l(\varepsilon_\uparrow)n_F(\varepsilon_\uparrow - \mu_l) \\ J_\gamma(\varepsilon)n_B(\varepsilon) & X_2 & J_r(\varepsilon_\downarrow)(1 - n_F(\varepsilon_\downarrow - \mu_r)) \\ J_l(\varepsilon_\uparrow)(1 - n_F(\varepsilon_\uparrow - \mu_l)) & J_r(\varepsilon_\downarrow)n_F(\varepsilon_\downarrow - \mu_r) & X_3 \end{pmatrix}, \quad (6.2.18)$$

where J is the spectral density function and n_F and n_B are the Fermi-Dirac and Bose-Einstein distributions respectively. We can once again define

$$X_n = - \sum_{m, m \neq n} \mathcal{L}_{mn}. \quad (6.2.19)$$

By using the relationship $\dot{\rho} = 0$, we can find the eigenfunctions of the evolution operator, and predict the mean current and photocurrent, the occupation probability of each state, and the current and photocurrent noise through the system. We are able to generate these results for whatever tunnelling and recombination rates we wish to consider. We find the three eigenvalues, λ for the system, and their associated eigenvectors, V_R and V_L . The eigenvector associated with $\lambda = 0$ contains information about the steady state of the system.

We now need to consider the electron and hole resonant tunnelling rates into the dot, and the excitonic recombination rate. We can also consider the effect of non-zero tunnelling rates out of the dot, and a non-zero photon absorption rate, as these will have an effect on the current and photo-current and the associated current noise.

We now wish to study the noise characteristics of this system, which give us more detailed information about the system's dynamics. We do this by studying

the Fano factor of the system, defined as:

$$\mathcal{F} = \frac{S(\omega)}{2e \langle I \rangle}, \quad (6.2.20)$$

where, the noise, $S(\omega)$, can be calculated from the relevant current or photocurrent operator and the system eigenvectors using the relation given in [30] and developed in [42].

The symmetrized noise spectrum for any two operators a and b is:

$$S(\omega) = \lim_{t \rightarrow 0} \int_{-\infty}^{\infty} d\tau \langle \bar{a}(t + \tau), \bar{b}(\tau) \rangle e^{i\omega\tau} \quad (6.2.21)$$

Using the quantum regression theory and an eigenvalue expansion [42], we can define the noise spectra as:

$$S(\omega) = 2 \sum_{k=1}^n Re \left(\frac{\langle V_{L0} | I_k | V_{Rk} \rangle \langle V_{Lk} | I_k | V_{R0} \rangle}{(i\omega - \lambda_k)} + \frac{\langle V_{L0} | I_k | V_{Rk} \rangle \langle V_{Lk} | I_k | V_{R0} \rangle}{(-i\omega - \lambda_k)} \right) \quad (6.2.22)$$

where I is the current operator, V_R and V_L are the right and left eigenvectors, and λ is the associated eigenvalue. The tabulated results shown below were calculated using Matlab.

For a Poissonian distribution of photon emission, in which the photons are emitted independently, the Fano factor will be equal to one. A Fano factor of less than one indicates that the photons tend to be more evenly separated, known as *sub-Poissonian* noise, and a Fano factor of greater than one indicates that the photons tend to be emitted in bunches, known as *super-Poissonian* noise [43].

We calculate the photon noise and current noise through the system. The photon noise is the noise distribution of the photons being emitted from the sample.

Fano Factors	current noise	photon noise
Limiting Factor α_e, α_h	0.99	0.70
Limiting Factor γ	1.47	0.85

The current noise needs a more detailed understanding. We know that the current is related to the electrons tunnelling into the dots and the holes tunnelling out of the dots, but there are technically two possible ways of measuring the noise in the system, depending upon whether we treat the electron and hole tunnelling onto the dot as one single event, involving a quanta of charge moving from one contact to the other, or whether we treat the two tunnelling events as two separate occurrences. The noise spectra of the two methodologies will be different. The current noise spectra calculated is for the *second* case, in which the two events are treated separately. For the first case, the system will have only two alternating events: a “current” event and a “photon” event, the noise spectra will necessarily be identical. Looking at the results, we see that for the case in which the tunnelling rates are the limiting factor, the current noise is approximately Poissonian, and the photon noise is sub-Poissonian. This can be understood as being caused by there being relatively large period of time during which the carriers are tunnelling into the dots, which leads the photon emission events being spaced out in time, and thus the noise is sub-Poissonian. The photon emission time period is comparatively short, implying that the photon emission event has little effect on the noise characteristics of the current noise. The carriers tunnel almost independently, and thus show a Poissonian distribution. For the recombination rate limited case, the current noise becomes super-Poissonian, whilst the photon noise remains sub-Poissonian, although to a lesser degree. In this case, the mean photon recombination time period is the longest time scale, which implies that the carriers

tunnel in pairs - with two carriers tunnelling quickly, followed by a pause as the exciton recombines, leading to super-Poissonian noise characteristics. The photon noise moves towards a fano factor of 1, but the photons are still more evenly distributed than an independent case.

Figure 6.2.3 shows the simulated noise characteristics of the system.

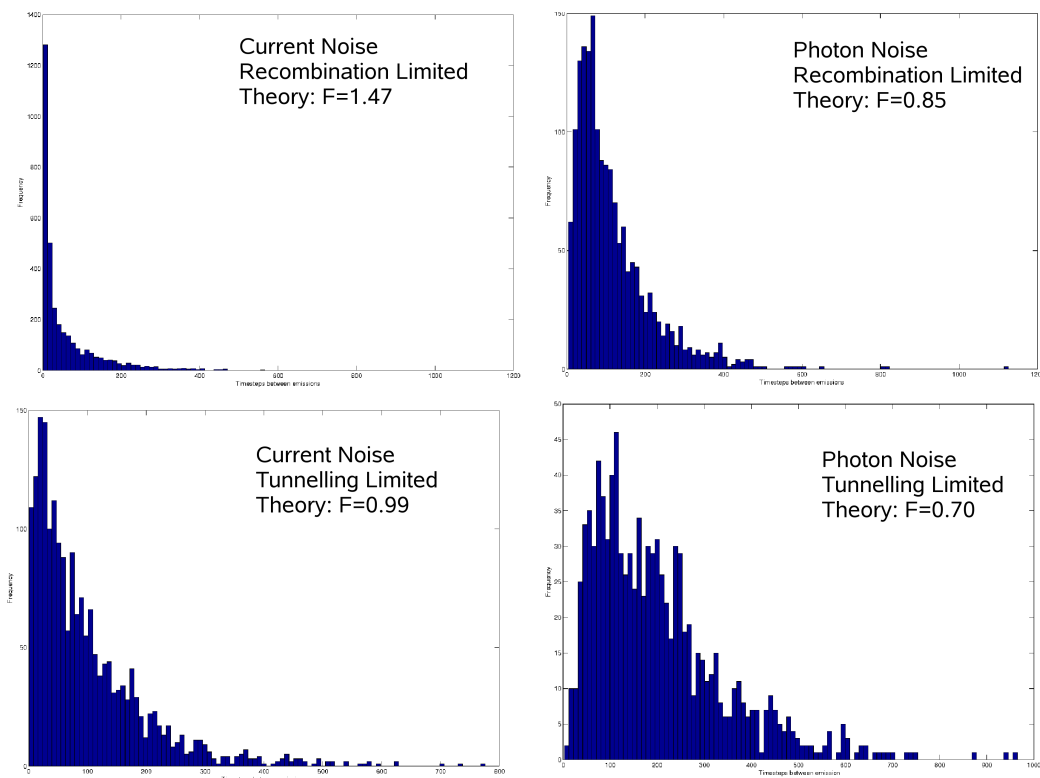


Figure 6.2.3: Simulated Noise Characteristics for different tunnelling rates. The theoretical prediction for Fano factor is shown for comparative purposes

6.3 CTR in two interacting quantum dots

Having fully analysed the CTR in one isolated QD, we can now develop the theory further to include the effects of neighbouring dots interacting with one another and creating new, more complicated sequential regimes. It has already been seen that neighbouring dots are able to interact with each other via the Coulomb Interaction, and we will now study the effects of this on a system of two QDs. We restrict ourselves to analysing a system of only two QDs because the chances of finding a system with the correct energy level alignments becomes exponentially less likely as the number of dots required increases.

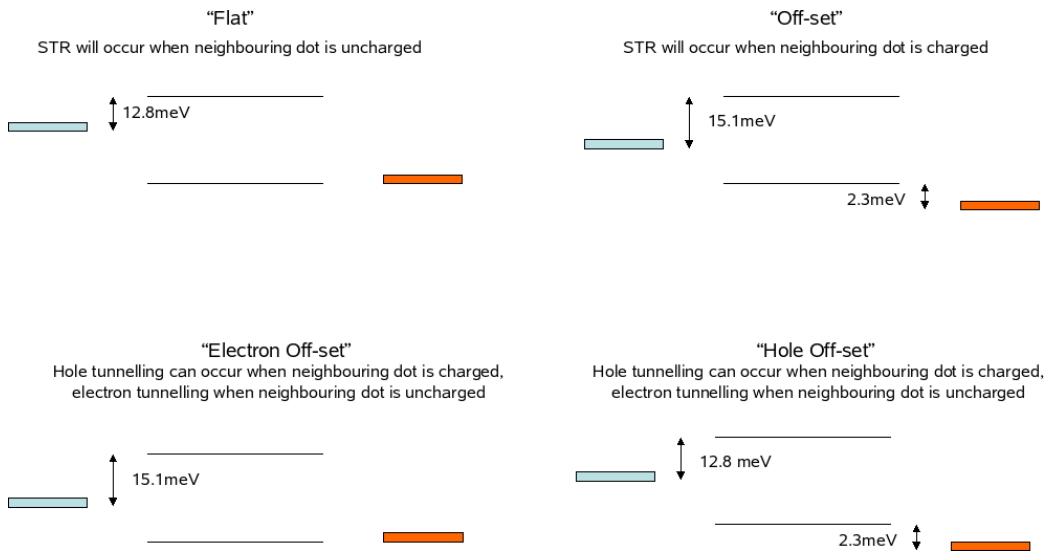


Figure 6.3.1: The four possible combinations of E_A and E_B in the dot offset. The effect of the dot itself being positively charged is to shift both electron and hole energy levels by 12.8 meV. The effect of the neighbouring dot being charged shifts the energy levels by 2.3 meV. The separation between the electron and hole levels remains constant.

The probability of a carrier resonantly tunnelling onto a dot is dependant upon the energy levels being correctly aligned at that moment. We have seen in the 1QD

regime that the electron and hole energy levels need to be offset by an energy of 12.8meV (which we now denote as E_A) for the system to be able to maintain a non-zero emission rate. The secondary offset, due to the occupation of a neighbouring dot was calculated in chapter 2 to be approximately 2.3meV (which we call E_B). This is a sufficient offset to be able to move the dot system in and out of resonance.

The 2 dot system will therefore be emissive in a regime where the electron and hole energy levels of the 2 dots are some combination of the two offsets; the tunnelling rate through one dot is not only dependant upon its own occupation, but also upon the occupation of its neighbouring dot. Figure 6.3.1 shows the four possible combinations of E_A and E_B in the dot offset.

Now we have defined the 4 possible configurations that each individual dot can be in, we need to work out the result of each of the possible combinations of the four. Figure 6.3.2 shows the 10 possible combinations of 2 dots.

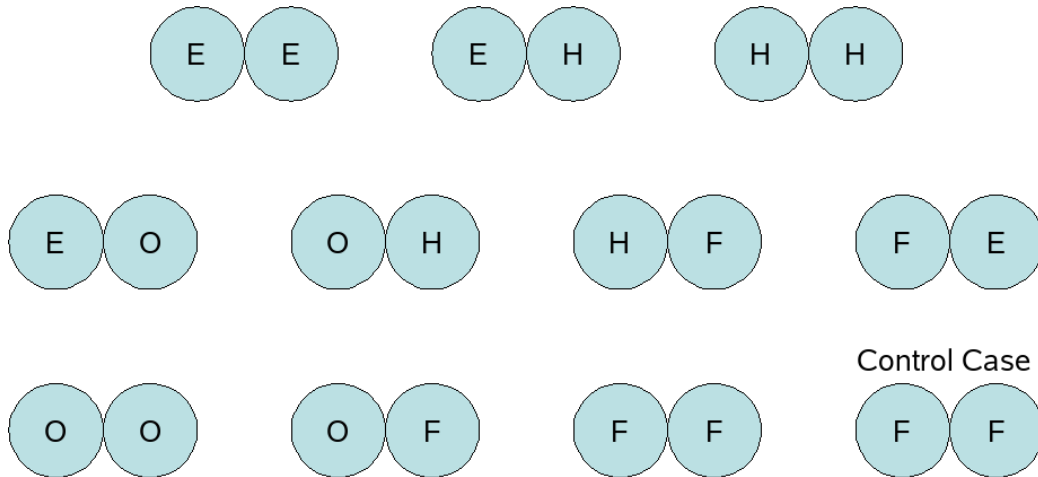


Figure 6.3.2: The 10 possible combinations of 2 dots. E,H, O, and F correspond to the four states identified in figure 6.3.1. A non-interacting control case is also included.

In order to analyse the two dot system fully, we now use a simple notation, based on the system states we used in the 1 dot scenario. Figure 6.3.3 shows the 9 possible states of the system, and the corresponding states of each dot.

Dot 1	Dot 2	Numerical State Notation
$ \downarrow\rangle$	$ \downarrow\rangle$	$ 1\rangle$
$ \downarrow\rangle$	$ 0\rangle$	$ 2\rangle$
$ 0\rangle$	$ \downarrow\rangle$	$ 3\rangle$
$ \downarrow\rangle$	$ \uparrow\rangle$	$ 4\rangle$
$ 0\rangle$	$ 0\rangle$	$ 5\rangle$
$ \uparrow\rangle$	$ \downarrow\rangle$	$ 6\rangle$
$ 0\rangle$	$ \uparrow\rangle$	$ 7\rangle$
$ \uparrow\rangle$	$ 0\rangle$	$ 8\rangle$
$ \uparrow\rangle$	$ \uparrow\rangle$	$ 9\rangle$

Figure 6.3.3: The 9 possible states of the system, and the corresponding states of each dot

Using the numerical state notation, and knowing which transitions are allowed, we are now able to plot the possible state trajectories for the 10 combinations. We also include a control case, that of two CT regime dots, identical to the one analysed in section 6.2, which do not interact with each other at all. Figure 6.3.4 shows the possible trajectories. We can clearly see that without backwards state evolu-

tion, seven of the ten combinations are immediately blocked. These combinations will emit for a finite time period, but each one has an accessible system state, which, once occupied, the system remains trapped in indefinitely. There are three combinations, however, which remain emissive indefinitely. These combinations are the F-F, O-F and E-H systems.

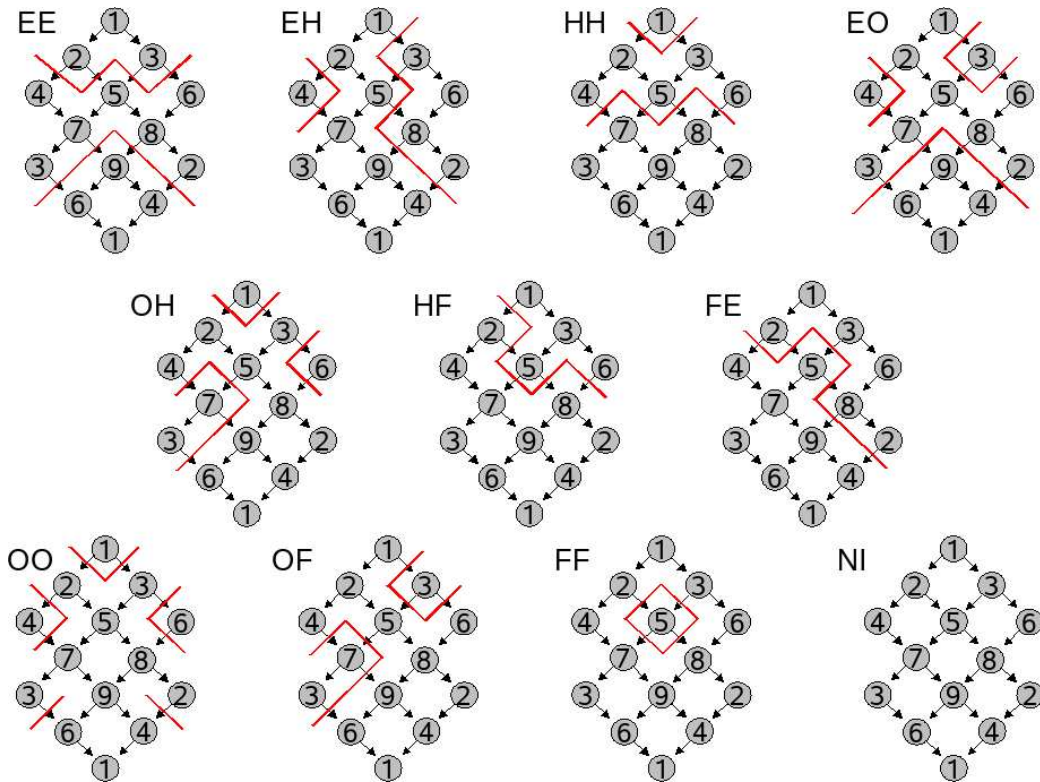


Figure 6.3.4: The possible trajectories of the system for the 10 different two-dot configurations. The solid lines denote blocked pathways. The control case is shown in the bottom right.

We can note that for the case in which one dot remains active while the other remains passive, the system will evolve diagonally on the diagram through a three state evolutionary cycle. We denote this as "lateral" movement. If both dots are simultaneously active, the system will move downwards through the states - we de-

note this as "vertical" movement. For the control sample, the system will evolve according to a random walk through the system states. Any constraints then placed on the system, will alter its evolution, and subsequently its noise characteristics. By calculating the probability of each of the infinite number of different routes the system could take to complete an evolutionary cycle, we can explicitly calculate the expected transmission rate and noise characteristics. For convenience, we choose the cycle to start and finish in state 2.

FF

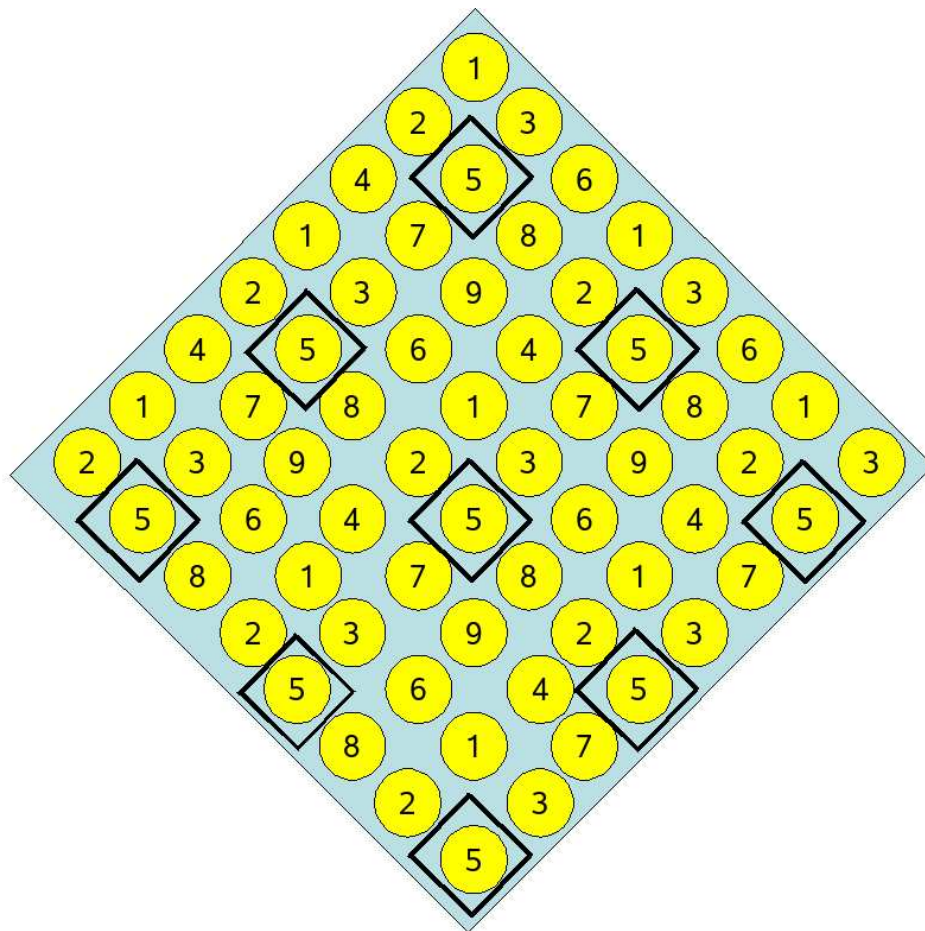


Figure 6.3.5: State Trajectories of FF system. We can see that state 5 is completely inaccessible. Other than this, the FF system is identical to the control case.

Figure 6.3.5 shows the possible state trajectories of the FF system. We see that

the only difference from the control sample is the unavailability of state 5. The overall dynamics of this system do not vary greatly from the control sample.

OF

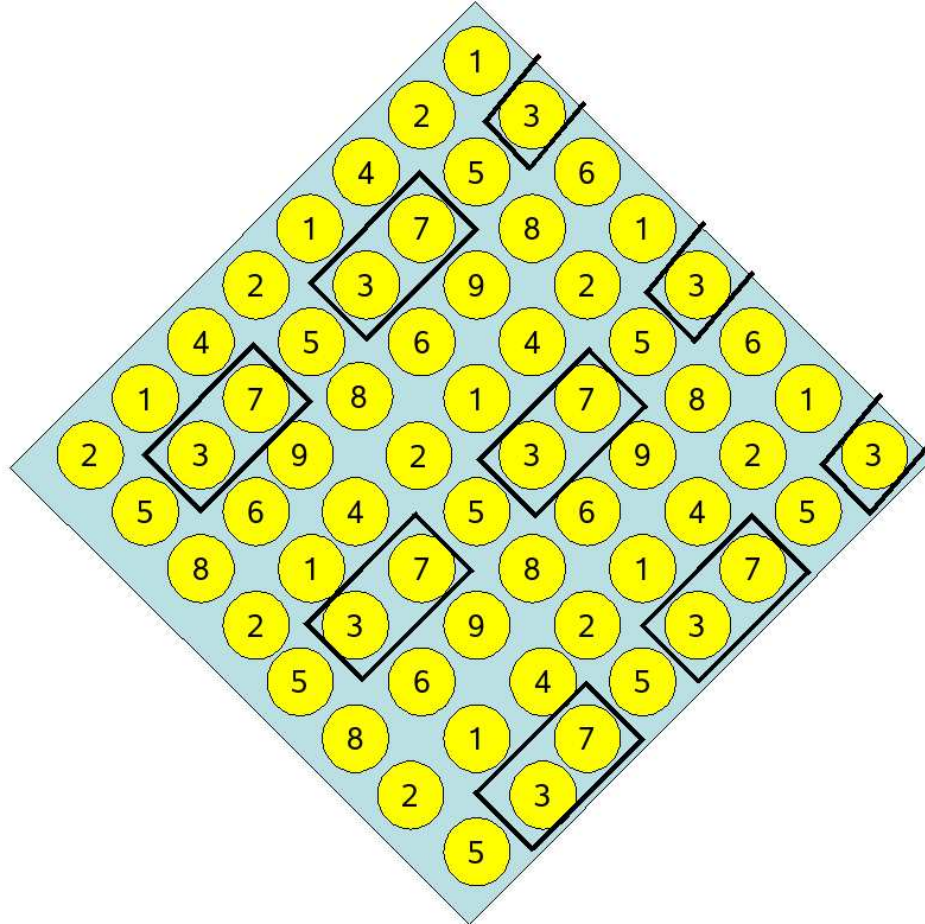


Figure 6.3.6: State Trajectories of OF system. We can see that states 3 and 7 are completely inaccessible. This has the effect of significantly raising the probability of a one-dot 1-2-4-1 evolutionary cycle, leading to a sub-Poissonian noise distribution

Figure 6.3.6 shows the possible state trajectories of the OF system. We see that states 3 and 7 are unavailable, forcing the system through state 5. This configuration also means that the system will evolve laterally, frequently following the single dot evolution chain 1-2-4-1. This predicts that one dot will be consider-

ably more active than its partner. The increase in lateral trajectories also suggests that photons be emitted from this system with a smaller frequency variation than in the control sample.

EH

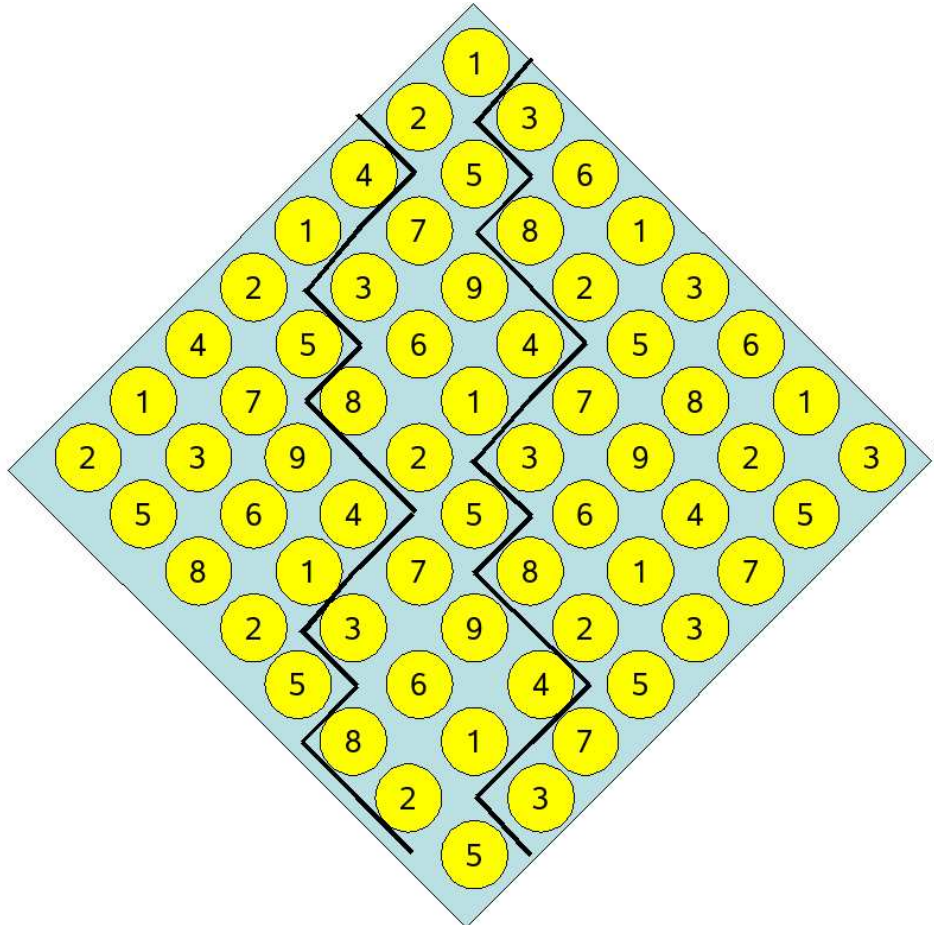


Figure 6.3.7: State Trajectories of EH system. We see the blocked pathways force the system evolution down a vertical path, and prevents the kind of one-dot evolutionary cycles prevalent in the OF configuration. The increased probability of the pathway following a 9-6-1 or 9-4-1 route leads to a super-Poissonian noise distribution

For the EH system shown in figure 6.3.7, we see that the system remains confined within a vertical channel through the states. No single dot evolution trajectories are possible in this system, implying that the two dots will move through

their individual states in unison, and release photons in pairs. We would therefore expect to see greater bunching in this system than in the control case.

We can analyse the four systems both numerically and theoretically, applying the master equation method to each system to find the evolution operator, and subsequently calculating the current and noise characteristics.

We first define a Hamiltonian for each system. The Hamiltonian for the FF, OF and EH systems will be equivalent to the Hamiltonian for the control case with the terms corresponding to the blocked interactions removed.

Using the master equation method once more, we are able to find the evolution operator, and solve for its eigenfunctions. To do this, we must first define a Hamiltonian for the two dot system, again separated into system, bath, and interaction operators. We start with the control case (NI) in which all the state transitions are allowed. We are then in a position to adjust this Hamiltonian for the other three systems of interest by removing terms corresponding to blocked transitions.

$$H_{tot} = H_S + H_B + H_I + H_I^\dagger \quad (6.3.1)$$

where

$$H_S = \varepsilon_{\uparrow 1} |\uparrow_1\rangle \langle \uparrow_1| + \varepsilon_{\downarrow 1} |\downarrow_1\rangle \langle \downarrow_1| + \varepsilon_{\uparrow 2} |\uparrow_2\rangle \langle \uparrow_2| + \varepsilon_{\downarrow 2} |\downarrow_2\rangle \langle \downarrow_2| \quad (6.3.2)$$

$$H_B = \sum_Q \left(\varepsilon_l \hat{l}_Q^\dagger \hat{l}_Q + \varepsilon_r \hat{r}_Q^\dagger \hat{r}_Q + \varepsilon_\gamma \hat{\gamma}_Q^\dagger \hat{\gamma}_Q \right) \quad (6.3.3)$$

Before calculating the interaction Hamiltonian, we simplify the system by

switching to the numerical notation seen in figure 6.3.3.

$$\begin{aligned}
 H_I = & \hat{r}_1^\dagger |2\rangle \langle 1| + \hat{r}_2^\dagger |3\rangle \langle 1| + \hat{l}_1 |4\rangle \langle 2| + \hat{r}_2^\dagger |5\rangle \langle 2| + \hat{r}_1^\dagger |5\rangle \langle 3| + \hat{l}_2 |6\rangle \langle 3| \\
 & + \hat{\gamma}_1^\dagger |1\rangle \langle 4| + \hat{r}_2^\dagger |7\rangle \langle 4| + \hat{l}_1 |7\rangle \langle 5| + \hat{l}_2 |8\rangle \langle 5| + \hat{\gamma}_2^\dagger |1\rangle \langle 6| + \hat{r}_1^\dagger |8\rangle \langle 6| \\
 & + \hat{\gamma}_1^\dagger |3\rangle \langle 7| + \hat{l}_2 |9\rangle \langle 7| + \hat{\gamma}_2^\dagger |2\rangle \langle 8| + \hat{l}_1 |9\rangle \langle 8| + \hat{\gamma}_2^\dagger |4\rangle \langle 9| + \hat{\gamma}_1^\dagger |6\rangle \langle 9| \quad (6.3.4)
 \end{aligned}$$

From this Hamiltonian, we can now repeat the procedure set out in section 6.2, and calculate bath and system operators for the 4 two-dot combinations we are interested in, from which we can calculate the Louivillian operator and the eigenfunctions of the system.

By solving for the zero eigenvalue, we can find its associated eigenfunction, which will give us the probability of occupation of each state in the system at any given time. This is shown in figure 6.3.8. The lighter squares represent the states most likely to be occupied. For the control case, all states are equally likely to be occupied. For the FF case, state 5 is inaccessible, and as a result, states 2 and 3 have the highest occupation probability, as their is only one possible exit route from these states. For the OF case, states 3 and 7 are inaccessible, leading to an increase in the occupation probability of states 1 and 4. For the EH case, all states are accessible, but we see states 2 and 5 represent the most common evolutionary route.

By taking these occupation predictions and accounting for the external emission associated with each state, we can accurately predict the average current and photocurrent through each of the systems. We can do this in three separate ways: by using the predictions above generated by the master equation method, by running a computational simulation over 1 million timesteps for each configuration,

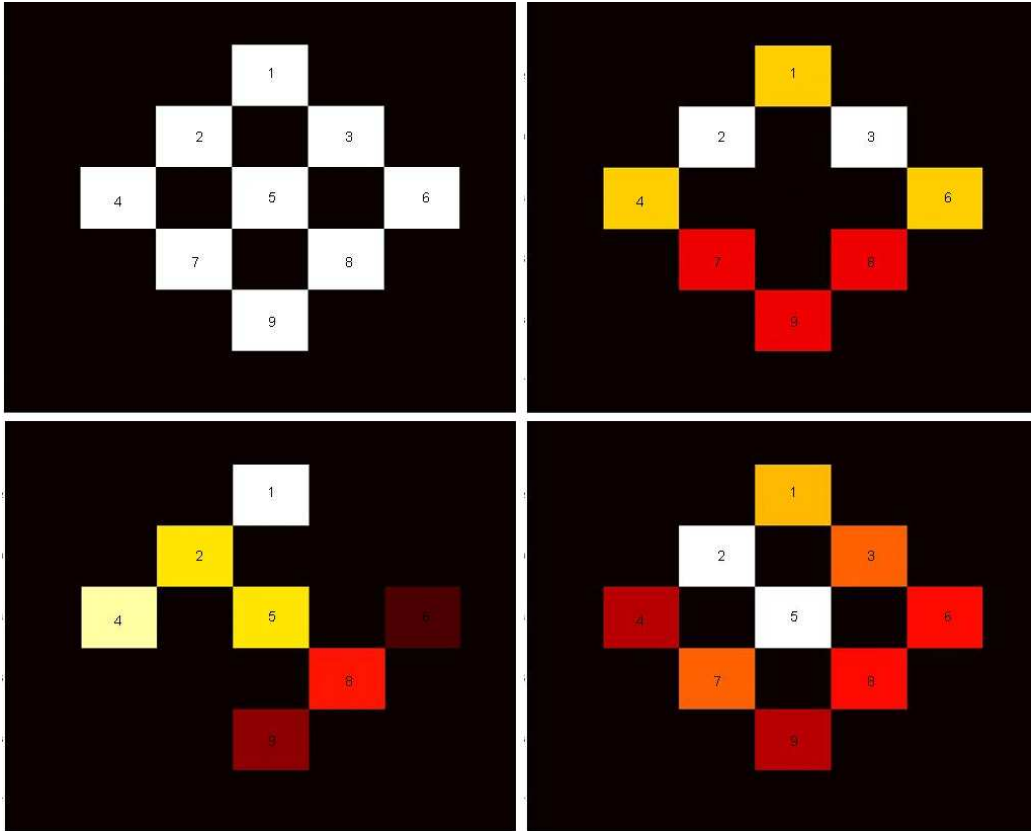


Figure 6.3.8: State occupation probabilities for each of the different two dot configurations. Clockwise from top left: NI, FF, EH, OF configurations. The lighter colour squares represent the state with the higher occupation probability at any given time.

and finally by using a simple statistical analysis of the most likely routes through the system, we can make an estimate of current and photon emission rates. The three predictions for each configuration are shown below.

We can also make a prediction of the current and photo-current noise through the configurations. Our analytical method is not detailed enough to make a numerical prediction, but as mentioned previously, the increased verticality of the EH evolutionary route should lead to a higher Fano factor, and the likely 1-2-4-1 diagonal evolution of the OF system should lead to a lower Fano factor than the

6.3. CTR in two interacting quantum dots

Photon Emission Rates	Initial Prediction	Simulation	Master Equation
No Interaction (control)	0.667	0.667	0.667
Flat-Flat	0.550	0.536	0.540
Offset-Flat	0.470	0.448	0.450
Electron-Hole	0.411	0.408	0.410

control case. The use of the numerical simulation is not subtle enough to capture these dynamics over a large number of timesteps, but by studying the variation in the number of timesteps between photon emission events, shown in figure 6.3.9, we can see that the simulation shows excellent agreement with our analytical predictions. We can see that the mean number of timesteps increases in line with the decreasing emission rates, as we move from the control sample to the more restricted configurations. We can see that the FF configuration is very similar to the control sample, with the extra timesteps caused by the single inaccessible state. Also notable is the high proportion of emissions in the 3,4 and 5 timestep range for the OF case, indicating a high degree of diagonal system evolution, and the likelihood in the EH system for the photon emission events to be either only 1 or 2 timesteps apart, or 4+, demonstrating the vertical route through the system states.

Using the eigenvectors calculated for each configuration previously, and using the same method as detailed in section 6.2, we are able to make predictions for the Fano factors of the four configurations. These results correspond as expected with both the analytical predictions and the simulated results.

Fano Factors	Master Equation Theory
No Interaction (control)	0.96
Flat-Flat	0.83
Offset-Flat	0.72
Electron-Hole	1.12

6.3. CTR in two interacting quantum dots

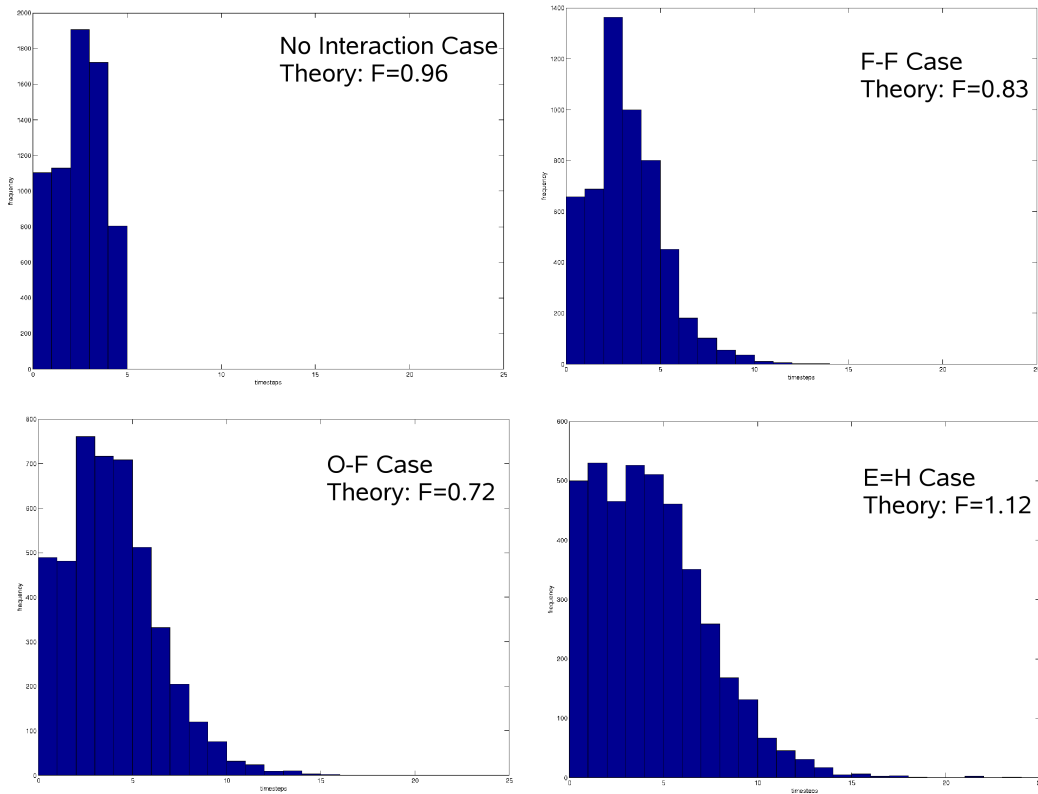


Figure 6.3.9: Noise characteristics of the numerical simulations for each of the different two dot configurations. The theoretical Fano factor prediction is included for comparison

We can clearly see that the numerical and theoretical results are in excellent agreement for both the one dot and two dot cases. We showed how the current and photon current noise characteristics are dependant upon the relevant tunnelling and recombination rates, and also showed how the current and photon current noise through a two dot system is strongly dependant upon the exact energy configurations of the dots in question. We are able to study these systems analytically and gain insight into the underlying mechanisms behind the currents and noise characteristics. Gaining a clearer understanding of the transport and electroluminescence characteristics of particular quantum dot systems could potentially provide valuable

insight into characterising novel quantum dot devices.

Chapter 7

Conclusions and Future Prospects

In chapters 2-4, we have shown that it is possible to construct a numerical model of a quantum dot array located in the intrinsic region of a p-i-n junction which accurately describes the associated experimental data. Using a master equation approach, we were able to analyse the processes involved in a two level quantum dot, and by inputting the relevant tunnelling, relaxation and recombination rates, we were able to make a prediction of the level occupation probabilities within the model. We also demonstrated that it is necessary to include both phonon-assisted relaxation and Coulomb interaction effects within each individual dot in order for the simulated results to match the experimental data in a satisfactory manner. This clearly suggests that both of these processes are an important feature of the system being modelled, and explains the origins of many of the features visible in the experiments. A more rigorous quantum mechanical treatment of quantum tunnelling, excitonic recombination, and carrier-carrier Coulomb interaction could be achieved, and may reveal several subtle features as yet unseen, but for this to become necessary, the experiments would have to be carried out at a considerably

lower temperature for any quantum correlation effects to be observed.

In chapter 5, we isolated the effects of delayed and simultaneous tunnelling current, and observed that the effect of changing the location of the dot array within the intrinsic region of the p-i-n junction has a direct effect on the bias voltages at which delayed and simultaneous tunnelling occurs. We also note that the inclusion of the Coulomb interaction leads to a feedback dominated regime, in which a mixture of delayed and simultaneous tunnelling is spread over the entire range of bias voltages.

We then investigated this concept further by analysing the Coulomb field fluctuations around the dot array over the entire range of bias voltages. The correlation length of these fluctuations was shown to directly correspond with the dot occupation, indicating a series of feedback dominated fluctuations in the tunnelling currents. It is again worth noting that these fluctuations have been treated semi-classically. For a more detailed study of Coulomb triggered Fermi sea fluctuations, a more rigorous quantum mechanical treatment would be required.

We studied the process of up-conversion luminescence and the proposed Auger mechanism. By a straightforward QM calculation, we were able to include basic Auger processes in our model, and found that the results were in excellent agreement with experimental data. We also calculated the effect of a varying magnetic field on the system, and predicted a reduction in UCL at increasing fields. A further potential development in studying UCL and the Auger process would be to simulate the system with the dot layer embedded within a leaky resonant cavity. This would lead to laser action, and a study of the photon statistics in this scenario could potentially be interesting.

When studying the fluctuations in the Coulomb field as a function of time, it

was discovered that several dots were emitting in a regime in which electrons and holes tunneled into the dot's resonant energy levels alternately. We designated this regime the “correlated tunnelling regime”, and studied it in detail in chapter 6, using a variety of methods. We first studied the regime for the one dot case for both tunnelling and recombination limited systems, using a numerical simulation and master equation analysis to make predictions concerning the current and photo-current noise through the dot.

We also analyzed a range of different two dot systems, involving different combinations of single dots with resonant energy offsets. We demonstrated that only three of the ten possible combinations would be capable of continued systematic evolution, leading to current transport and photon evolution. We again analyzed these systems using a numerical simulation and master equation approach, and derived results for mean currents and photo-currents, and their respective noise characteristics. The numerical and analytical results showed remarkable correspondence.

We have observed the single dot correlated tunnelling regime in simulation, but not experimentally. It would be interesting to study experimental data to see what possible correlated tunnelling regimes might be visible, and to ascertain how many dots are involved. The noise measurements for current and photon noise are also generated by the simulation; noise measurements for noise through a quantum dot array are possible and would enable a further means of comparison.

Bibliography

- [1] T. Takagahara, Phys. Rev. B **36**, 9293 (1987).
- [2] M. A. Reed, R. Bate, et al., J. Vac. Sci. Tech. B **4**, 358 (1986).
- [3] A. D. Yoffe, Adv. in Phys **50** (2001).
- [4] J. Singh, *Semiconductor Devices: An Introduction* (McGraw-Hill, 1994).
- [5] H. Haug and S. W. Koch, *Quantum theory of Optical and Electronic Properties of Semiconductors* (World Scientific, 2004).
- [6] <http://www.ioffe.ru/SVA/NSM/Semicond/GaAs/Figs/421.gif>.
- [7] A. F. J. Levi, *Applied Quantum Mechanics* (Cambridge, 2003).
- [8] A. R. Chaggar, Ph.D. thesis, University of Nottingham (2008).
- [9] L. Turyanska, A. Baumgartner, et al., Appl. Phys. Lett. **89**, 092106 (2006).
- [10] J. H. Davies, *the Physics of Low Dimensional Semiconductors: An Introduction* (Cambridge University Press, 1998).
- [11] Y. H. Chen, J. Sun, et al., Appl. Phys. Lett. **88**, 0719303 (2006).
- [12] W. M. McGee, T. J. Krzyewski, and T. S. Jones, J. Appl. Phys. **99**, 043505 (2006).
- [13] Q. Gong, P. Offermans, et al., Appl. Phys. Lett. **85**, 5697 (2004).
- [14] L. Turyanska, A. Baumgartner, et al., Appl. Phys. Lett. **92**, 091121 (2008).
- [15] A. Patane, R. J. A. Hill, et al., Phys. Rev. B **65**, 165308 (2002).
- [16] R. Yang and P. P. Ruden, J. Appl. Phys. **78**, 3 (1995).
- [17] M. Taut, Phys. Rev. A **48**, 3561 (1993).

- [18] O. Stier, M. Grundmann, and D. Bimberg, Phys. Rev. B **59**, 5688 (1999).
- [19] A. J. Williamson, L. W. Wang, and A. Zunger, Phys. Rev. B **62**, 12936 (2000).
- [20] M. A. Cusack, P. R. Briddon, and M. Jaros, Phys. Rev. B **54**, R2300 (1996).
- [21] O. Engstroem, A. Eghtedari, and M. Kaniewska, Materials Science and Engineering **27**, 936 (2007).
- [22] <http://hyperphysics.phy-astr.gsu.edu/HBASE/quantum/hosc5.html>.
- [23] Y. Alhassid, Rev. Mod. Phys. **72**, 895 (2000).
- [24] L. L. Sohn, L. P. Kouwenhoven, and G. Schoen, *Mesoscopic Electron Transport* (Springer, 1997).
- [25] S. Datta, *Electron Transport in Mesoscopic Systems* (Cambridge, 1995).
- [26] G. W. Hoofdt, W. A. J. L. van der Poel, and L. W. Molenkamp, Phys. Rev. B **35**, 8281 (1987).
- [27] F. Adler, M. Geiger, et al., J. Appl. Phys. **80**, 4019 (1996).
- [28] M. J. Steer, D. J. Mowbray, et al., Phys. Rev. B **54**, 17738 (1996).
- [29] A. Imamoglu and Y. Yamamoto, Phys. Rev. Lett. **72**, 210 (1994).
- [30] H. Carmichael, *An Open Systems Approach to Quantum Optics* (Springer-Verlag, 1993).
- [31] W. H. Press and S. A. T. and, *Numerical Recipes in C: The Art of Scientific Computing* (Cambridge University Press, 1992).
- [32] C. J. Gorter, Physica **17**, 777 (1951).
- [33] M. Rontani, G. Maruccio, et al., J. Appl. Phys. **101**, 081714 (2007).
- [34] G. Medeiros-Ribeiro, F. G. Pikus, et al., Phys. Rev. B **55**, 1573 (1997).
- [35] R. J. Warburton, B. T. Miller, et al., Phys. Rev. B **58**, 16 221 (1998).
- [36] G. Kiesslich, A. Wacker, and E. Scholl, Phys. Rev. B **68**, 125320 (2003).
- [37] G. Kiesslich, A. Wacker, and E. Scholl, Physica E **12**, 837 (2002).
- [38] G. Kiesslich, A. Wacker, and E. Scholl, Physica B **314**, 459 (2002).

- [39] P. P. Paskov, P. O. Holtz, et al., *Appl. Phys. Lett.* **77**, 812 (2000).
- [40] D. Morris, N. Perret, and S. Fafard, *S. App. Phys. Lett.* **75(23)** (1999).
- [41] C. Kammerer, G. Cassabois, et al., *Phys. Rev. Lett.* **87(20)**, 207401 (2001).
- [42] T. Harvey, Ph.D. thesis, University of Nottingham (2009).
- [43] Y. M. Blanter and M. Buttiker, *Phys. Rep.* **336**, 1 (2000).